Thesis Report

Analytical modelling of the three-dimensional stress field induced by fluid production and injection in reservoirs with displaced faults

Pranshu Singhal

Pictures courtesy of Drs. Jan Kees Blom

TU Delft

Thesis Report

Analytical modelling of the three-dimensional stress field induced by fluid production and injection in reservoirs with displaced faults

by

Pranshu Singhal

to obtain the degree of Master of Science
at the Delft University of Technology,
to be defended publicly on August 21, 2019.

Student number: 4733649		
Thesis committee:	Prof. Dr. J. D. Jansen,	TU Delft, supervisor
	Dr. F. Vossepoel,	TU Delft
	Prof. Dr. K. Wapenaar.	TU Delft

An electronic version of this thesis is available at `http://repository.tudelft.nl/`.

Abstract

Injection and production of fluids into/from the subsurface has been known to trigger earthquakes, referred to as induced seismicity. This seismicity may occur when anthropogenically caused changes in the in-situ stress conditions result in reactivation of pre-existing faults in the subsurface causing slip accompanied by sudden release of energy. Several studies have numerically modelled the induced stresses due to production/injection in reservoirs of various geometries. In this report we present a simplified three-dimensional reservoir with a displaced fault and derive analytical expressions for induced stresses in and outside the reservoir due to production and injection of fluids. We use the calculated stresses for the three-dimensional model and analyse onset of slip across the fault. The research builds upon the analytical two-dimensional plane-strain analysis for induced stresses and slip initiation in Jansen et al. [10] to which our work contributed. We reaffirm the findings from the plane-strain analysis in Jansen et al. [10] and conclude that the effects of incorporating third dimension on induced stresses and slip behaviour are limited. We find infinite peaks in resultant shear stresses at the reservoir boundaries and observe a distinctly different pattern in induced stresses and slip behaviour between production and injection scenarios. In case of production, the slip patches are predicted to grow inwards into the reservoir initially until they merge, while for injection the slip patches grow separately into the overburden and underburden. The findings in this report are in agreement with the previous analytical and numerical studies on induced seismicity. In this research we also introduce geometrical complexity in the reservoir in the form of laterally varying height of the reservoir and we observe that the effects of variation in reservoir thickness are also minimal, however the induced stress patterns and slip initiation is significantly impacted by fault throw, initial stress conditions and fault frictional characteristics.

Acknowledgements

Foremost, I would like to offer my sincere gratitude and thanks to my thesis committee chair Prof. Jan-Dirk Jansen without whose vision this research would not have been possible. His patience, dedication and motivation has made this research seem much more easier than it was. I have benefited immensely from his guidance at each step of the research and writing of my thesis. His immense knowledge and expertise and willingness to help make him the ideal supervisor I could have asked for. I would also like to thank the rest of my thesis committee, Dr. Femke Vossepoel and Prof. Kees Wapenaar for their time and assistance. In particular Dr. Vossepoel's commitment to the research has been exceptional and her invaluable inputs during the writing phase have helped me significantly improve the quality of this report.

I would also like to acknowledge the support extended by the administrative staff at the Delft University of Technology for making the whole process trouble-free. Lastly, I would like to thank my family, my girlfriend and my friends for supporting me throughout the duration of this research and for keeping me going.

Delft University of Technology
August 2019
Pranshu Singhal

Contents

List of Figures ix

List of Tables xiii

1 Introduction 1
- 1.1 Induced seismicity 1
  - 1.1.1 Background 2
  - 1.1.2 Causal mechanisms 2
- 1.2 Previous studies on induced stresses and fault slip 3
- 1.3 Research objectives 5
- 1.4 Assumptions 9
  - 1.4.1 Sign convention 9

2 Analytical Model 11
- 2.1 Two-Dimensional 11
  - 2.1.1 Vertical fault 12
  - 2.1.2 Inclined fault. 12
- 2.2 Three-dimensional 13
  - 2.2.1 Symmetrical cuboidal reservoir 13
  - 2.2.2 Asymmetrical laterally thinning reservoir 14

3 Methodology 15
- 3.1 Inclusion theory 15
- 3.2 Green's functions 17
  - 3.2.1 Displacements 18
  - 3.2.2 Stresses 19
- 3.3 Induced stresses 20
  - 3.3.1 Cuboidal reservoir 20
  - 3.3.2 Thinning reservoir 20

4 Results and Discussion 23
- 4.1 Stresses 23
  - 4.1.1 Cuboidal 23
  - 4.1.2 Asymmetrical/laterally thinning reservoir 28
- 4.2 Slip 34
- 4.3 Shear stress directions 45
- 4.4 Sensitivity. 46

5 Conclusions 49

Bibliography 53

Appendices 55
- A Induced stresses in three-dimensional symmetrical cuboidal reservoir with a displaced fault . . 57
- B Induced stresses in three-dimensional asymmetrical laterally thinning reservoir with a displaced fault 60

List of Figures

1.1 From Jansen et al. [10]: Total shear stresses resulting from decreasing incremental reservoir pressures p (production), and corresponding slip boundaries for the top half of a two-dimensional reservoir with a displaced fault as depicted in figure (2.1), under plane-strain conditions with dimensions as listed in table (2.2). Total shear stresses; orange: $p = 0$ MPa, blue: $p = -5$ MPa, red: $p = -20$ MPa, green: $p = -35$ MPa. Slip boundaries; light gray: $p = 0$ MPa, medium gray: $p = -5$ MPa, dark gray: $p = -20$ MPa and black: $p = 35$ MPa. y_3 and y_4 represent the intersections of shear stress and slip boundary for the top half of the reservoir. 7
1.2 From Jansen et al. [10]: Intersections y_3 and y_4 of the shear stress profile with the slip threshold for the upper slip patch, and total slip patch half-length $L_{sl}/2 = y_4 - y_3$ as a function of incremental pressure p during production. 7

2.1 Schematic for a two-dimensional reservoir with a displaced normal fault. 12
2.2 Schematic for a three-dimensional symmetrical cuboidal reservoir with a displaced normal fault. 13
2.3 Cross section for $x < 0$ m and $x > 0$ m for an asymmetrical laterally thinning reservoir reservoir with a displaced normal fault. 14

3.1 From Jansen et al. [10]: Schematic depicting the imaginary steps involved in calculating displacements in and around an expanding inclusion Ω in an infinite matrix. 17
  (a) Step 1 17
  (b) Step 2 17
  (c) Step 3 17
3.2 Cuboidal unit used as the integration unit for a symmetrical cuboidal reservoir 21
3.3 Cuboidal unit with a wedge shaped unit on top used as the integration unit for an asymmetrical laterally thinning reservoir 21

4.1 Dimensionless normal stresses $\frac{\sigma_{xx}}{C}$ and $\frac{\sigma_{yy}}{C}$ at the planes corresponding to $x = 0$, $y = 0$ and $z = 0$, with the scaling parameter $C = 2.36 \times 10^6 N/m^2$ as defined in equation (3.25), for a symmetrical cuboidal reservoir with dimensions as listed in table (2.3). 25
  (a) Dimensionless normal stress $\frac{\sigma_{xx}}{C}$ on the yz plane (Symmetrical) 25
  (b) Dimensionless normal stress $\frac{\sigma_{xx}}{C}$ on the xy plane (Symmetrical) 25
  (c) Dimensionless normal stress $\frac{\sigma_{xx}}{C}$ on the zx plane (Symmetrical) 25
  (d) Dimensionless normal stress $\frac{\sigma_{yy}}{C}$ on the yz plane (Symmetrical) 25
  (e) Dimensionless normal stress $\frac{\sigma_{yy}}{C}$ on the xy plane (Symmetrical) 25
  (f) Dimensionless normal stress $\frac{\sigma_{yy}}{C}$ on the zx plane (Symmetrical) 25
4.2 Dimensionless normal stress $\frac{\sigma_{zz}}{C}$ and Dimensionless shear stress $\frac{\sigma_{xy}}{C}$ at the planes corresponding to $x = 0$, $y = 0$ and $z = 0$, with the scaling parameter $C = 2.36 \times 10^6 N/m^2$ as defined in equation (3.25), for a symmetrical cuboidal reservoir with dimensions as listed in table (2.3). . . 26
  (a) Dimensionless normal stress $\frac{\sigma_{zz}}{C}$ on the yz plane (Symmetrical) 26
  (b) Dimensionless normal stress $\frac{\sigma_{zz}}{C}$ on the xy plane (Symmetrical) 26
  (c) Dimensionless normal stress $\frac{\sigma_{zz}}{C}$ on the zx plane (Symmetrical) 26
  (d) Dimensionless shear stress $\frac{\sigma_{xy}}{C}$ on the yz plane (Symmetrical) 26
  (e) Dimensionless shear stress $\frac{\sigma_{xy}}{C}$ on the xy plane (Symmetrical) 26
  (f) Dimensionless shear stress $\frac{\sigma_{xy}}{C}$ on the zx plane (Symmetrical) 26
4.3 Dimensionless shear stresses $\frac{\sigma_{yz}}{C}$ and $\frac{\sigma_{zx}}{C}$ at the planes corresponding to $x = 0$, $y = 0$ and $z = 0$, with the scaling parameter $C = 2.36 \times 10^6 N/m^2$ as defined in equation (3.25), for a symmetrical cuboidal reservoir with dimensions as listed in table (2.3). 27
  (a) Dimensionless shear stress $\frac{\sigma_{yz}}{C}$ on the yz plane (Symmetrical) 27

(b) Dimensionless shear stress $\frac{\sigma_{yz}}{C}$ on the xy plane (Symmetrical) 27
(c) Dimensionless shear stress $\frac{\sigma_{yz}}{C}$ on the zx plane (Symmetrical) 27
(d) Dimensionless shear stress $\frac{\sigma_{zx}}{C}$ on the yz plane (Symmetrical) 27
(e) Dimensionless shear stress $\frac{\sigma_{zx}}{C}$ on the xy plane (Symmetrical) 27
(f) Dimensionless shear stress $\frac{\sigma_{zx}}{C}$ on the zx plane (Symmetrical) 27

4.4 Dimensionless normal stresses $\frac{\sigma_{xx}}{C}$ and $\frac{\sigma_{yy}}{C}$ at the planes corresponding to $x = 0$, $y = 0$ and $z = 0$, with the scaling parameter $C = 2.36 \times 10^6 N/m^2$ as defined in equation (3.25), for an asymmetrical laterally thinning reservoir with dimensions as listed in table (2.3). 29
(a) Dimensionless normal stress $\frac{\sigma_{xx}}{C}$ on the yz plane (Asymmetrical) 29
(b) Dimensionless normal stress $\frac{\sigma_{xx}}{C}$ on the xy plane (Asymmetrical) 29
(c) Dimensionless normal stress $\frac{\sigma_{xx}}{C}$ on the zx plane (Asymmetrical) 29
(d) Dimensionless normal stress $\frac{\sigma_{yy}}{C}$ on the yz plane (Asymmetrical) 29
(e) Dimensionless normal stress $\frac{\sigma_{yy}}{C}$ on the xy plane (Asymmetrical) 29
(f) Dimensionless normal stress $\frac{\sigma_{yy}}{C}$ on the zx plane (Asymmetrical) 29

4.5 Dimensionless normal stress $\frac{\sigma_{zz}}{C}$ and Dimensionless shear stress $\frac{\sigma_{xy}}{C}$ at the planes corresponding to $x = 0$, $y = 0$ and $z = 0$, with the scaling parameter $C = 2.36 \times 10^6 N/m^2$ as defined in equation (3.25), for an asymmetrical laterally thinning reservoir with dimensions as listed in table (2.3). 30
(a) Dimensionless normal stress $\frac{\sigma_{zz}}{C}$ on the yz plane (Asymmetrical) 30
(b) Dimensionless normal stress $\frac{\sigma_{zz}}{C}$ on the xy plane (Asymmetrical) 30
(c) Dimensionless normal stress $\frac{\sigma_{zz}}{C}$ on the zx plane (Asymmetrical) 30
(d) Dimensionless shear stress $\frac{\sigma_{xy}}{C}$ on the yz plane (Asymmetrical) 30
(e) Dimensionless shear stress $\frac{\sigma_{xy}}{C}$ on the xy plane (Asymmetrical) 30
(f) Dimensionless shear stress $\frac{\sigma_{xy}}{C}$ on the zx plane (Asymmetrical) 30

4.6 Dimensionless shear stresses $\frac{\sigma_{yz}}{C}$ and $\frac{\sigma_{zx}}{C}$ at the planes corresponding to $x = 0$, $they = 0$ and $z = 0$, with the scaling parameter $C = 2.36 \times 10^6 N/m^2$ as defined in equation (3.25), for an asymmetrical laterally thinning reservoir with dimensions as listed in table (2.3). 31
(a) Dimensionless shear stress $\frac{\sigma_{yz}}{C}$ on the yz plane (Asymmetrical) 31
(b) Dimensionless shear stress $\frac{\sigma_{yz}}{C}$ on the xy plane (Asymmetrical) 31
(c) Dimensionless shear stress $\frac{\sigma_{yz}}{C}$ on the zx plane (Asymmetrical) 31
(d) Dimensionless shear stress $\frac{\sigma_{zx}}{C}$ on the yz plane (Asymmetrical) 31
(e) Dimensionless shear stress $\frac{\sigma_{zx}}{C}$ on the xy plane (Asymmetrical) 31
(f) Dimensionless shear stress $\frac{\sigma_{zx}}{C}$ on the zx plane (Asymmetrical) 31

4.7 Dimensionless normal stress $\frac{\sigma_{xx}}{C}$ and dimensionless shear stress $\frac{\sigma_{xy}}{C}$ at the $z = 0$ (xy) plane, with the scaling parameter $C = 2.36 \times 10^6 N/m^2$ for a symmetrical cuboidal reservoir with dimensions as listed in table (2.3), depicted for the whole reservoir including the horizontal booundaries ($x \pm 3000$ m) 32
(a) Dimensionless normal stress $\frac{\sigma_{xx}}{C}$ on the xy plane (whole reservoir) 32
(b) Dimensionless normal stress $\frac{\sigma_{xy}}{C}$ on the xy plane (whole reservoir) 32

4.8 Dimensionless normal stress $\frac{\sigma_{xx}}{C}$ and dimensionless shear stress $\frac{\sigma_{xy}}{C}$ at the $z = 0$ (xy) plane, with the scaling parameter $C = 2.36 \times 10^6 N/m^2$ for a symmetrical cuboidal reservoir with throw, $t = 0$, $a = b = 150$ m and all other dimensions as listed in table (2.3) 33
(a) Dimensionless normal stress $\frac{\sigma_{xx}}{C}$ on the xy plane (whole reservoir) 33
(b) Dimensionless shear stress $\frac{\sigma_{xy}}{C}$ on the xy plane (whole reservoir) 33

4.9 Total resultant shear stress at different z, for an incremental reservoir pressure, $p = -20$ MPa . The solid black line represents the slipping boundary 35

4.10 Stresses at $z \approx 0$ for an reservoir pressure, $p = -20$ MPa . a) Horizontal stresses; orange: σ'^{0}_{normal}, green: σ_{normal}, blue: σ'_{normal}, red: $\sigma'^{0}_{normal} + \sigma'_{normal}$. b) Shear stresses; orange: σ^{0}_{shear}, blue: $\sigma^{R,inc}_{shear}$, red:$\sigma^{R,T}_{shear}$. c) Regions of slip; red: $\sigma^{R,T}_{shear}$, gray: slip boundaries $\pm\mu$ ($\sigma'^{0}_{normal} + \sigma'_{normal}$) ; 36

4.11 Stresses at $z \approx 0$ for an reservoir pressure, $p = 20$ MPa . a) Horizontal stresses; orange: σ'^{0}_{normal}, green: σ_{normal}, blue: σ'_{normal}, red: $\sigma'^{0}_{normal} + \sigma'_{normal}$. b) Shear stresses; orange: σ^{0}_{shear}, blue: $\sigma^{R,inc}_{shear}$, red:$\sigma^{R,T}_{shear}$. c) Regions of slip; red: $\sigma^{R,T}_{shear}$, gray: slip boundaries $\pm\mu$ ($\sigma'^{0}_{normal} + \sigma'_{normal}$) ; 36

4.12 Shear stresses in a symmetrical cuboidal reservoir, resulting from different incremental reservoir pressures p. a) production; orange: $p = 0$ MPa, blue: $p = -5$ MPa, red: $p = -20$ MPa, green: $p = -35$ MPa. b) injection; orange: $p = 0$ MPa, blue: $p = 5$ MPa, red: $p = 20$ MPa, green: $p = 35$ MPa. Gray lines in both figures: boundaries; light gray: $p = 0$ MPa, medium gray: $p = \pm 5$ MPa, dark gray: $p = \pm 20$ MPa and black: $p = \pm 35$ MPa. 38

4.13 Shear Capacity Utilization (SCU) for different incremental pore pressures (Injection), for a symmetrical cuboidal reservoir with dimensions as listed in table (2.3). The red portions represents regions where resultant total shear stresses are beyond the slip conditions, and thus represent the slip patch. 40
(a) SCU, $p = 0$ MPa (Symmetrical) 40
(b) SCU, $p = 2$ MPa(Symmetrical) 40
(c) SCU, $p = 5$ MPa (Symmetrical) 40
(d) SCU, $p = 10$ MPa (Symmetrical) 40
(e) SCU, $p = 15$ MPa (Symmetrical) 40
(f) SCU, $p = 20$ MPa (Symmetrical) 40
(g) SCU, $p = 25$ MPa (Symmetrical) 40
(h) SCU, $p = 35$ MPa (Symmetrical) 40

4.14 Shear Capacity Utilization (SCU) for different incremental pore pressures (Production), for a symmetrical cuboidal reservoir with dimensions as listed in table (2.3). The red portions represents regions where resultant total shear stresses are beyond the slip conditions, and thus represent the slip patch. 41
(a) SCU, $p = 0$ MPa (Symmetrical) 41
(b) SCU, $p = -2$ MPa(Symmetrical) 41
(c) SCU, $p = -5$ MPa (Symmetrical) 41
(d) SCU, $p = -10$ MPa (Symmetrical) 41
(e) SCU, $p = -15$ MPa (Symmetrical) 41
(f) SCU, $p = -20$ MPa (Symmetrical) 41
(g) SCU, $p = -25$ MPa (Symmetrical) 41
(h) SCU, $p = -35$ MPa (Symmetrical) 41

4.15 Shear Capacity Utilization (SCU) for different incremental pore pressures (Production) depicting the merging of slip patches, for a symmetrical cuboidal reservoir with dimensions as listed in table (2.3). The red portions represents regions where resultant total shear stresses are beyond the slip conditions, and thus represent the slip patch. 42
(a) SCU, $p = -26$ MPa (Symmetrical) 42
(b) SCU, $p = -27$ MPa(Symmetrical) 42
(c) SCU, $p = -28$ MPa (Symmetrical) 42
(d) SCU, $p = -29$ MPa (Symmetrical) 42
(e) SCU, $p = -30$ MPa (Symmetrical) 42
(f) SCU, $p = -31$ MPa (Symmetrical) 42
(g) SCU, $p = -32$ MPa (Symmetrical) 42
(h) SCU, $p = -33$ MPa (Symmetrical) 42

4.16 Shear Capacity Utilization (SCU) for different incremental pore pressures (Injection), for an asymmetrical thinning reservoir with dimensions as listed in table (2.3). The red portions represents regions where resultant total shear stresses are beyond the slip conditions, and thus represent the slip patch. 43
(a) SCU, $p = 0$ MPa (Asymmetrical) 43
(b) SCU, $p = 2$ MPa (Asymmetrical) 43
(c) SCU, $p = 5$ MPa (Asymmetrical) 43
(d) SCU, $p = 10$ MPa (Asymmetrical) 43
(e) SCU, $p = 15$ MPa (Asymmetrical) 43
(f) SCU, $p = 20$ MPa (Asymmetrical) 43
(g) SCU, $p = 25$ MPa (Asymmetrical) 43
(h) SCU, $p = 35$ MPa (Asymmetrical) 43

4.17 Shear Capacity Utilization (SCU) for different incremental pore pressures (Production), for an asymmetrical thinning reservoir with dimensions as listed in table (2.3). The red portions represents regions where resultant total shear stresses are beyond the slip conditions, and thus represent the slip patch. 44
  (a) SCU, $p = 0$ MPa (Asymmetrical) 44
  (b) SCU, $p = -2$ MPa(Asymmetrical) 44
  (c) SCU, $p = -5$ MPa (Asymmetrical) 44
  (d) SCU, $p = -10$ MPa (Asymmetrical) 44
  (e) SCU, $p = -15$ MPa (Asymmetrical) 44
  (f) SCU, $p = -20$ MPa (Asymmetrical) 44
  (g) SCU, $p = -25$ MPa (Asymmetrical) 44
  (h) SCU, $p = -35$ MPa (Asymmetrical) 44
4.18 Vector plot for total resultant shear stresses $\sigma^{R,T}_{shear}$, for a symmetrical cuboidal reservoir and for an asymmetrical laterally thinning reservoir, at a incremental pore pressure $p = -20$ MPa (Production). The arrows depict the vector direction, while the size of the arrows depicts the magnitude of the vector. 45
  (a) Vector plot for total resultant shear stress, $p = -20$ MPa (Symmetrical) 45
  (b) Vector plot for total resultant shear stress, $p = -20$ MPa (Asymmetrical) 45
4.19 Total resultant shear stresses, $\sigma^{R,T}_{shear}$ (Solid lines), and the corresponding slip boundaries (dashed lines) at incremental pore pressures $p = -20$ MPa (Production) for different reservoir heights. The ratio of throw to height is fixed for all cases at $t/H = 1/3$ 46
4.20 Total resultant shear stresses, $\sigma^{R,T}_{shear}$ (Solid lines), and the corresponding slip boundaries (dashed lines) at incremental pore pressures $p = -5$ MPa and $p = -20$ MPa (Production) for different fault throws. Height of the reservoir is fixed for all cases at $H = 300$ m 47
  (a) Sensitivity of slip initiation to fault throw, t, at pore pressure $p =$ at pore pressure $p =$ -5Mpa 47
  (b) Sensitivity of slip initiation to fault throw, t, at pore pressure $p =$ -20Mpa 47

List of Tables

2.1 Reservoir Properties and Initial Stresses 11
2.2 Reservoir and fault dimensions for two-dimensional plane-strain analysis as in Jansen et al. [10] 12
2.3 Reservoir and fault dimensions for three-dimensional analysis 13

1

Introduction

Induced seismicity has been observed over several years from a wide variety of anthropogenic activities such as mining operations, nuclear tests, extraction of hydrocarbons, waste water disposal, carbon capture and storage (CCS), hydraulic fracturing etc. The injection or production of fluids from the subsurface alters existing stress patterns, which ultimately results in build up of energy that may be released suddenly in the form of seismicity. While induced seismicity due to injection is expected due to the destabilising nature of the associated pore pressure increase, the seismicity induced by production is less intuitive and not as well understood. The Groningen field in the Netherlands, along with its long history of gas production, also has a history of production-induced seismicity. It is now understood that the heterogeneous deformations and stress development along faults are the likely cause for this induced seismicity in the Groningen field, along with other natural gas fields in the Netherlands and Germany with a similar geological setting [10] [2] [27][1][26]. Several studies in the recent past have numerically modelled the deformations and stress changes in faulted reservoirs as a result of gas production or fluid injection. This project aims to find analytical expressions for injection and production-induced stresses across a fault in a simplified homogeneous three-dimensional reservoir that will help understand the causal mechanisms behind the induced seismicity. In this report we build upon the research undertaken by Jansen et al. [10] that presents close-form expressions for displacements and stresses in a homogeneous two-dimensional reservoir. This project follows the same approach as Jansen et al. [10] using inclusion theory and Green's functions to determine induced stress fields in and around the reservoir as a result of pore pressure changes across faults with non zero throw. We use a simplified model of the subsurface with increasing complexities as a representation of the reservoir and fault geometry as it exists in the field.

1.1. Induced seismicity

Earthquakes are seismic events that result in a sudden release of seismic energy and thus generate seismic waves that can travel long distances. Naturally occurring earthquakes are usually caused by tectonic or volcanic activity in the subsurface. Though most earthquakes are caused naturally, some anthropogenic practices are also known to cause earthquakes. Induced seismicity refers to these human induced earthquakes that can be caused by a variety of anthropogenic activities. The smaller scale induced seismicity in case of hydraulic fracturing, is a desired process used to create fractures in order to increase permeability. However, in the case of hydrocarbon extraction or fluid injection for secondary oil recovery or geothermal applications, it is an undesired side effect. In this report, we study induced seismicity, but we limit our scope to the earthquakes caused by injection or extraction (production) of fluids into or from the subsurface. This entails applications like CCS, geothermal energy, waste water disposal, reservoir floods for secondary oil recovery and hydrocarbon production among others.

Fluid extraction/injection from/into the subsurface has been known to cause induced seismicity in multiple regions throughout the world since the last few decades. While the magnitude of such earthquakes are generally not large enough to pose a serious public health hazard, some of these events can be strong enough (magnitude $M_w > 3.5$) to be felt by local population and cause building damages. There have been few higher magnitude events, like the ones caused by liquid waste disposal in Colorado in 1960s [3], however the magnitude of earthquakes caused by hydrocarbon extraction are typically smaller ($M_w \leq 4.5$). Regardless, the induced seismicity in regions with low to none natural seismic activity, is particularly a matter of concern for the local population and can lead to serious socio-economic problems as is the case in Groningen, The Netherlands. It has thus emerged as a key subject for research aimed at understanding the underlying mechanisms, predicting the behaviour of induced seismicity and mitigating risks associated with it.

1.1.1. Background

Anthropogenic activities have been recorded to cause earthquakes as early as the 1920s [18], with multiple recorded examples of earthquakes caused by several activities including impoundments of large dam reservoirs, nuclear tests, extraction or injection of fluids into the subsurface and so on. Some prominent recorded cases of induced seismicity due to injection of fluids are due to waste water disposal in Rocky Mountain Arsenal, USA [9]; due to waterflooding for oil recovery in Texas, Colorado and Nebraska, USA [24],[20] Alberta, Canada [13], Shandong, China [7]; and due to geothermal projects in New Mexico, USA[24], Puhagan, Phillipines [7]. Extraction of fluids from the reservoir has also been recorded to cause induced earthquakes in multiple regions with the most prominent examples being in Texas, USA and Groningen, Netherlands [24]. Induced seismicity in the Groningen Field, Netherlands, was first recorded in 1991, nearly 3 decades after the commencement of production from the field. While the number and magnitude of induced events remained low and inconsequential until the early 2000s, both have increased since then [28]. With the higher frequency and magnitudes, the earthquakes have become a subject of public concern and controversy, leading to widespread protests and production cuts in Groningen.

1.1.2. Causal mechanisms

In permeable rocks the fluid occupies vacant pore space in the rocks as opposed to impermeable fractured rocks. As a result, changes in pore pressure in the rocks result in stress perturbations in the reservoir and surrounding rocks. Induced seismicity is caused when anthropogenic activities alter the existing state of stress in the subsurface in a specific way that leads to build up of energy and eventual sudden release of that energy. Theoretically, the seismicity can be induced directly by stress changes from anthropogenic activities that are of the same order as ambient stresses, or indirectly when the smaller stress changes caused by anthropogenic activities result in re-activation of pre-existing faults and cause slip [3]. However, the stress changes induced by anthropogenic activities, particularly fluid injection or extraction are not usually of the same order as ambient stresses in the subsurface at typical reservoir depths and the resultant seismicity directly would be of low magnitudes to be consequential. The observed induced seismicity with such activities is thus due to stress changes causing slip along pre-existing faults and fractures. Slip is defined as relative movement of rocks on two sides of a fault surface. Friction between the surfaces prevents the rocks from sliding, however when the stresses build up and exceed a certain threshold, slip is triggered and the potential energy accumulated is suddenly released causing earthquakes.

The shear stress magnitudes across faults in the subsurface are thus constrained by the frictional strength of the faults. Frictional strength of a fault is proportional to the effective normal stresses acting on the surface of the fault. The limiting relation between shear stresses and effective normal stresses that result in slip can be defined by Coulomb criterion. According to Coulomb criterion when the ratio of shear stress to shear resistance exceeds a certain constant value (coefficient of sliding friction, μ) the fault will slip. Shear resistance of a fault is defined as $(\mu(\sigma'_{normal}) + C)$ where C is cohession (In our study, we assume cohesion for the fault to be zero, a generally followed simplifying assumption that does not change the nature of our solution). σ'_{normal} is effective normal stress related to the total normal stresses σ_{normal} as described by the Terzaghi principle [25],

$$\sigma'_{normal} = \sigma_{normal} + \alpha p, \tag{1.1}$$

where α is Biot's coefficient and p is pore pressure. Please note, in this research we follow a sign convention where tensile normal stresses are considered positive and incremental pore pressure is considered positive for injection of fluids or for pore pressure increase, as elaborated further in section (1.4.1). This relation depicts the dependence of fault stability on pore pressure. Changes in pore pressure by extraction or injection of fluids in the vicinity of the fault thus alter the frictional strength of a fault. As a result changes in total normal stress, pore pressure, shear stress or fault friction can thus make a fault unstable and cause slip.

The coefficient of friction μ, typically varies in a typical range from 0.6 to 0.8 [3], and is a function of rock type, depth, temperature and state of the fault among others. The effective coefficient of friction in static conditions is the coefficient of static friction μ_{static}; however when the rocks along a fault have relative movement, the coefficient of friction reduces to what we refer as coefficient of kinetic/dynamic friction

$\mu_{dynamic}$ [11]. We consider the coefficient of friction to be constant, at a relatively lower value $\mu = 0.6$ for our analysis to allow for lower frictional strength and occurrence of slip at lower stress alterations. Under static conditions (before slip), thus, the occurrence of slip is largely dependent on the effective normal stress and shear stress on the fault, as well as pore pressure.

The effective normal stresses can be altered by either changes in the total normal stresses, or by changes in pore pressure. The state of stress in the subsurface is governed by a wide range of factors, namely the depth, weight of overburden, burial history as well as tectonic activity among others. Normal stress on a fault is in turn also dependent on the orientation of the fault. It is thus critical for all geomechanical studies on fault reactivation to have extensive data about the in-situ stress conditions as well as fault orientations. But in-depth knowledge about the in-situ stresses and fault orientations is often not available which limits the validity and accuracy of several geomechanical models of induced seismicity. The pore pressure in the subsurface closely follows the hydrostatic gradient, except when the fluid is of considerably different density, like oil or gas, or when isolated pockets of fluid get trapped in complex rock structures. Extraction or injection of fluids in the subsurface results in changes in the pore pressure and thus in the existing stress patterns. In case of injection, as seen in equation (1.1), pore pressure is expected to increase, thus reducing the effective normal stress across a fault and thus potentially causing slip. In case of production however, the occurrence of slip is not intuitive as depletion of pressure in equation (1.1) should result in increased effective normal stress, thus stabilizing the fault. However, the extraction of fluids associated with widespread seismicity, for instance in Groningen, implies slightly more complex effects of fluid extraction at play that result in seismicity. The induced seismicity in case of extraction of fluids is associated with the poroelastic behaviour of reservoir rock in the subsurface. Upon depletion, the reservoir undergoes contraction which results in changes in strains and stresses in the reservoir. Since the reservoir is enclosed within a much larger domain of rock, the contraction leads to stresses in the surrounding rock as well [24]. The production of natural gas is understood to cause differential deformation/compaction across faults that changes the existing stress field and create conditions for slip, likely the cause of induced seismicity in these regions. We thus try to find the analytical expressions for changes in shear stresses and effective normal stresses due to a change in pore pressure by injection/production of fluids from a reservoir with a displaced fault.

The pre-existing stress conditions, frictional strength of faults as well as pore pressures in the reservoir play a significant role in understanding induced seismicity. In this report, we consider a reservoir with geomechanical properties close to those of the Rotliegend sandstones that form the main reservoir unit in Groningen and nearby hydrocarbon fields in The Netherlands and Germany. We also assume the fault running through the reservoir to be near-critically stressed so as to study the impact of small pore pressure changes on possible seismicity, even though this is not perceived to be the case in the Groningen gas field. A fault is said to be critically stressed when the magnitude of stresses across it reach the value constrained by it's frictional strength and any further increase leads to triggering of slip across the fault. As a result, even small scale changes in the stress field in the reservoir, can thus result in slip in case of near-critically stressed faults. As a result the results are expected to predict slip initiation at lower levels of depletion/injection than it would in the actual reservoir where faults are not near-critically stressed.

1.2. Previous studies on induced stresses and fault slip

In the long history of induced seismicity, much of the attention in earlier days was restricted to induced seismicity due to injection of fluids in the subsurface. Raleigh et al. [19] in 1976 published results from an experiment exploring the feasibility of controlling injection induced seismicity, in the Rangeley oil field, Colorado, US during secondary recovery through waterflooding. The seismicity was monitored for a duration of several months, as a response to varied fluid pressure controlled by injecting/producing water through wells within the observation zone. Lab experiments were used to determine the frictional and mechanical properties and behaviour for the rocks. The study concluded that increased pore pressures are capable of triggering induced earthquakes and also conclusively demonstrated the adequacy of Mohr-Coulomb concept of reduced effective stress in explaining the injection induced seismicity for this case. However, in most cases of moderate injection induced seismicity, it is quite challenging to correlate induced seismicity and injection of fluids accurately, for a variety of factors including poor knowledge about in-situ stresses, inaccuracies in establishing the centre of seismicity and simultaneous injection/production nearby leading to a complex flow patterns [24]. As discussed in section (1.1.2), induced seismicity from depletion of a reservoir is counter-intuitive (to the Coulomb criterion and Terzaghi principle as in equation (1.1)), owing to the stabilizing effect depleting pore pressure or increasing effective normal stress. Geertsma [5] addressed the poroelastic deformations of

rocks under the influence of fluid extraction, but only limited to the scope of mechanical deformations and subsidence.
Segall [21] suggested the poroelastic stressing of rocks to be the cause for depletion induced seismicity. As a result of depletion or outflow of pore fluid rocks undergo contraction. With different degrees of flow and thus contraction in rocks of different permeabilities (reservoir of higher permeability as opposed to sealing overburden, for example) the resultant differential strains and stresses in the formations change the existing stress patterns in the subsurface, which Segall attributed to be the cause for seismicity. Segall [22], based on the work done by Geertsma [6], provided an analytical solution to displacements and stresses in a disc shaped reservoir and was able to demonstrate the solution was applicable to a dome shaped reservoir. Segall made use of Green's functions and demonstrated the displacements caused in the reservoir to be a distribution of centres of dilations with magnitudes proportional to the pore pressure change. Segall [22] correlated the predicted displacement results with data from the Lacq deep-gas field in south-western France and found the results to be in agreement. The resultant stresses induced by pore pressure reduction in such a reservoir were modelled to be of too small a magnitude to induce rock failure and Segall thus argued the pore pressure changes resulting in reactivation of critically stressed faults to be the potential cause of depletion induced seismicity. This finding also highlighted the significance of reliable information on in-situ stress conditions for modelling or predicting induced seismicity.

Building upon the Segall's [22] work on induced seismicity, Pennington et al. [17] proposed differential compaction around pre-existing faults to be the possible causal mechanism for depletion-induced seismicity. They postulated a fault in contact with the reservoir subject to depletion is strengthened and produces a barrier to slip. With incremental depletion, the stress builds up and the locked portions of the fault with high stresses, termed 'asperities', eventually fail resulting in induced seismicity. They also suggested the process is repeated as the pressure continues to fall, with the frequency and size of earthquakes increasing as the asperities possibly increase in size.

Mulders [14] studied the proposed mechanisms by Pennington et al. [17] and numerically modelled gas production in a three-dimensional disk-shaped gas reservoir representative of the Groningen and Annerveen gas fields among other Rotliegend gas fields in the Netherlands. The reservoir modelled was divided into two compartments by a steeply dipping fault. Mulders concluded that for the steeply dipping normal faults in an extensional stress regime, gas depletion led to largely-normal fault slip due to differential compaction. He found the maximum differential compaction to occur when the reservoir geometry has a throw equal to the thickness of the reservoir. He also observed maximum normal fault slip for the scenario with maximum horizontal stress parallel to the strike direction of the fault.

Orlic and Wassing [16] used numerical methods to determine stress changes and fault stability induced by production from gas reservoirs. They used a three-dimensional disk-shaped reservoir with a central fault. They emphasized the impact of reservoir structural setting on the induced stresses, particularly the fault throw. They also concluded the location of highest stress changes and thus fault reactivation to be sections of the fault where the reservoir blocks on either side of the fault are juxtaposed. The study highlighted the significant impact of reservoir geometry on the resultant stresses and fault reactivation. They also studied the effect of presence of a viscoelastic caprock on the induced stresses in order to model the non-homogeneous salt unit commonly observed in Rotliegend reservoirs in the Netherlands and Germany. They concluded that a viscoelastic caprock in close proximity to the reservoir leads to a modified induced stress pattern and enhanced fault slip.

Van Wees et al.[29] reviewed the existing numerical models for depletion induced stresses and presented a three dimensional elasto-plastic geomechanical model for induced seismicity due to production in a simplified Groningen-like reservoir. Their analysis focussed on the gas depletion-induced seismicity in the Netherlands and contextualised it to the findings from generic models for induced seismicity. They calculated the cumulative seismic moment summing the moment for each recorded event from Groningen and observed a non linear increase with production. They then used their geomechanical model to predict the cumulative seismic moment and found it in agreement with the observed non-linear growth. They also used the predictions of delayed onset of seismicity to conclude that the faults in Groningen are most likely not critically stressed. They also concluded that a geomechanical model of differential compaction due to pressure depletion across a non-critically stressed fault can explain the delay in onset of depletion-induced seismicity as well as the non linear growth in seismic moment for the induced seismicity observed in Groningen.

Van den Bogert [26] investigated the initiation of slip and slip behaviour with respect to a variety of modelling parameters namely the fault orientation, in-situ state of stress, fault offset as well as several reservoir and fault properties. Van den Bogert used two-dimensional finite element modelling and conducted sensitivity studies beginning with a simplistic model with a single vertical fault in a reservoir with linear-elastic properties. Bogert also compared the results from finite element modelling with the analytical approach and found the results for a uniform linear-elastic subsurface and uniformly depleting reservoir without offset to be the same for both the approaches. The in-situ stress state, fault orientation, fault cohesion and friction angle were found to significantly influence the onset of slip. Stress patterns and thus the onset of slip was also observed to be strongly dependent on the Poisson's ratio as opposed to the limited impact of Young's modulus. Largest fault throw was found to cause the earliest onset of slip (lowest level of depletion). Another key finding was that the propagation of slip or slip patch growth was found to be accelerated for faults with low offsets.

Buijze et al. [1] presented a 2D plane-strain model for static stress development and reactivation of faults in a reservoir with a displaced fault for depletion case. They used numerical modelling and combined the static analysis up to initiation of slip with full dynamic modelling of the fault rupture and wave propagation. The model was focused on the seismicity in Groningen and thus incorporated the lithologies present in the North of Groningen. The initial state of stress was approximated to measurements from the Groningen field for vertical stress gradient and minifrac tests with a chosen ratio of horizontal to vertical stress $K_0 = 0.72$. A notable consideration was the incorporation of cohesion along with friction coefficient in the fault strength, typically assumed to be 0 in most studies. They found the stresses to be critical at the fault on the top and bottom of the region where reservoir blocks on either side of the fault are juxtaposed (top of hanging wall and base of foot wall). They also found faults with throw to be reactivated at lower levels of depletion compared to faults with zero throw, as the offset between depleting reservoir units was responsible for concentration of stresses at the above mentioned locations. The changes in stress patterns due to a presence of faults with throw were also concluded to significantly impact the size of induced seismic events besides the critical pressure needed for slip.

Haug et al. [8] presented 2D finite element models studying the effect of reservoir depth, thickness, rock properties of the reservoir and surroundings on development of induced stresses and fault reactivation. Haug et al. [8] note the existing analytical studies modelling induced stress patterns are limited to simpler reservoir geometries, or homogeneous material properties. This limits the solutions in a way that heterogeneous distribution of stresses due to fault throw or due to rocks with different mechanical properties juxtaposed across the fault are not accounted for. Building upon the work by Orlic and Wassing [16] on viscoelastic caprock modifying the induced stress patterns and modelling, Haug et al. [8] also checked their results for such a viscoelastic caprock and salt diapir. They concluded that the presence of salt diapir led to favourable conditions for slip locally and salt structures of various thickness above Rotliegend reservoirs to be the possible cause of local concentration of induced seismicity. They found that the tendency to slip was higher for reservoir with steeply dipping faults, for higher reservoir thickness and a shallower position of the reservoir.

1.3. Research objectives

In recent years, induced seismicity from gas production in Groningen and other smaller gas fields in the Netherlands and Northern Germany has been the attention of much public and political debate as well as a subject for extensive research. There is a collective effort to increase the level of understanding about induced seismicity, develop better controls and gain expertise in predicting the nature of seismicity, as evident in the studies covered in the section above. With countries trying to meet agreed upon climate change targets, they are increasingly looking at geothermal energy and CCS (Carbon Capture and Storage) as means to meet those targets. CCS with large volumes of injected fluids is expected to potentially cause induced seismicity problems, with even stronger events than witnessed from hydrocarbon extraction[3]. Increasing geothermal energy efficiency with fluid stimulation is also known to possibly trigger seismic events. Therefore, there is an increasing need to understand the causal mechanisms and to develop technical expertise to be able to precisely model seismicity associated with fluid injection/extraction. This will enable better control on such events and thus better chances of minimizing overall seismicity as well as avoiding damaging events with larger magnitudes. In addition, it helps bridge knowledge gaps in predicting precise locations and magnitudes of future events in existing and planned projects. Studies focussed on dynamic modelling of slip after slip initiation offer insights into the nature of seismicity and scale of seismic events expected, while static modelling offers insights on fault reactivation and prediction of location of seismic events. There have been several numerical studies as covered in the section above, that have successfully modelled the stress development due to production and injection of fluids, in reservoirs with different characteristics both in 2D and in 3D. In our study we derive analytical expressions for stresses for a simplistic three-dimensional reservoir model with a displaced fault.

This analytical analysis is expected to either find results that are qualitatively similar to the ones obtained by previous studies about the stress development and initiation of slip, thus reaffirming the findings analytically as well as refining/sharpening the findings with newer insights, or possibly yield results that are significantly different from the results obtained from previous studies based on numerical approaches. Analytical solutions to the stresses can provide a better alternative in further studies as well, allowing for stress calculation with far less computational resources. In addition, the research incorporates the effects of a full three-dimensional analysis and puts them against the analytical results obtained from 2D plane-strain analysis, thus allowing us to compare how much the stress solutions change qualitatively. If the changes observed are significant, it can be argued that further research into the subject needs to incorporate a three-dimensional stress tensor to predict stress patterns to an acceptable degree of accuracy. However if the results obtained for three-dimensional analysis do not differ much from the qualitative outcomes of plane-strain analysis, it is indicative that future researches on the subject can thus fairly well predict stress behaviour with a plane-strain analysis, thus saving significant amount of time and computational resources, especially in the case of numerical analysis.

Jansen et al. [10] studied the initiation of slip across a fault due to injection and production in a 2D reservoir and derived analytical expressions for resultant displacements and stresses for a plane-strain case. A schematic of the reservoir is depicted in figure (2.1). For a laterally extensive reservoir with dimensions as listed in table (2.2) the stresses were calculated using the derived expressions. To study the initiation of slip, slip boundaries were calculated using Coulomb criterion, with condition of slip in a vertical fault plane given by

$$0 < |\sigma^0_{xy} + \sigma_{xy}| + \mu(\sigma'^0_{xx} + \sigma'_{xx}), \tag{1.2}$$

where μ is the friction coefficient, σ^0_{xy} is initial shear stress, σ'^0_{xx} is initial effective horizontal stress, σ_{xy} and σ'_{xx} are incremental shear and effective horizontal stresses respectively. For the upper half of a two-dimensional reservoir with a displaced fault under plane-strain conditions, with geometry and dimensions as in figure (2.1) and table ((2.2)), the slip boundary given by $\mu(\sigma'^0_{xx}+\sigma'_{xx})$ and the combined shear stress given by $\sigma^0_{xy}+\sigma_{xy}$ were plotted for decreasing incremental pore pressures p (production) as depicted in figure (1.1). The points on the fault ($x = 0$), where the calculated stresses intersect the slip boundary were calculated by solving the following equation for y:

$$\hat{\sigma}_{xy}(0, y) = \sigma_{sl}(y) \tag{1.3}$$

where $\hat{\sigma}_{xy}(0, y)$ is the combined shear stress (initial and incremental as a result of production) and $\sigma_{sl}(y)$ is the slip boundary. For the top half of the reservoir, the intersection heights y_3 and y_4 have been marked for different incremental pore pressures in figure (1.1). The intersections y_3 and y_4 were plotted for decreasing pore pressures pressures, as in figure (1.2), and it was observed that the intersection height $0 < y_3 < a$ decreased increasingly rapidly with pressure. That is, the inner slip patch from the top half of the reservoir was observed to grow rapidly towards the inner slip patch from the bottom half, until they merge as y_3 approaches 0. Further, the combined shear stress at the centre of the fault σ_{valley} ('valley' is the region near the centre of the fault, which in the case of production experienced shear stress exceeding slip threshold at higher levels of depletion, as seen in figure (1.1) from Jansen et al. [10]) was calculated and the pressure at the bottom of the valley for which this combined stress σ_{valley} reaches the corresponding slip boundary $\sigma_{sl}(y_3)$ was derived. Beyond this pressure, p_{merge}, the slip patches theoretically must have merged within the reservoir. Jansen et al. [10] plotted the values for σ_{valley} for different scaled fault throw t/h and observed the magnitude of σ_{valley} increases with the increasing throw. With these observations based on a two-dimensional reservoir model, Jansen et al. [10] predicted the growth of slip patches in the vertical direction. In order to further investigate the finding, we attempt to extend the 2D model to incorporate the effects of the third dimension into the stress equations, so as to capture the possible horizontal propagation of stress.

The main objectives for this study can thus be summarized as below:

1. Derive analytical expressions for induced stresses for a simplistic three-dimensional reservoir with a displaced fault.
2. Calculate induced stresses and slip thresholds using the derived expressions and analyse onset of slip.
3. Compare induced the stress patterns and slip initiation for injection and production.
4. Evaluate the effect of a incorporating a third dimension to the two-dimensional plain-strain analysis for induced stresses in Jansen et al. [10] and also investigate the predicted directions for growth of slip patches by capturing the possible horizontal propagation of stress in third dimension.

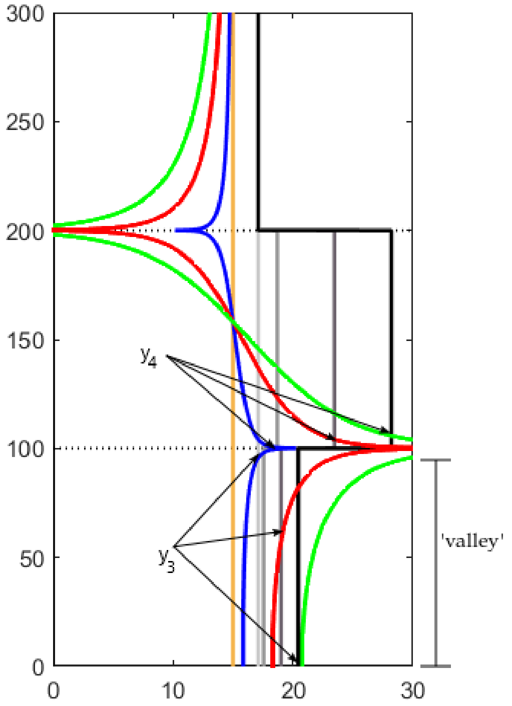

Figure 1.1: From Jansen et al. [10]: Total shear stresses resulting from decreasing incremental reservoir pressures p (production), and corresponding slip boundaries for the top half of a two-dimensional reservoir with a displaced fault as depicted in figure (2.1), under plane-strain conditions with dimensions as listed in table (2.2). Total shear stresses; orange: $p = 0$ MPa, blue: $p = -5$ MPa, red: $p = -20$ MPa, green: $p = -35$ MPa. Slip boundaries; light gray: $p = 0$ MPa, medium gray: $p = -5$ MPa, dark gray: $p = -20$ MPa and black: $p = 35$ MPa. y_3 and y_4 represent the intersections of shear stress and slip boundary for the top half of the reservoir.

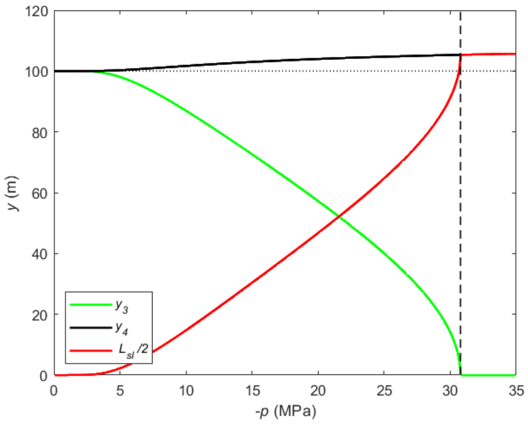

Figure 1.2: From Jansen et al. [10]: Intersections y_3 and y_4 of the shear stress profile with the slip threshold for the upper slip patch, and total slip patch half-length $L_{sl}/2 = y_4 - y_3$ as a function of incremental pressure p during production.

5. Evaluate the effects of geometrical heterogeneity (reservoir thickness) and fault throw on the induced stress patterns and slip initiation.

We approach the outlined objectives by first defining a simplified reservoir geometry with a displaced fault followed by describing the methodology used in deriving expressions for induced stresses. We then compute the resultant stress patterns for the simple reservoir geometry and then for a modified reservoir geometry. Then we use the calculated results to analyse initiation of slip across the fault for production as well as for injection scenarios. We record our observations and then conclude by compiling our findings. In this report, in section (1.4) we list out the simplifying assumptions within our analysis and outline the sign convention. We define the reservoir geometry with drawings depicting the reservoir and the displaced fault in chapter (2). We begin with a two-dimensional reservoir as covered in Jansen et al. [10] and then move onto an increasingly complex reservoir by adding geometrical complexities. In chapter (3) we discuss the methodology behind deriving the analytical expressions for induced stresses. We use the inclusion theory, as postulated by Eshelby [4] to determine the forces an inclusion (reservoir) enclosed in an infinite domain experiences as a result of changes in pore pressure and then we use the Green's function approach used by Segall [22] to determine induced stresses in and outside the reservoir with a displaced fault due to pore pressure changes. Chapter (4) records the results obtained along with our observations and interpretations. The induced stresses are reduced to a scaled dimensionless form to first study the effect of geometrical definition of the reservoir isolated from the effects of elastic properties and the pore pressure. We then study the onset of slip by calculating total shear stresses and slip thresholds given by Coulomb criteria at the fault plane. We conclude by compiling the findings contextualizing them with respect to the stated objectives and previous studies in chapter (5).

1.4. Assumptions

For the purpose of limiting the scope of this study within the constraint of time available, we employ certain limiting assumptions while trying to minimize the impact of those assumptions on the validity and nature of the results obtained. We also employ certain simplifying assumptions in order to approximate the real conditions as close as possible while allowing for ease of calculation and specific analysis of impacts pertaining to an individual complexity, for example like lateral variation in thickness of reservoir. The major assumptions within the analysis are listed below:

1. We assume the domain within which the reservoir is included, is impermeable, i.e does not allow any flow from or to the reservoir. As a result, juxtaposition of reservoir with overburden or underburden acts as a flow barrier.

2. The fault considered is assumed to be non-sealing, therefore allows pressure transmission laterally across the fault within the reservoir. However, we assume no pressure or flow changes to occur in the fault above and below the reservoir.

3. The fault is assumed to be near-critically stressed, that is we assume high initial shear stresses and thus assume suitable horizontal stress values as opposed to using existing ratios of vertical to horizontal stresses. This is to study the effects of minor pore pressure changes in the specific case of near-critically stressed faults.

4. We assume the impermeable domain within which the reservoir is enclosed, to have the same elastic properties as the reservoir.

5. We assume the rocks within reservoir and the domain to behave elastically, and thus we limit our analysis to elastic solutions for stresses in and around the reservoir. In reality, this will not be the case, and there will be inelastic deformations.

6. The coefficient of friction is assumed to be constant, as a simplifying assumption. We chose a lower bound from a typical range of values for coefficient of static friction μ_{static}. The lower estimate ensures we account for slip even at lower levels of injection/production. The selection of coefficient of static friction stays true in the initial state, before changing the pore pressure p. However, upon reduction in stresses post initiation of slip, the frictional strength of fault may reduce and the coefficient of kinetic/dynamic friction is more likely applicable. We also assume the cohesion for fault, C, to be zero.

7. Our model is limited to the stress field generated and thus has been used to analyse the initiation of slip. We however do not take into account the propagation of slip and do not incorporate a model for the seismic waves generated.

1.4.1. Sign convention

Multiple fields of study, follow slightly varying sign conventions pertaining to pore pressures and stresses. As a result, it can be confusing when modelling the initial conditions or analysing the generated results. To avoid any possible confusions, we list the sign convention consistently followed in this research as below:

1. We consider incremental pressure p to be positive for injection of fluids (increase in pore pressure in the subsurface) and thus negative in case of production of fluids (reduction in pore pressure in the subsurface).

2. Tensile normal stresses in this report are considered as positive, while compressive normal stresses are considered negative.

3. Shear stresses in this report are considered as positive for a normal faulting tendency and negative for a reverse faulting tendency.

As part of the plotting convention for this research, while calculating stresses and depicting results for the fault plane ($x = 0$) we consider a point slightly to the right of the fault ($x > 0$).

2
Analytical Model

In this project, we consider a finite reservoir ('inclusion') within an infinite domain ('matrix') for our analysis. The reservoir and the domain are split into two parts through a displaced fault running through the reservoir. We represent the subsurface conditions by a series of models with increasing complexities, beginning with a simpler geometry for ease of solving as well as for isolating the effects of geometry on the resultant expressions for stresses. As discussed in Jansen et al. [10] we first consider a vertical fault under plane-strain conditions, progressing towards inclined faults and three-dimensional strains. The reservoir is subject to injection or production of fluids which results in differential compaction or unequal deformations across the fault. The elastic properties of the reservoir and the domain enclosing the reservoir are considered to be the same, and the elastic coefficients are chosen as the observed in the producing sections of Rotliegend sandstones in Groningen. The elastic coefficients and initial stresses in the reservoir are listed in table (2.1). Typically, the initial stress state is modelled by choosing an appropriate ratio of horizontal to vertical in-situ total normal stresses, with the total vertical stresses governed by the depth and density of overburden as present in the chosen reservoir analogue. However, in our model we assume the fault to be near critically stressed or close to shear failure, and we thus assign values to the total initial horizontal stress σ^0_{xx} (-60 MPa) and initial shear stresses σ^0_{xy} (15 MPa), σ^0_{zx} (0 MPa) so as to allow for the stated assumption.

Table 2.1: Reservoir Properties and Initial Stresses

Symbol	Property	Value	SI Units
G	shear modulus	6500	MPa
p	incremental reservoir pressure	20	MPa
p^0	initial reservoir pressure	35	MPa
α	Biot's coefficient	0.9	-
μ_{st}	static friction coefficient	0.6	-
ν	Poisson's coefficient	0.15	-
σ^0_{xx}	initial horizontal stress in x-direction	-60	MPa
σ^0_{xy}	initial shear stress	15	MPa
σ^0_{zx}	initial shear stress	0	MPa

2.1. Two-Dimensional

For the simplest of models, we consider a plane-strain geometry with unit thickness, in an infinite domain under plane-strain conditions. plane-strain conditions act as a simplifying assumption and are generally accepted as an approximation to the real strain state. A displaced fault of infinite extent and strike direction perpendicular to the plane of the paper, divides the reservoir and the domain in two. The geometry of the reservoir and the fault are depicted in figure (2.1), and the dimensions of the reservoir and fault are listed in table (2.2), with height H, width W and throw t, as follows:

$$H = a + b,$$

$$W = c + d,$$

$$t = b - a,$$

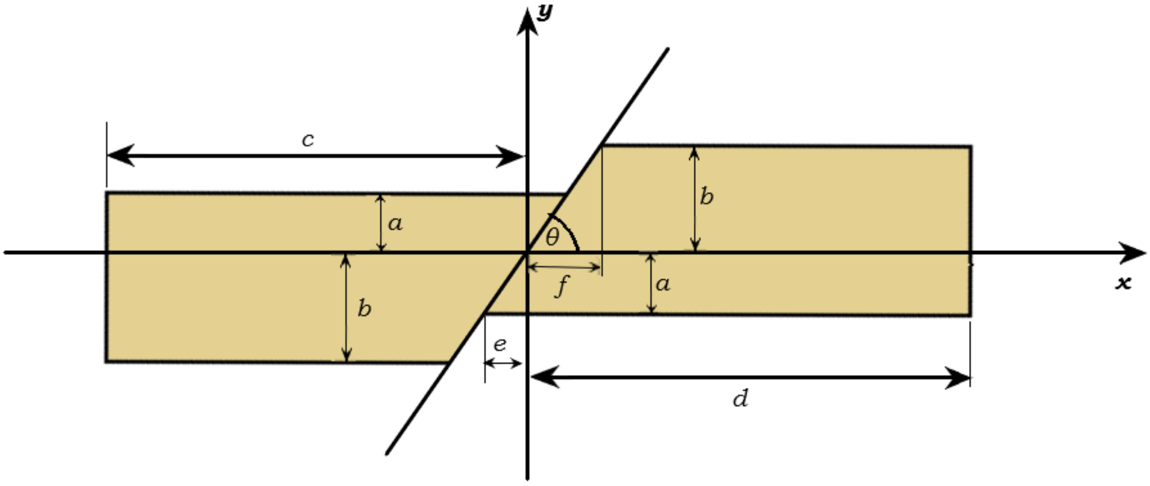

Figure 2.1: Schematic for a two-dimensional reservoir with a displaced normal fault.

Table 2.2: Reservoir and fault dimensions for two-dimensional plane-strain analysis as in Jansen et al. [10]

Symbol	Property	Value	SI Units
a	Reservoir Dimension (Vertical)	100	m
b	Reservoir Dimension (Vertical)	200	m
c	Reservoir Dimension (Horizontal)	∞	m
d	Reservoir Dimension (Horizontal)	∞	m
θ	Fault Dip	$\pi/2$ (Vertical) or $\pi/3$ (Inclined)	rad

2.1.1. Vertical fault

In the simplest model, we assume the fault to be vertical ($\theta = \pi/2$). The vertical fault is a close approximation to steeply dipping faults, as observed in Groningen, Netherlands for instance. For the purpose of arriving at expressions for displacements and stresses, as detailed in the following sections, the reservoir in this simplistic model can be considered as two rectangular units of infinite lateral extent in $x-$ direction, separated by the fault.

2.1.2. Inclined fault

Slightly adding to the model complexity, we consider a reservoir with an inclined fault an an angle θ as listed in table (2.2). The reservoir in this model can be considered as a combination of two trapezoidal units, as depicted in figure (2.1), with

$$f = \frac{b}{\tan(\theta)},$$

$$e = \frac{a}{\tan(\theta)}$$

The analysis for two-dimensional models is not in the scope of this text, and we refer to Jansen et al. [10] for the results and detailed discussions. In this report, we limit our discussion to three-dimensional models, as a follow up from the two-dimensional analysis.

2.2. Three-dimensional

In order to understand the stress patterns across the fault and slip behaviour in a reservoir with three-dimensional stresses, we now consider a three-dimensional model. We consider a domain with a vertical fault parallel to the z-axis ($\theta = \pi/2$) that splits the reservoir and the domain. The three-dimensional geometry represents a closer approximation to actual subsurface geometry. The fault has a throw t, dip θ and runs all along the reservoir in $z-$direction as indicated in the figures (2.2) and (2.2).

$$t = b - a,$$

It is to be noted, in this report, we do not consider a reservoir with an inclined fault, and limit our analysis to a vertical fault. The resultant expressions for a reservoir with an inclined fault are expected to be more complex, however the qualitative results for stresses and slip, as covered in the subsequent sections are expected to be similar, as was observed in the two-dimensional plane-strain analysis covered in Jansen et al. [10]

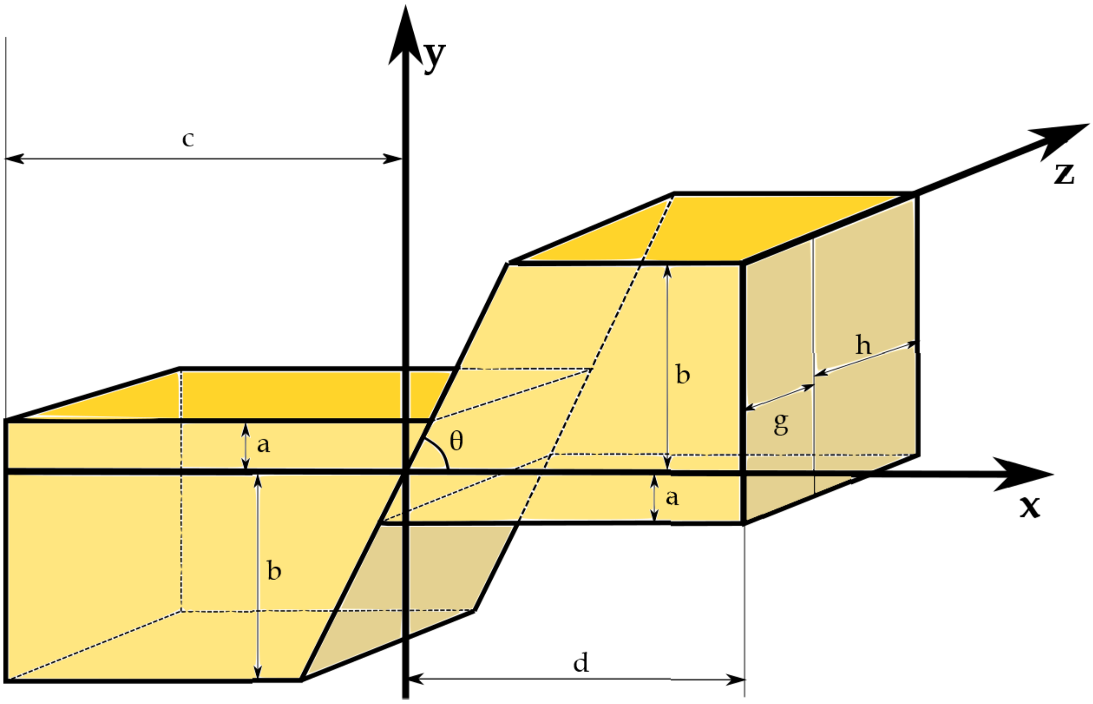

Figure 2.2: Schematic for a three-dimensional symmetrical cuboidal reservoir with a displaced normal fault.

Table 2.3: Reservoir and fault dimensions for three-dimensional analysis

Symbol	Property	Value	SI Units
a	Reservoir Dimension (Vertical)	100	m
b	Reservoir Dimension (Vertical)	200	m
c	Reservoir Dimension (Horizontal)	3000	m
d	Reservoir Dimension (Horizontal)	3000	m
g	Reservoir Dimension (Horizontal)	500	m
h	Reservoir Dimension (Horizontal)	500	m
l	Max. Difference in Res. Thickness	50	m
θ	Fault Dip	$\pi/2$	rad

2.2.1. Symmetrical cuboidal reservoir

We begin with a simpler case of a symmetrical cuboidal reservoir, with height H, width W, thickness T and throw t as below. This geometry represents parallel bedding with no lateral variation in height of the reservoir horizontally. We assume the overlap between the reservoir compartments is uniform in the $z-$direction, and

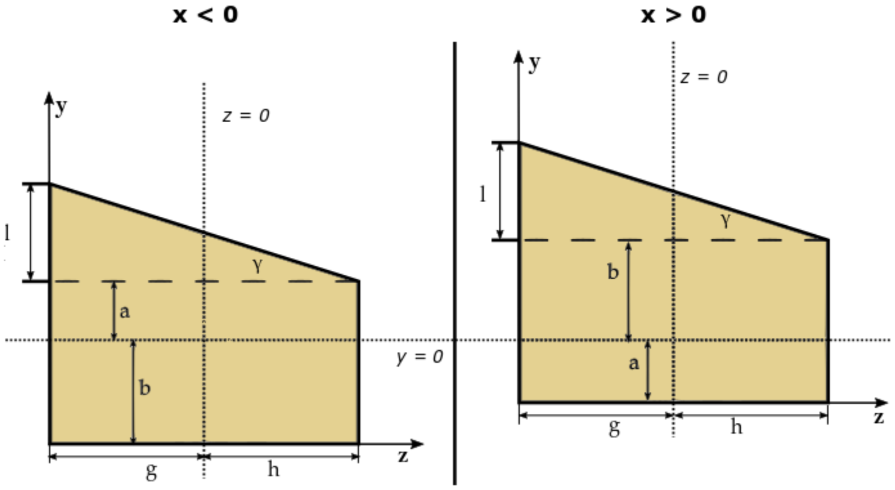

Figure 2.3: Cross section for $x < 0$ *m and* $x > 0$ *m for an asymmetrical laterally thinning reservoir reservoir with a displaced normal fault.*

the reservoir is significantly larger in extent in the $x-$direction with respect to the thickness of the reservoir. The dimensions are as listed in table (2.3).

$$H = a + b,$$

$$W = c + d,$$

$$T = g + h,$$

$$t = b - a,$$

The reservoir in this case has been considered as a combination of two cuboidal units on each side of the fault.

2.2.2. Asymmetrical laterally thinning reservoir

The shape of a reservoir is rarely perfectly cuboidal as in the symmetrical model we considered, owing to the depositional environment and post-depositional processes in the subsurface, and the lateral variation in reservoir height can possibly have a significant effect on stresses induced the fault, as well as slipping behaviour with the introduction of pressure changes by injection/production. In order to capture the effect of lateral variations in height, we introduce a slightly more complex geometry with a varying reservoir height along the $z-$ direction. The thickness of the reservoir is assumed to be linearly decreasing with horizontal distance, as depicted in the figure (2.2), with the maximum difference in height l as listed in table (2.3). For the purpose of stress calculations, the reservoir has been considered as a combination of four units, a set of a cuboid and a wedge placed on top of it, on either side of the fault.

3

Methodology

In this project, we use the combination of concepts of inclusion theory and Green's functions to derive the analytical expressions of induced stresses at any point in the domain as a result of pore pressure changes. Inclusion theory is a theoretical concept used to determine the resultant stresses and strains an enclosed inclusion would experience when subject to a change that results in a tendency to deform the inclusion (eg: change in pressure, temperature etc.). The method is described in detail in the following section. Green's functions are used to determine the displacements at any point due to a point body force at a point within the reservoir. Once the expressions for displacements at a point within and outside the reservoir due to a point body force within the reservoir are obtained, the stresses at any point are calculated using relations from classical mechanics that relate strains to displacements, as well as, stresses to strains. Thereafter, we integrate the expressions over the reservoir, to incorporate the effects of the body forces at all points within the reservoir. The geometry of the models we chose, as described in section (2), governs the dimensions of reservoir and thus the complexities of the integration.

3.1. Inclusion theory

The theory of inclusions was first postulated by Eshelby [4] in 1957 as a method to determine the elastic field resulting from a homogeneous deformation within an isotropic elastic solid ('inclusion') enclosed in an infinite homogeneous isotropic medium ('matrix'). The method involves a sequence of simple imaginary operations of cutting, straining and welding. The inclusion is cut and removed from the matrix and allowed to transform unconstrained. It is restored into its original form by applying surface forces and then re-attaching it to the matrix with the surface forces replaced by equal and opposite body forces.

Injection or production of fluid into a reservoir, due to the poroelastic nature of permeable rocks, results in deformation within the rock that is analogous to a thermal expansion or contraction of a body. Since the reservoir is enclosed in a larger body of rocks in the subsurface, which limits the mechanical deformation in the reservoir, the deformation is expected to be lower than what it would have been if the reservoir were unconstrained. As a result stresses build up inside the reservoir and in the enclosing rocks.

Mura [15] used eigenstrains to describe non-elastic strains such as thermal expansion, phase transformation, initial strains, plastic strains and misfit strains while the eigenstresses referred to stresses caused by these eigenstrains in bodies which are free from any other external force or surface constrain. Eshelby refers to eigenstrains as stress-free transformation strains. In case of inclusions, the stresses caused by constraint from the surrounding elastic medium which prohibits unconstrained deformation are referred to as eigenstresses. In the imaginary step of allowing unconstrained deformation, the strains in the inclusion would thus be eigenstrains. It is important to note that the eigenstrains are non zero within the inclusion and zero outside anywhere in the matrix. The strains resulting after restoring body forces are the elastic strains, that are non zero in the entire matrix.

The procedure as described by Eshelby [4] can be demonstrated with the help of the schematic in figure (3.1). We consider the inclusion, a homogeneous reservoir inside an infinite homogeneous matrix with same elastic properties, subjected to an increase in pore pressure p. The increase in pore pressure results in lower effective stress and thus causes an elastic expansion of the inclusion. The imaginary steps involved in the method are:

1. Cut out the inclusion and allow it to expand freely, without altering the elastic constants, under the effect of increased pore pressure p. Since the expansion is unconstrained, both the inclusion and the matrix are stress free. From generalized Terzaghi Principle relating total stress σ^*_{ij} with effective stress $\sigma^{*'}_{ij}$ and pore pressure p [25],

$$\sigma^*_{ij} = \sigma^{*'}_{ij} - \alpha p \delta_{ij}, \tag{3.1}$$

where α is the Biot's coefficient and δ_{ij} is the Kronecker delta defined as

$$\delta_{ij} = \begin{cases} 1 & \text{if} \quad i = j \\ 0 & \text{if} \quad i \neq j \end{cases} .$$

Note the sign convention used, with pore pressure positive for injection, and compressive normal stresses as negative. Since the total stress is zero, from equation (3.1) we get,

$$\sigma^{*'}_{ij} = \alpha p \delta_{ij}. \tag{3.2}$$

Since the deformation is uniform dilatational (no shear strains) due to unconstrained expansion and the eigenstrain tensor ϵ^* has only diagonal components, given by

$$\epsilon^*_{ij}\delta_{ij} = \frac{\epsilon^*}{3}, \tag{3.3}$$

where volumetric eigenstrain ϵ^* is given by

$$\epsilon^* = \epsilon^*_{xx} + \epsilon^*_{yy} + \epsilon^*_{zz}. \tag{3.4}$$

From Hooke's law with uniform dilation and from equations (3.2), (3.3),

$$\epsilon^*_{ij}\delta_{ij} = \frac{\sigma^{*'}_{ij}}{3K} = \frac{\alpha p}{3K}. \tag{3.5}$$

2. Apply surface forces to the inclusion, to bring it back to the original shape and size before transformation. At this step, the inclusion is in a stressed state with zero strains. The stresses required to bring the inclusion to it's original shape after uniform dilatational deformation are normal stresses given by,

$$\bar{\sigma}^*_{xx} = \bar{\sigma}^*_{yy} = \bar{\sigma}^*_{zz} = \bar{\sigma}^* = -\alpha p, \tag{3.6}$$

with $\bar{\sigma}^*_{ii}$ as the normal stresses and $\bar{\sigma}^*$ representing the average stress at any point in the inclusion. The force **f** on the surface, required to bring back the inclusion to it's original configuration is given by

$$\mathbf{f}(x,y,z) = \bar{\sigma}^* \mathbf{n}_\Gamma(x,y,z) = -\alpha p \, \mathbf{n}_\Gamma(x,y,z), \tag{3.7}$$

where **f** is force vector with three coordinate directions and $\mathbf{n}_\Gamma$ is the unit normal vector.

3. Weld the inclusion back into the matrix, removing the surface forces and applying equal and opposite forces to the matrix. The inclusion is now restored within the matrix and the body forces result in displacement within the inclusion that result in strains and a modified stress state. The displacements, strains and stresses from these forces can be calculated with the help of Green's functions, as detailed in the next section.

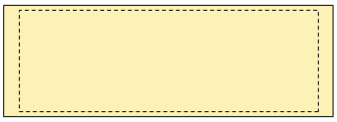

(a) Step 1: Cut out the inclusion and allow it to expand freely under the effect of increased pore pressure p

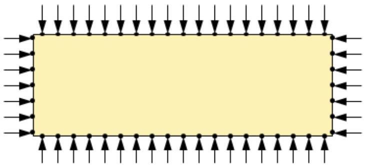

(b) Step 2: Apply suface forces to restore the inclusion to the original shape and size.

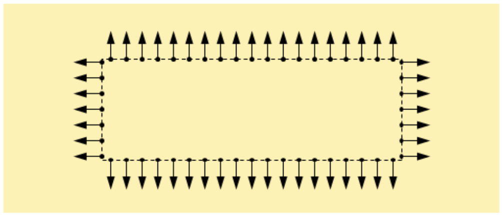

(c) Step 3: Weld the inclusion back into the matrix, remove surface forces and apply equal and opposite forces to the matrix

Figure 3.1: From Jansen et al. [10]: Schematic depicting the imaginary steps involved in calculating displacements in and around an expanding inclusion Ω *in an infinite matrix.*

3.2. Green's functions

Green's functions are mathematical functions used most commonly to solve non homogeneous boundary value problems (ordinary differential equations with initial or boundary conditions). The Green's function is an integral kernel, first developed by George Green, as an impulse response to a linear differential operator for the boundary value problem. The concept has been extensively used as 'the method of Green's functions' in solving equations like the Heat Equation, Wave Equation, Helmholtz's equation and so on. The method of Green's functions allows the use of superposition principle, for a given linear differential operator so that the general solution for an entire domain where the differential operator is defined, is essentially the superimposition of Green's functions for each location within the domain.

The displacement differential equations of the elasticity theory are fundamental equations are obtained by combining kinematic equations (relating displacements and strains), constitutive equations (relating strains and stresses) and equilibrium equations (relating stresses and forces). They are key to determine the state of strain and displacement in a body subject to any given body or surface force. Mura [15] also shows how the displacement field due to eigenstrains ϵ^*_{ij} is equivalent to the displacement field caused by a body force of magnitude which is a function of the eigenstrain ϵ^*_{ij}. Thus, the displacement differential equations are to be solved in order to obtain a displacement field caused by a body force on the inclusion within the matrix, as obtained in the section above.

Several methods have been used to solve the displacement differential equations, like the method of Fourier integrals and stress functions. Love [12] provided a solution using the method of Green's functions to determine the displacement at a point due to a unit body force any point. Once the inclusion is restored and forces reapplied to the matrix as body forces we use triple integrals of this solution to obtain displacement fields and thus stress fields at a point caused by the combined action of point forces at all the points within the inclusion.

The Green's function $\tilde{g}_{ij}(x,y,z,\zeta,\xi,\psi)$ is the component in x_i direction of the displacement at point (x,y,z) due to a unit body force in x_j direction at point (ζ,ξ,ψ), presented in detail in Mura [15]. It can be expressed as

$$\tilde{g}_{ij}(x,y,z,\zeta,\xi,\psi) = \frac{1}{4\pi G}\frac{\delta_{ij}}{\hat{R}} - \frac{1}{16\pi G(1-\nu)}\frac{\partial^2}{\partial x_i \partial x_j}\hat{R}, \tag{3.8}$$

where

$$\hat{R} = \sqrt{(x-\zeta)^2 + (y-\xi)^2 + (z-\psi)^2}. \tag{3.9}$$

The displacement u_i at a point (x,y,z) as a result of all the restoring surface forces of magnitudes as in equation (3.7) can be calculated by integrating over the surface of the inclusion denoted by Γ,

$$u_i(x,y,z) = -\alpha p \iint_\Gamma \tilde{\mathbf{g}}_i(x,y,z,\zeta,\xi,\psi) \cdot \mathbf{n}_\Gamma(\zeta,\xi,\psi)\, d\Gamma, \tag{3.10}$$

where

$$\tilde{\mathbf{g}}_i(x,y,z,\zeta,\xi,\psi) = \begin{bmatrix} \tilde{g}_{ix} \\ \tilde{g}_{iy} \\ \tilde{g}_{iz} \end{bmatrix}. \tag{3.11}$$

The coordinate values ζ, ξ and ψ here refer to locations at the surface of the inclusion Γ.
We use Gauss' divergence theorem to transform the surface integral over Γ to a volume integral within the entire inclusion Ω (as depicted in figure (3.1

$$u_i(x,y,z) = -\alpha p \iiint_\Omega \nabla \cdot \tilde{\mathbf{g}}_\mathbf{i}(\mathbf{x},\mathbf{y},\mathbf{z},\zeta,\xi,\psi)\, \mathbf{d}\Omega, \tag{3.12}$$

The coordinate values ζ, ξ and ψ now refer to the locations within the inclusion or the reservoir. In the following section, we derive the Green's functions for displacements and stresses at any point due to a pressure change p.

3.2.1. Displacements

For the two-dimensional case, refer to Jansen et al. [10] for the methodology. For a three-dimensional reservoir with a vertical fault as described in section (2), the Green's functions for displacement at a point (x,y,z) as a result of unit force at any point within the reservoir (ζ,ξ,ψ) are given by equation (3.8). Using equations (3.10) and (3.12) we can arrive at expressions for displacements at a point (x,y,z) due to body forces (of non-zero magnitude) resultant from a pressure change in the reservoir. To get total displacements (resultant from body forces at each point within the reservoir), we need to integrate the derived expressions over the entire reservoir. However, in order to ease analysis of different geometrical models and following Soltanzadeh and Hawkes [23] we have rearranged the resultant expressions for Green's functions in a generalized form, such that total displacement can be represented in the simplified form :

$$u_i(x,y,z) = D \iiint_\Omega g_i(x,y,z,\zeta,\xi,\psi)\, d\Omega, \tag{3.13}$$

with D as a dimensionless parameter defined as:

$$D(\zeta,\xi) = \frac{(1-2\nu)\alpha p}{2\pi(1-\nu)G}, \tag{3.14}$$

and $g_i(x,y,z,\zeta,\xi,\psi)$ as the Green's functions for displacements at any location within the matrix.
The scaled displacement $G_i(x,y,z)$ is thus defined as

$$G_i(x,y,z) = \frac{u_i(x,y,z)}{D} = \iiint_\Omega g_i(x,y,z,\zeta,\xi,\psi)\, d\Omega. \tag{3.15}$$

From equations (3.15) and (3.12) we can thus derive

$$\iiint_\Omega g_i(x,y,z,\zeta,\xi,\psi)\, d\Omega = \frac{-\alpha p}{D} \iiint_\Omega \nabla \cdot \tilde{\mathbf{g}}_\mathbf{i}(x,y,z,\zeta,\xi,\psi)\, d\Omega, \tag{3.16}$$

or

$$g_i(x,y,z,\zeta,\xi,\psi) = -\frac{2\pi(1-\nu)G}{(1-2\nu)}\left(\nabla\cdot\tilde{\mathbf{g}}_{\mathbf{i}}(x,y,z,\zeta,\xi,\psi)\right). \tag{3.17}$$

Thus in a three-dimensional model, the resultant Green's functions $g_i(x,y,z,\zeta,\xi,\psi)$ for displacements at any point (x,y,z) due to a body force at point (ζ,ξ,ψ) within the reservoir resulting from a pressure change p, are:

$$g_x(x,y,z,\zeta,\xi,\psi) = \frac{x-\zeta}{4\hat{R}^3}, \tag{3.18}$$

$$g_y(x,y,z,\zeta,\xi,\psi) = \frac{y-\xi}{4\hat{R}^3}, \tag{3.19}$$

$$g_z(x,y,z,\zeta,\xi,\psi) = \frac{z-\psi}{4\hat{R}^3}. \tag{3.20}$$

The total displacements at any point can be found by integrating these Green's functions for each individual model described in section (2). The Green's functions thus obtained have also been used in a similar fashion to obtain Green's functions for stresses at any point in the domain, as detailed in the next section.

3.2.2. Stresses

To arrive at expressions for stress field resultant from the body forces after the inclusion is welded back into the matrix, we use three-dimensional equations from classical mechanics that relate the stresses to resultant displacement. The three-dimensional stress tensor at any point is related to the three-dimensional strain tensor by the constitutive equations. For an isotropic solid, the constitutive equation in terms of Lamé parameters λ and μ is:

$$\sigma_{xx}(x,y,z) = \lambda\delta_{ij}\epsilon_{kk}(x,y,z) + 2\mu\left(\epsilon_{ij}(x,y,z)\right), \tag{3.21}$$

where $\epsilon_{kk} = \epsilon_{xx} + \epsilon_{yy} + \epsilon_{zz}$ is the volumetric strain.

Using $\lambda = \frac{2\mu\nu}{(1-2\nu)}$ and $\mu = G$,

$$\begin{aligned}
\sigma_{xx}(x,y,z) &= A\left[\epsilon_{xx}(x,y,z) + B\left(\epsilon_{yy}(x,y,z) + \epsilon_{zz}(x,y,z)\right)\right],\\
\sigma_{yy}(x,y,z) &= A\left[\epsilon_{yy}(x,y,z) + B\left(\epsilon_{xx}(x,y,z) + \epsilon_{zz}(x,y,z)\right)\right],\\
\sigma_{zz}(x,y,z) &= A\left[\epsilon_{zz}(x,y,z) + B\left(\epsilon_{xx}(x,y,z) + \epsilon_{yy}(x,y,z)\right)\right],\\
\sigma_{xy}(x,y,z) &= 2G\epsilon_{xy}(x,y,z),\\
\sigma_{yz}(x,y,z) &= 2G\epsilon_{yz}(x,y,z),\\
\sigma_{xz}(x,y,z) &= 2G\epsilon_{xz}(x,y,z),
\end{aligned} \tag{3.22}$$

such that

$$\begin{aligned}
A &= E\frac{(1-\nu)}{(1+\nu)(1-2\nu)},\\
B &= \frac{\nu}{(1-\nu)},
\end{aligned}$$

where E = Young's modulus, G = shear modulus and ν = Poisson's ratio. The $\epsilon_{ij}(x,y,z)$ in equation (3.22) represent total strains, which are related to resultant displacements as:

$$\epsilon_{ij}(x,y,z) = \frac{1}{2}\left(\frac{\partial u_i(x,y,z)}{\partial x_j} + \frac{\partial u_j(x,y,z)}{\partial x_i}\right). \tag{3.23}$$

Combining equations (3.23), (3.22) and (3.13) we arrive the expressions for resultant stresses, which can be rearranged in terms of Green's functions for stresses g_{ij} as:

$$\sigma_{ij}(x,y,z) = C\left[\iiint_\Omega g_{ij}(x,y,z,\zeta,\xi,\psi)\,d\Omega - 2\pi\delta_\Omega\delta_{ij}\right], \tag{3.24}$$

where the scaling parameter C is defined as

$$C = GD, \tag{3.25}$$

and δ_Ω is modified Kronecker delta defined as:

$$\delta_\Omega = \begin{cases} 1 & \text{if} \quad (x,y)\in\Omega \\ 0 & \text{if} \quad (x,y)\notin\Omega \end{cases}. \tag{3.26}$$

Thus, the resultant Green's functions for stresses at any point (x, y, z) due to a point body force at any point(ζ, ξ, ψ) resulting from a pore pressure change p are:

$$\begin{aligned}
g_{xx}(x,y,z,\zeta,\xi,\psi) &= \frac{\hat{R}^2 - 3(x-\zeta)^2}{2\hat{R}^5},\\
g_{yy}(x,y,z,\zeta,\xi,\psi) &= \frac{\hat{R}^2 - 3(y-\xi)^2}{2\hat{R}^5},\\
g_{zz}(x,y,z,\zeta,\xi,\psi) &= \frac{\hat{R}^2 - 3(z-\psi)^2}{2\hat{R}^5},\\
g_{xy}(x,y,z,\zeta,\xi,\psi) &= \frac{3}{2\hat{R}^5}(x-\zeta)(y-\xi),\\
g_{yz}(x,y,z,\zeta,\xi,\psi) &= \frac{3}{2\hat{R}^5}(y-\xi)(z-\psi),\\
g_{zx}(x,y,z,\zeta,\xi,\psi) &= \frac{3}{2\hat{R}^5}(x-\zeta)(z-\psi),
\end{aligned} \tag{3.27}$$

with $\hat{R}$ as defined in equation (3.9). As in the case of total displacements, the induced stresses at any point can thus be found by integrating the Green's functions for stress at a point, over the entire reservoir Ω.

3.3. Induced stresses

As the pore pressure changes inside the inclusion, the inclusion is subject to a uniform body force as it is constrained within the matrix. The Green's functions $g_i(x,y,z,\zeta,\xi,\psi)$ and $g_{ij}(x,y,z,\zeta,\xi,\psi)$ derived in the section above represent displacements $u_i(x,y,z,\zeta,\xi,\psi)$ and stresses $\sigma_{ij}(x,y,z,\zeta,\xi,\psi)$ that will be caused by a body force of magnitude given by equation (3.7) acting at the point (ζ,ξ,ψ) . The induced stresses σ_{ij} at that point are basically the combined stresses at that point, due to body forces acting at each such point within the reservoir. Thus, from the Green's functions obtained in the above section, we can now calculate the induced stresses at any point in the domain by integrating them over the reservoir Ω.

3.3.1. Cuboidal reservoir

For the cuboidal model described in section (2.2.1), we divided the reservoir in two cuboidal units with general dimensions defined by p,q,r,s,m,n as depicted in figure (3.2), we have from equation (3.24) for each cuboidal unit,

$$\sigma_{ij}(x,y,z) = C\left[\int_m^n \int_r^s \int_p^q g_{ij}(x,y,z,\zeta,\xi,\psi)d\zeta d\xi d\psi - 2\pi\delta_\Omega\delta_{ij}\right], \tag{3.28}$$

or

$$\sigma_{ij}(x,y,z) = C\left[G_{ij}(x,y,z) - 2\pi\delta_\Omega\delta_{ij}\right], \tag{3.29}$$

with $G_{ij}(x,y,z)$, the integrals of Green functions at any point (x,y,z) defined as:

$$G_{ij}(x,y,z) = \int_m^n \int_r^s \int_p^q g_{ij}(x,y,z,\zeta,\xi,\psi)\, d\zeta d\xi d\psi. \tag{3.30}$$

3.3.2. Thinning reservoir

Similarly, for a reservoir with laterally varying height as in section (2.2.2), equation (3.30) is modified to include the wedge shaped unit on top of the existing cuboidal reservoir unit. The dimensions of the wedge shaped unit are defined by p,q,s,s',m,n as in figure (3.3). The resultant integrals for Green's functions $G_{ij}(x,y,z)$ are thus obtained as follows:

$$G_{ij}(x,y,z) = \int_m^n \int_r^s \int_p^q g_{ij}(x,y,z,\zeta,\xi,\psi)\, d\zeta d\xi d\psi + \int_m^n \int_s^{s+(n-\psi)\tan\gamma} \int_p^q g_{ij}(x,y,z,\zeta,\xi,\psi)\, d\zeta d\xi d\psi, \tag{3.31}$$

where

$$\gamma = \arctan\frac{s' - s}{n-m}. \tag{3.32}$$

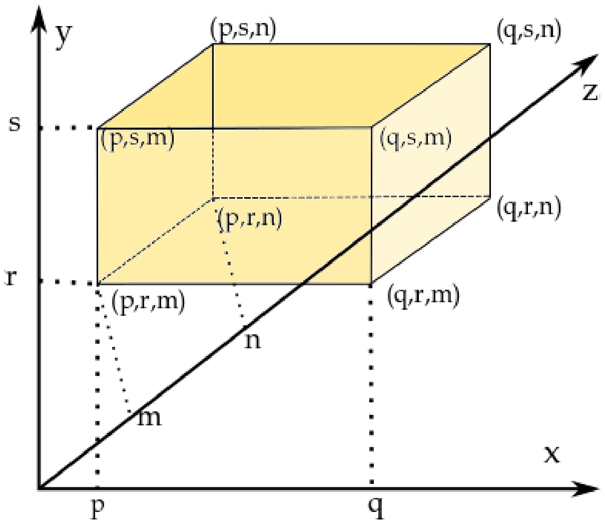
y
(p,s,n)
(q,s,n)
z
s
(p,s,m)
(q,s,m)
(p,r,n)
(q,r,n)
r
(p,r,m)
(q,r,m)
n
m
x
p
q

Figure 3.2: Cuboidal unit used as the integration unit for a symmetrical cuboidal reservoir

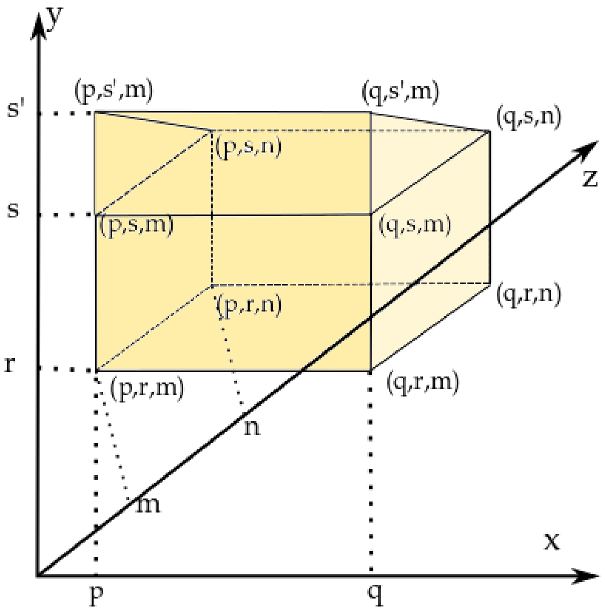
y
(p,s',m)
(q,s',m)
s'
(q,s,n)
(p,s,n)
z
s
(p,s,m)
(q,s,m)
(p,r,n)
(q,r,n)
r
(p,r,m)
(q,r,m)
n
m
x
p
q

Figure 3.3: Cuboidal unit with a wedge shaped unit on top used as the integration unit for an asymmetrical laterally thinning reservoir

4

Results and Discussion

4.1. Stresses

The integrals of Green's functions for induced stresses, defined in equations (3.30) and (3.31), are calculated at each point within the reservoir and in the enclosing domain in the immediate vicinity of the reservoir. We calculate dimensionless stresses, defined as $\frac{\sigma_{ij}(x,y,z)}{C}$, from the calculated integrals of Green's functions as follows(from equation (3.24)) :

$$\frac{\sigma_{ij}(x,y,z)}{C} = G_{ij}(x,y,z) - 2\pi\delta_{\Omega}\delta_{ij}, \tag{4.1}$$

with the scaling parameter C defined in equation (3.25):

$$C = GD = \frac{(1-2\nu)\alpha p}{2\pi(1-\nu)}. \tag{4.2}$$

4.1.1. Cuboidal

In the example of symmetrical cuboidal reservoir the integral for Green's function's $G_{ij}(x,y,z)$ for the whole reservoir with dimensions as in table (2.3) is the sum of integral for both the cuboidal units as described in the section (3.3.1). From equation (3.30),

$$G_{ij}(x,y,z) = \int_{-g}^{h}\int_{-b}^{a}\int_{-c}^{0} g_{ij}(x,y,z,\zeta,\xi,\psi)\,d\zeta d\xi d\psi + \int_{-g}^{h}\int_{-a}^{b}\int_{0}^{d} g_{ij}(x,y,z,\zeta,\xi,\psi)\,d\zeta d\xi d\psi. \tag{4.3}$$

The resultant integrals of Green's functions for induced stresses, $G_{ij}(x,y,z)$ at any point defined by the coordinates (x,y,z) in or outside the reservoir as depicted in the schematic (2.2), are listed in the Appendix A. As can be seen, the resultant expressions for shear stresses are functions of the inverse hyperbolic tangents, while the expressions for normal stresses are functions of inverse tangent functions. It is to be noted, the pore pressure component of the stresses has been incorporated into the scaling parameter, thus the stress integrals $G_{ij}(x,y,z)$ and the dimensionless stresses, $(G_{ij}(x,y,z) - 2\pi\delta_{\Omega}\delta_{ij})$ are independent of the pore pressure. As a result, the expressions are the same for both production and injection. Dimensionless stresses from equation (4.1) have been plotted for the fault plane ($x = 0$ or yz plane) to depict the stress development at the fault plane. The dimensionless stresses have also been plotted for the $z = 0$ (xy) plane and $y = 0$ (zx) plane for better visualisation, and the plots are depicted in figures (4.1), (4.2) and (4.3).

The figures depict stresses in the near fault region (-500 m $< x <$ 500 m), so as to depict the stress patterns away from the horizontal boundaries. Please note that the dimensionless stresses, independent of the pore pressure, depict direction of stresses corresponding to positive incremental pressures, p , or injection. For production, negative incremental pressures will result in sign inversion of the actual stresses $\sigma_{ij}(x,y,z)$. For injection, we observe that the reservoir expectedly undergoes expansion, and this in turns leads to perturbation in the state of stress around the reservoir. The figures reflect a very similar stress field as observed in our two-dimensional plane-strain analysis, covered in Jansen et al. [10]. Dimensionless horizontal stress $\frac{\sigma_{xx}}{C}$, dimensionless vertical stress $\frac{\sigma_{yy}}{C}$ and dimensionless shear stress in vertical direction $\frac{\sigma_{xy}}{C}$ on the $xy(z=0)$ plane are similar to those obtained for the plane-strain case, both qualitatively as well as quantitatively. Negative (compressive) horizontal stresses in the directions parallel as well as normal to the fault plane, caused by positive incremental pressures (injection) or expanding reservoir, are consistent with the findings in the two-dimensional case. The four peaks at the boundaries where reservoir juxtaposes overburden/overburden in the dimensionless shear stress $\frac{\sigma_{xy}}{C}$ are also consistent with plane-strain analysis. For the $x = 0$ (yz) plane, the results are similar to the dimensionless stresses obtained on the fault for the plane-strain case, only laterally extended in the newly introduced z-direction (refer to figures (6), (7), (8) in Jansen et al. [10]). The expressions for integrals, $G_{xx}(x, y, z)$, $G_{yy}(x, y, z)$ and $G_{xy}(x, y, z)$ were checked for an infinite reservoir in the z-direction, and we obtained the same expressions as those obtained for a two-dimensional reservoir in the plane-strain case. Note that the solutions for shear stress $G_{xy}(x, y, z)$ obtained as listed in Appendix A, have singularities at reservoir boundaries at exactly $y = \pm 100$ m and $y = \pm 200$ m on the fault plane $(x = 0$ m$)$ that result in infinite peaks in shear stress at the reservoir boundaries $(-\infty$ at $y = \pm 100$ m and ∞ at $y = \pm 200$ m$)$. We limit the infinite peaks obtained while plotting by choosing a point slightly above or below the exact boundary and by choosing a point slightly to the right of the fault.

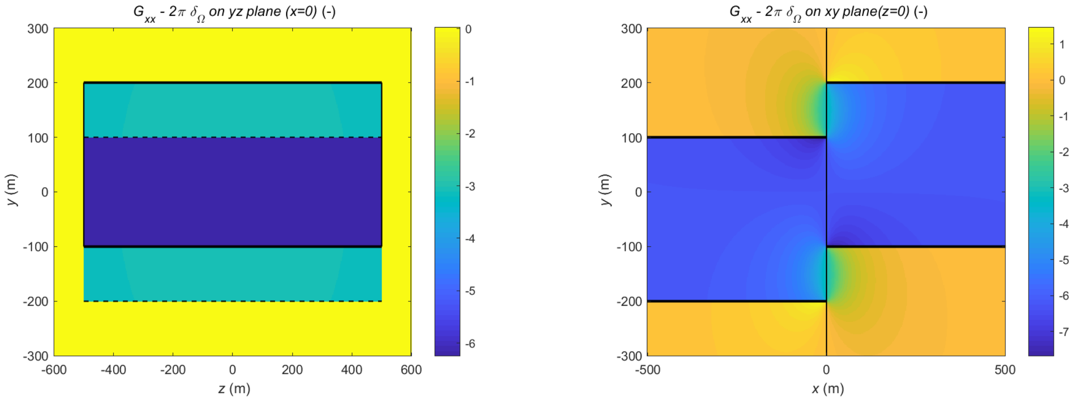

(a) Dimensionless normal stress $\frac{\sigma_{xx}}{C}$ on the yz plane (Symmetrical)

(b) Dimensionless normal stress $\frac{\sigma_{xx}}{C}$ on the xy plane (Symmetrical)

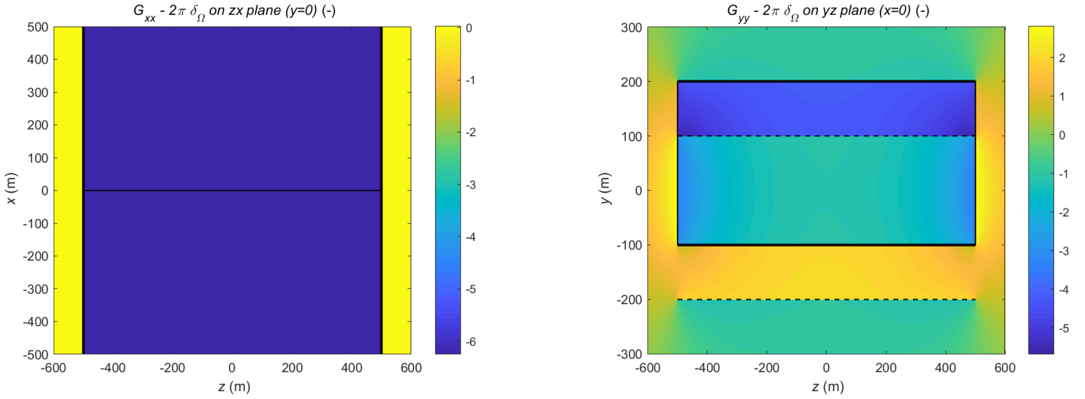

(c) Dimensionless normal stress $\frac{\sigma_{xx}}{C}$ on the zx plane (Symmetrical)

(d) Dimensionless normal stress $\frac{\sigma_{yy}}{C}$ on the yz plane (Symmetrical)

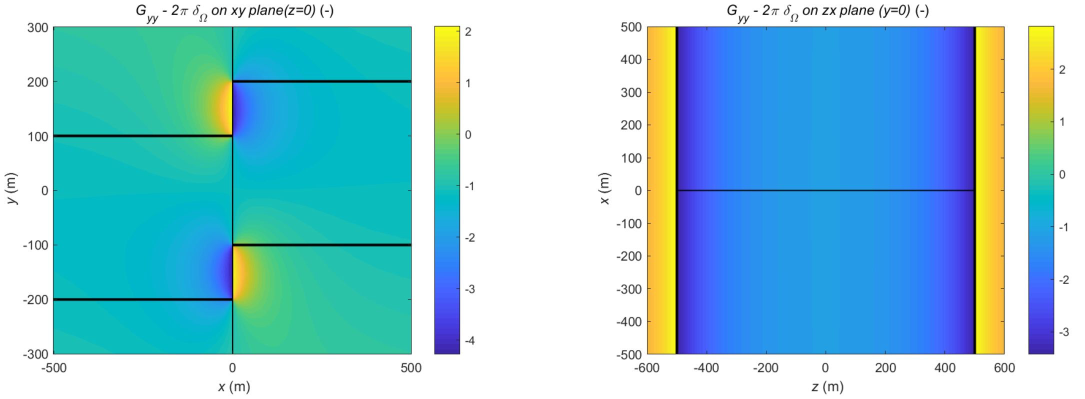

(e) Dimensionless normal stress $\frac{\sigma_{yy}}{C}$ on the xy plane (Symmetrical)

(f) Dimensionless normal stress $\frac{\sigma_{yy}}{C}$ on the zx plane (Symmetrical)

Figure 4.1: Dimensionless normal stresses $\frac{\sigma_{xx}}{C}$ *and* $\frac{\sigma_{yy}}{C}$ *at the planes corresponding to* $x = 0$, $y = 0$ *and* $z = 0$, *with the scaling parameter* $C = 2.36 \times 10^6 N/m^2$ *as defined in equation* (3.25), *for a symmetrical cuboidal reservoir with dimensions as listed in table (2.3).*

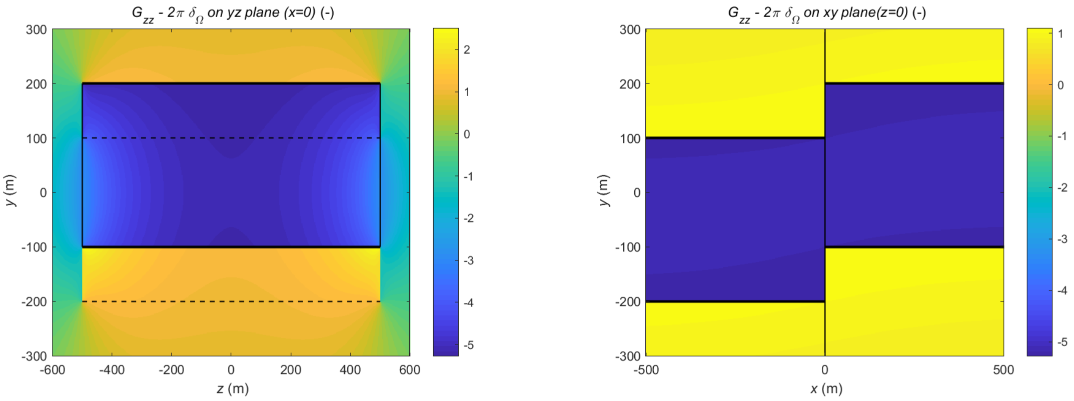

(a) Dimensionless normal stress $\frac{\sigma_{zz}}{C}$ on the yz plane (Symmetrical)

(b) Dimensionless normal stress $\frac{\sigma_{zz}}{C}$ on the xy plane (Symmetrical)

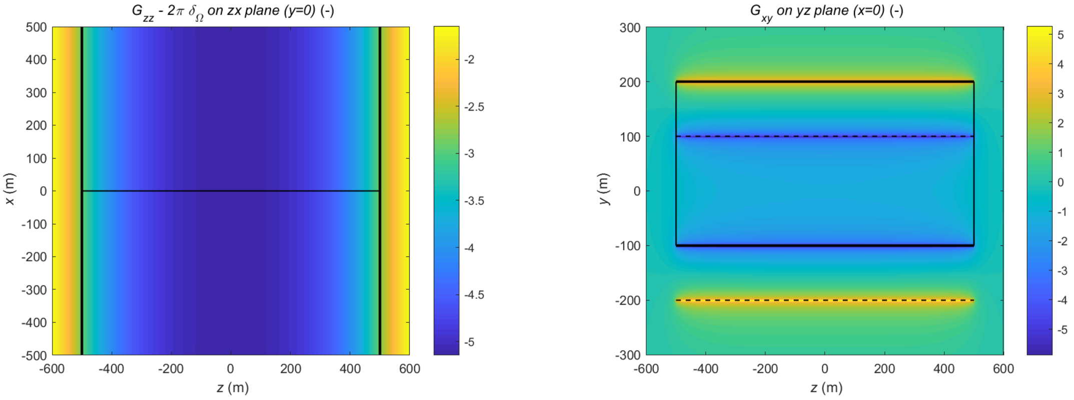

(c) Dimensionless normal stress $\frac{\sigma_{zz}}{C}$ on the zx plane (Symmetrical)

(d) Dimensionless shear stress $\frac{\sigma_{xy}}{C}$ on the yz plane (Symmetrical)

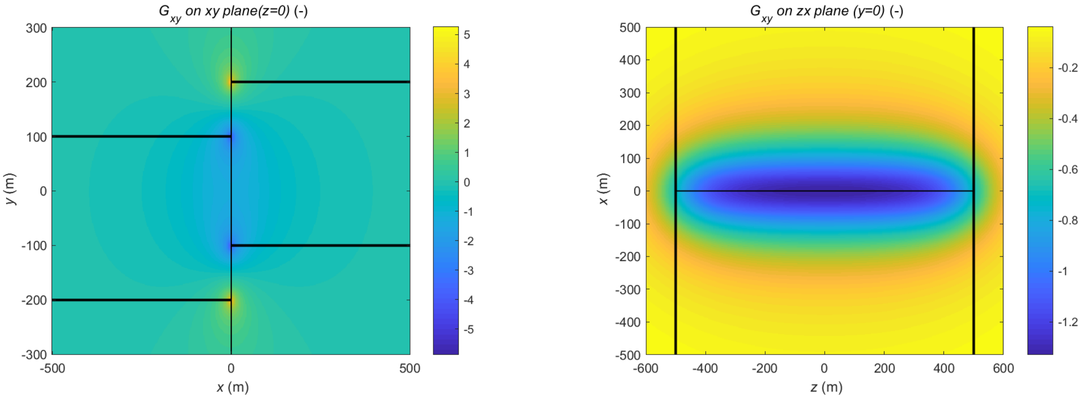

(e) Dimensionless shear stress $\frac{\sigma_{xy}}{C}$ on the xy plane (Symmetrical)

(f) Dimensionless shear stress $\frac{\sigma_{xy}}{C}$ on the zx plane (Symmetrical)

Figure 4.2: Dimensionless normal stress $\frac{\sigma_{zz}}{C}$ *and Dimensionless shear stress* $\frac{\sigma_{xy}}{C}$ *at the planes corresponding to* $x = 0$, $y = 0$ *and* $z = 0$, *with the scaling parameter* $C = 2.36 \times 10^6 N/m^2$ *as defined in equation* (3.25), *for a symmetrical cuboidal reservoir with dimensions as listed in table (2.3).*

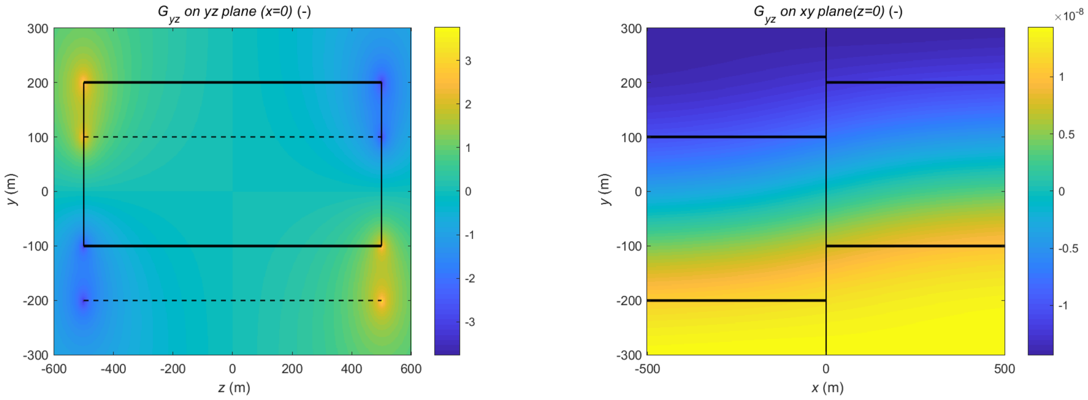

(a) Dimensionless shear stress $\frac{\sigma_{yz}}{C}$ on the yz plane (Symmetrical)

(b) Dimensionless shear stress $\frac{\sigma_{yz}}{C}$ on the xy plane (Symmetrical)

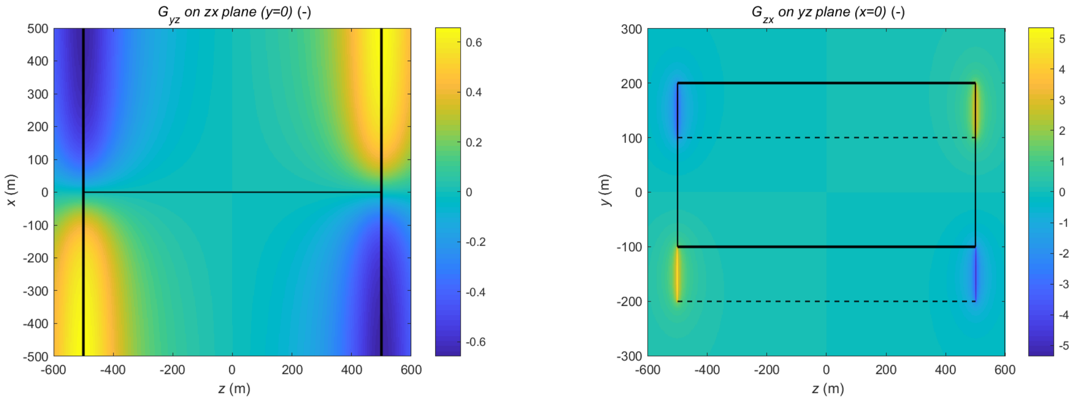

(c) Dimensionless shear stress $\frac{\sigma_{yz}}{C}$ on the zx plane (Symmetrical)

(d) Dimensionless shear stress $\frac{\sigma_{zx}}{C}$ on the yz plane (Symmetrical)

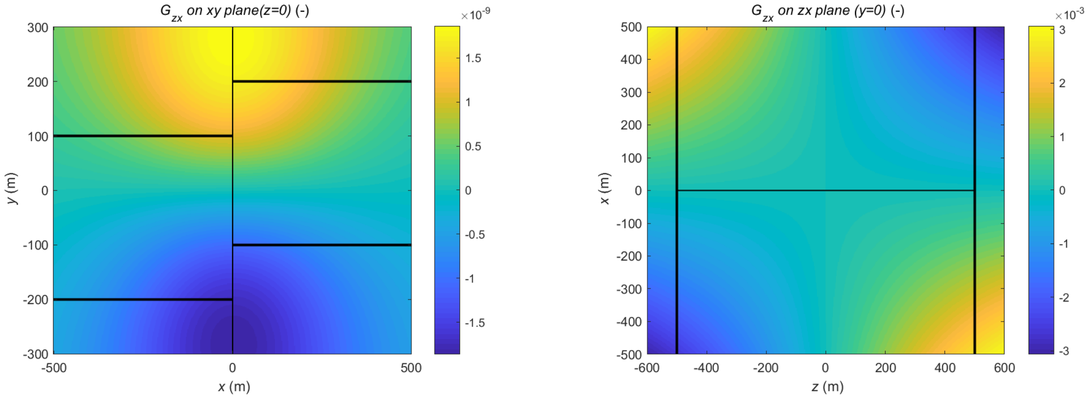

(e) Dimensionless shear stress $\frac{\sigma_{zx}}{C}$ on the xy plane (Symmetrical)

(f) Dimensionless shear stress $\frac{\sigma_{zx}}{C}$ on the zx plane (Symmetrical)

Figure 4.3: Dimensionless shear stresses $\frac{\sigma_{yz}}{C}$ *and* $\frac{\sigma_{zx}}{C}$ *at the planes corresponding to* $x = 0$, $y = 0$ *and* $z = 0$, *with the scaling parameter* $C = 2.36 \times 10^6 N/m^2$ *as defined in equation* (3.25), *for a symmetrical cuboidal reservoir with dimensions as listed in table (2.3).*

4.1.2. Asymmetrical/laterally thinning reservoir

In order to incorporate the effects of non-uniform reservoir thickness in actual conditions the model is updated to incorporate an asymmetrical laterally thinning reservoir, with a uniform decrease in height in the $z-$direction. Dimensionless stresses, $(G_{ij}(x,y,z) - 2\pi\delta_{\Omega}\delta_{ij})$, are also calculated for the asymmetrical reservoir however the integrals have only been performed analytically in two dimensions, owing to the mathematically complex integrals in the third dimension. To obtain the resultant dimensionless stresses the third integration has been performed numerically. The resultant expressions after two-dimensional analytical integration have been listed in the Appendix (B). For the asymmetrical laterally thinning reservoir the integral for Green's function's $G_{ij}(x,y,z)$ for the whole reservoir with dimensions as in table (2.3) is the sum of integral for both the cuboidal units and both wedge shaped units as described in the section (3.3.2). From equation (3.31),

$$\begin{aligned} G_{ij}(x,y,z) = &\int_{-g}^{h}\int_{-b}^{a}\int_{-c}^{0} g_{ij}(x,y,z,\zeta,\xi,\psi)\, d\zeta d\xi d\psi + + \int_{-g}^{h}\int_{a}^{a+(h-\psi)\tan\gamma}\int_{-c}^{0} g_{ij}(x,y,z,\zeta,\xi,\psi)\, d\zeta d\xi d\psi \\ &\int_{-g}^{h}\int_{-a}^{b}\int_{0}^{d} g_{ij}(x,y,z,\zeta,\xi,\psi)\, d\zeta d\xi d\psi + \int_{-g}^{h}\int_{b}^{b+(h-\psi)\tan\gamma}\int_{0}^{d} g_{ij}(x,y,z,\zeta,\xi,\psi)\, d\zeta d\xi d\psi, \end{aligned}$$

where

$$\gamma = \arctan\frac{s^{'} - s}{n-m}. \tag{4.4}$$

The induced stresses are calculated, as in the case for symmetrical reservoir, slightly to the right of the $x = 0$ (yz) or fault plane as well as the $y = 0$ (xz) plane and the $z = 0$ (zy) plane for better visualisation of the stress patterns. Figures (4.4), (4.5) and (4.6) depict the dimensionless stresses $(G_{ij}(x,y,z) - 2\pi\delta_{\Omega}\delta_{ij})$ for an asymmetrical reservoir with uniform height reduction in the lateral direction, with dimensions as given in table (2.3). The maximum reduction in height is denoted by l and in our analysis fixed at $l = 50$ m. The results obtained are qualitatively similar to the dimensionless stress patterns as observed for the symmetrical cuboidal reservoir. We check the expressions obtained after integrals in the first two dimensions subjected to the limit l approaching 0 or $\lim_{l\to 0} G_{ij}(x,y,z)$. We observe the resultant expressions are the same as obtained after integrals in two dimensions for a cuboidal reservoir. The resultant dimensionless stresses obtained are also the same as in the case of symmetrical cuboidal reservoir for $l = 0$. We also check the solutions for shear stress $G_{xy}(x,y,z)$ for an asymmetrical reservoir for singularities at reservoir boundaries at exactly $y = \pm 100$ m and $y = \pm 200$ m on the fault plane ($x = 0$ m), and we find infinite peaks in shear stress at these reservoir boundaries. We thus limit the infinite peaks obtained while plotting by choosing a point slightly above or below the exact boundary and by choosing a point slightly to the right of the fault as in the case for a cuboidal reservoir.

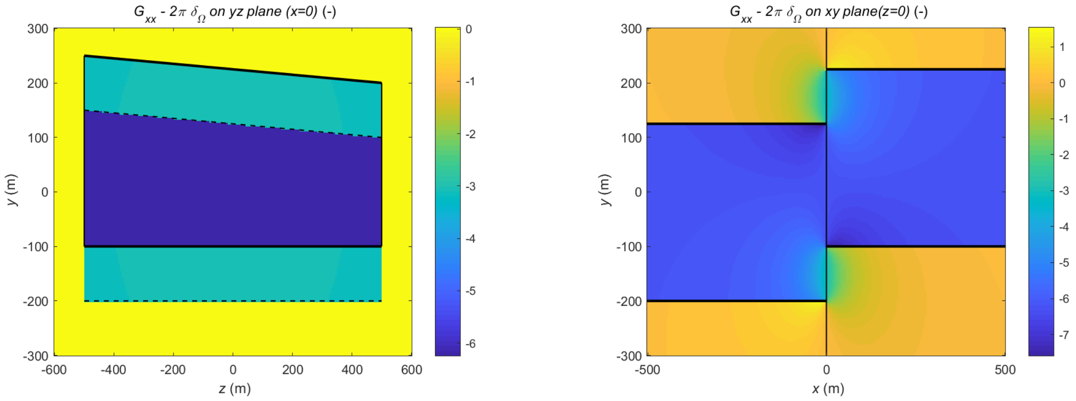

(a) Dimensionless normal stress $\frac{\sigma_{xx}}{C}$ on the yz plane (Asymmetrical)

(b) Dimensionless normal stress $\frac{\sigma_{xx}}{C}$ on the xy plane (Asymmetrical)

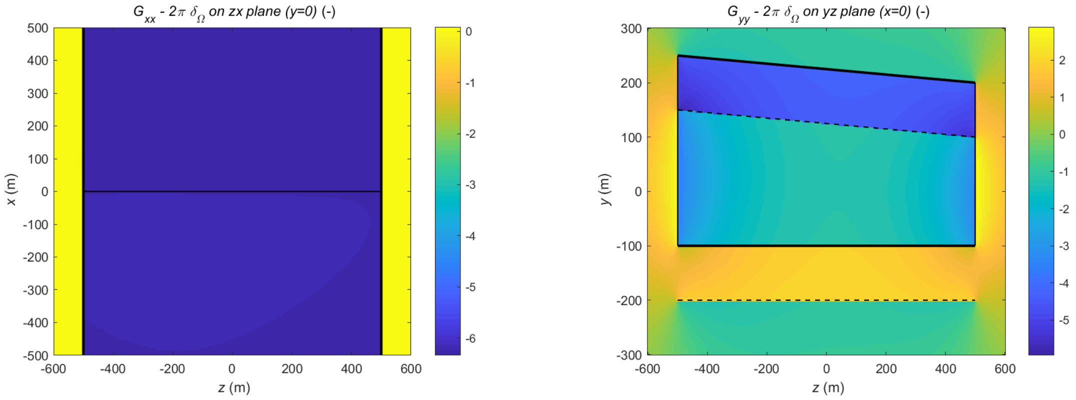

(c) Dimensionless normal stress $\frac{\sigma_{xx}}{C}$ on the zx plane (Asymmetrical)

(d) Dimensionless normal stress $\frac{\sigma_{yy}}{C}$ on the yz plane (Asymmetrical)

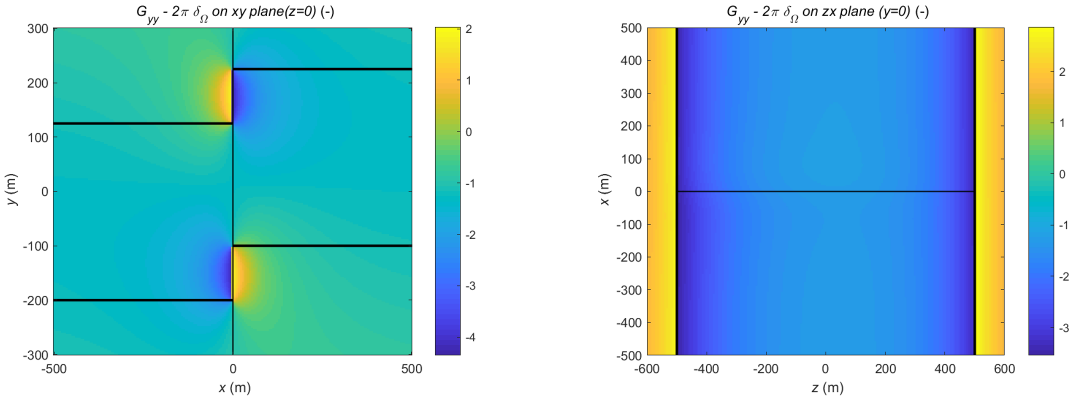

(e) Dimensionless normal stress $\frac{\sigma_{yy}}{C}$ on the xy plane (Asymmetrical)

(f) Dimensionless normal stress $\frac{\sigma_{yy}}{C}$ on the zx plane (Asymmetrical)

Figure 4.4: Dimensionless normal stresses $\frac{\sigma_{xx}}{C}$ *and* $\frac{\sigma_{yy}}{C}$ *at the planes corresponding to* $x = 0$, $y = 0$ *and* $z = 0$, *with the scaling parameter* $C = 2.36 \times 10^6 N/m^2$ *as defined in equation (3.25), for an asymmetrical laterally thinning reservoir with dimensions as listed in table (2.3).*

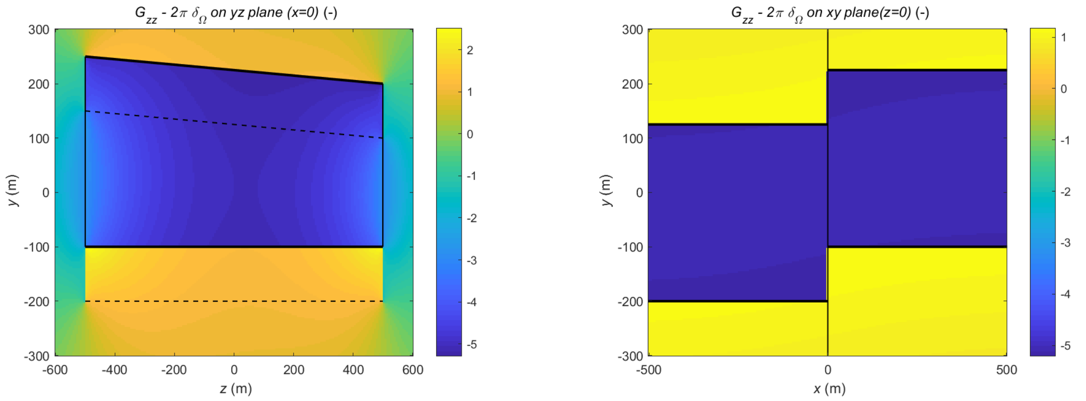

(a) Dimensionless normal stress $\frac{\sigma_{zz}}{C}$ on the yz plane (Asymmetrical)

(b) Dimensionless normal stress $\frac{\sigma_{zz}}{C}$ on the xy plane (Asymmetrical)

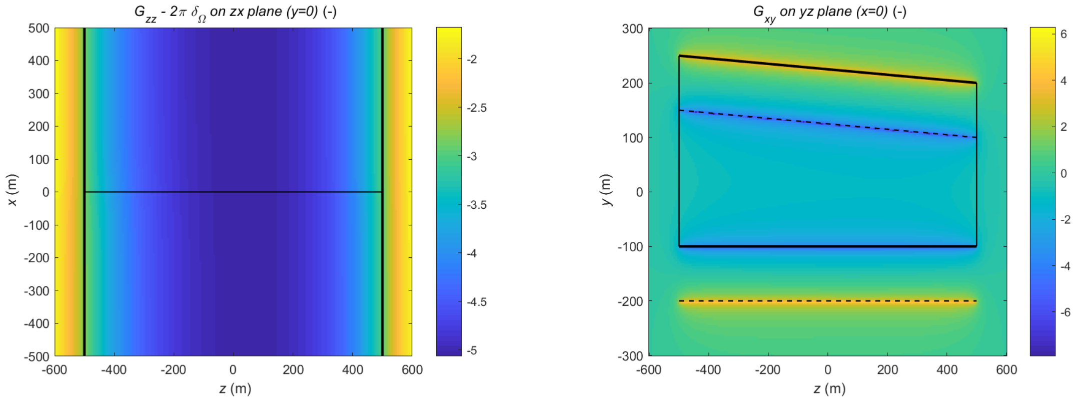

(c) Dimensionless normal stress $\frac{\sigma_{zz}}{C}$ on the zx plane (Asymmetrical)

(d) Dimensionless shear stress $\frac{\sigma_{xy}}{C}$ on the yz plane (Asymmetrical)

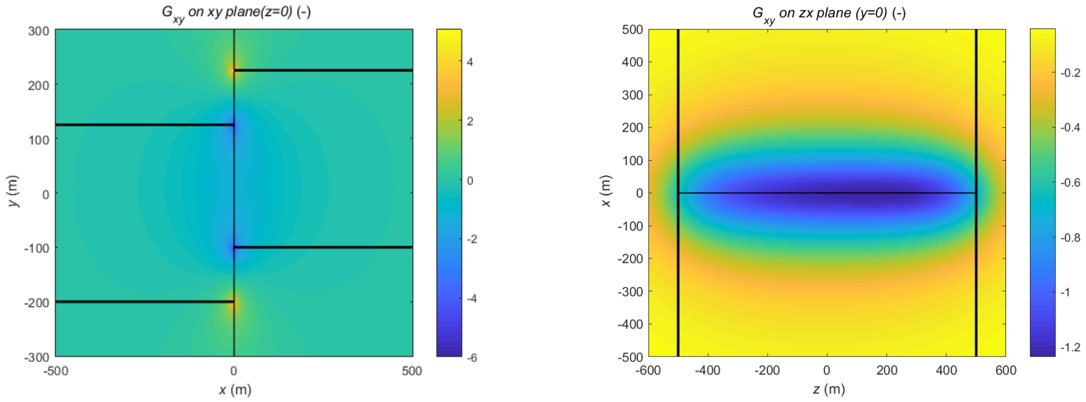

(e) Dimensionless shear stress $\frac{\sigma_{xy}}{C}$ on the xy plane (Asymmetrical)

(f) Dimensionless shear stress $\frac{\sigma_{xy}}{C}$ on the zx plane (Asymmetrical)

Figure 4.5: Dimensionless normal stress $\frac{\sigma_{zz}}{C}$ *and Dimensionless shear stress* $\frac{\sigma_{xy}}{C}$ *at the planes corresponding to* $x = 0$, $y = 0$ *and* $z = 0$, *with the scaling parameter* $C = 2.36 \times 10^6 N/m^2$ *as defined in equation (3.25), for an asymmetrical laterally thinning reservoir with dimensions as listed in table (2.3).*

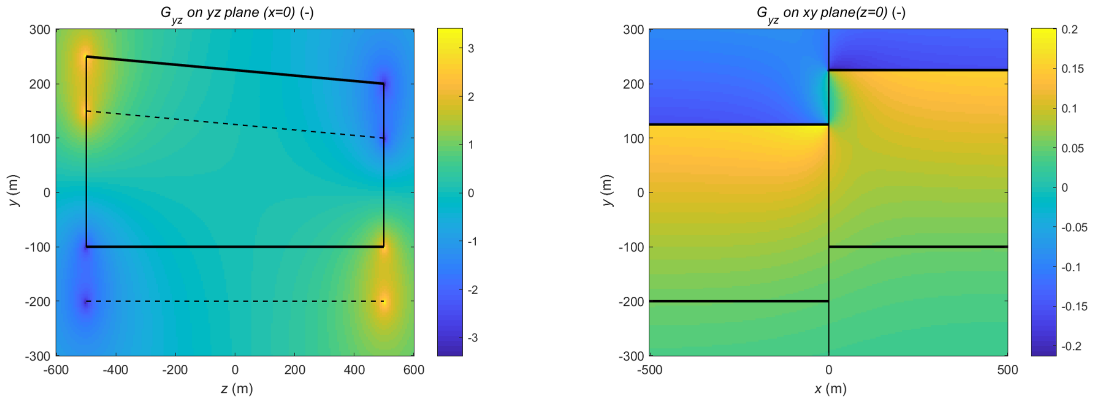

(a) Dimensionless shear stress $\frac{\sigma_{yz}}{C}$ on the yz plane (Asymmetrical)

(b) Dimensionless shear stress $\frac{\sigma_{yz}}{C}$ on the xy plane (Asymmetrical)

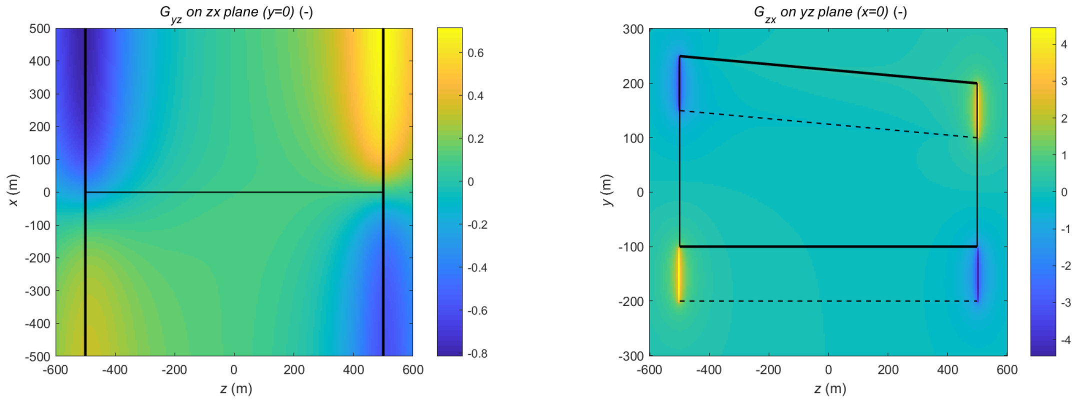

(c) Dimensionless shear stress $\frac{\sigma_{yz}}{C}$ on the zx plane (Asymmetrical)

(d) Dimensionless shear stress $\frac{\sigma_{zx}}{C}$ on the yz plane (Asymmetrical)

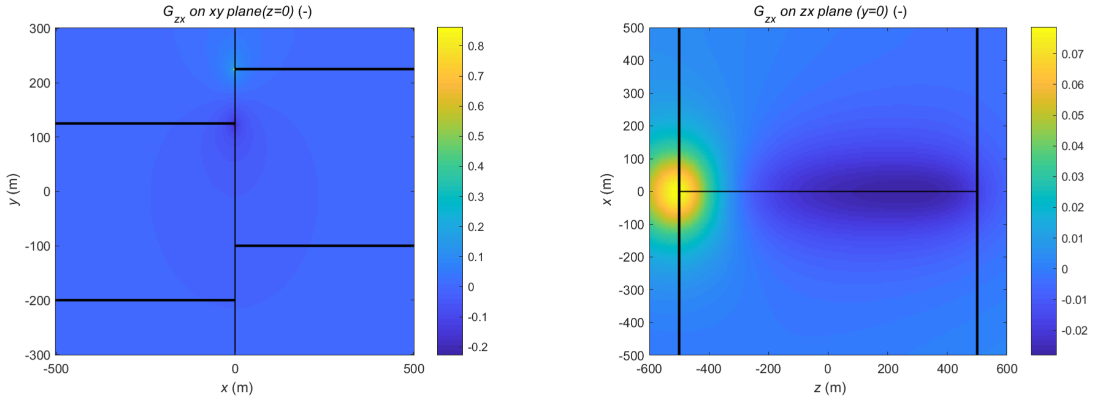

(e) Dimensionless shear stress $\frac{\sigma_{zx}}{C}$ on the xy plane (Asymmetrical)

(f) Dimensionless shear stress $\frac{\sigma_{zx}}{C}$ on the zx plane (Asymmetrical)

Figure 4.6: Dimensionless shear stresses $\frac{\sigma_{yz}}{C}$ *and* $\frac{\sigma_{zx}}{C}$ *at the planes corresponding to* $x = 0$*,* $they = 0$ *and* $z = 0$*, with the scaling parameter* $C = 2.36 \times 10^6 N/m^2$ *as defined in equation (3.25), for an asymmetrical laterally thinning reservoir with dimensions as listed in table (2.3).*

The induced stresses (dimensionless) for a symmetrical three-dimensional cuboidal reservoir as depicted in figures (4.1), (4.2) and (4.3) are consistent with the findings in two-dimensional plane-strain analysis as covered in Jansen et al. [10]. As can be seen in figures (4.1) and (4.2) the reservoir subjected to pore pressure increase (injection) undergoes compression (in the sign convention throughout this research, compressive stresses are negative). The overburden and underburden in the immediate vicinity of the fault also experience stress perturbations, but tensile in nature. The magnitude and distribution of these tensile stresses is relatively low, predictably owing to their infinitely heigh vertical extent as compared to the reservoir height. For visualisation of the boundary effects of the lateral reservoir boundaries in x direction, we plot the results depicting stresses over the entire reservoir for dimensionless normal stress σ_{xx} and shear stress σ_{xy} as depicted in figure (4.7). At the lateral end of the reservoir perpendicular the the fault strike direction, ($x = \pm 3000$ m), the formations adjacent to the reservoir also undergoes slight compression. There is a sharp boundary of compressive and tensile stresses of low magnitudes in both the overburden and the underburden at the ($x \pm 3000$ m) mark. End effect on the reservoir boundary can be seen within the reservoir largely upto ($\approx x \pm 2500$ m), where the compressive stresses on the reservoir decrease approaching the end of the reservoir.

The dimensionless horizontal stress perpendicular to the strike of the fault $\frac{\sigma_{xx}}{C}$, are continuous in the x direction within the reservoir. Similarly, normal stresses $\frac{\sigma_{yy}}{C}$ and $\frac{\sigma_{zz}}{C}$ are continuous in the y and z directions respectively. At the fault (yz) plane, as observed in figure (4.1 (a)), the compressive stresses $\frac{\sigma_{xx}}{C}$ are the highest at the section of the fault where the reservoir juxtaposes the reservoir followed by lower compressive induced at stress sections of the fault where reservoir juxtaposes the overburden and underburden. We compared this to the stress pattern observed for a reservoir with no displacement (throw, $t = 0$) as in figure (4.8 (a)). The induced stress in this case are uniform within the reservoir. As a result, for a fault with displacement the stresses are concentrated on a smaller section of the fault and the fault experiences differential weakening of the fault's shear strength. Vertical normal stress $\frac{\sigma_{yy}}{C}$ in figure (4.1 (e)) also depict a concentration of stresses in fault sections where reservoir juxtaposes overburden or underburden, with the reservoir under compression and the formation across the fault under tension.

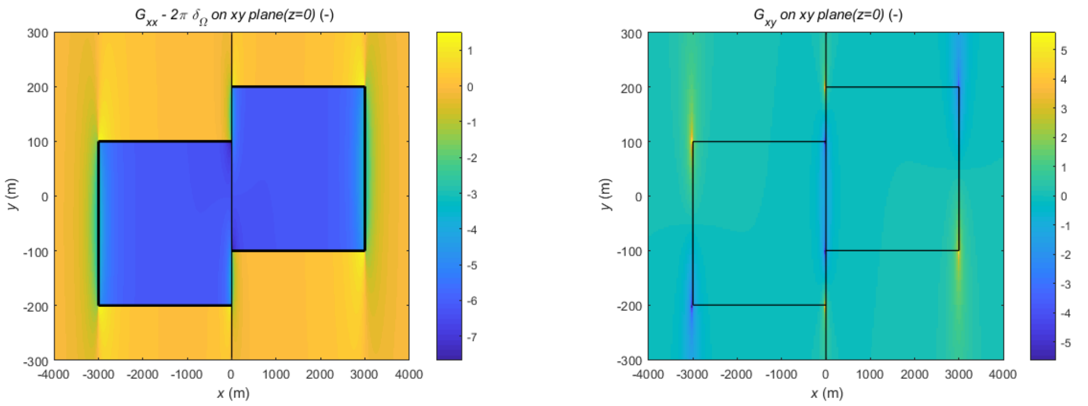

(a) Dimensionless normal stress $\frac{\sigma_{xx}}{C}$ on the xy plane (whole reservoir)

(b) Dimensionless normal stress $\frac{\sigma_{xy}}{C}$ on the xy plane (whole reservoir)

Figure 4.7: Dimensionless normal stress $\frac{\sigma_{xx}}{C}$ *and dimensionless shear stress* $\frac{\sigma_{xy}}{C}$ *at the* $z = 0$ (xy) *plane, with the scaling parameter* $C = 2.36 \times 10^6 N/m^2$ *for a symmetrical cuboidal reservoir with dimensions as listed in table (2.3), depicted for the whole reservoir including the horizontal booundaries* ($x \pm 3000$ *m*)

For shear stress $\frac{\sigma_{xy}}{C}$ figure (4.2 (f)) shows stress concentrations at the boundaries of reservoir units on either side of the fault. The induced stress exhibits a normal faulting tendency at the top of foot wall (right of the fault) and at the bottom of the hanging wall while the top of the hanging wall and the bottom of the foot wall undergo reverse faulting stresses for an increased reservoir pressure (injection). The same is expected to be reversed with decrease in pore pressure (production). As we see in figure (4.7 (b)), the edges of the reservoir witness induced shear stresses $\frac{\sigma_{xy}}{C}$ of the opposite sign as those on the fault, at the same vertical height with a reverse faulting tendency at the top of the foot wall and bottom of the hanging wall. For the reservoir with a fault with no throw, in figure (4.8 (b)), the observed shear stress is considerably lower, with no sections of the fault with stress concentrations. It is important to note that since we consider a location slightly to the right of the fault, in figures depicting results at the fault plane, $y = 100$ m represents the top of the hanging wall, $y = 200$ m represents the top of the foot wall, $y = -100$ m represents the bottom of the foot wall and $y = -200$ m represents the bottom of the hanging wall.

Asymmetrical laterally thinning reservoir The induced stresses for a laterally thinning reservoir, are qualitatively the same as observed for a cuboidal reservoir. We do not observe the anticipated effects of

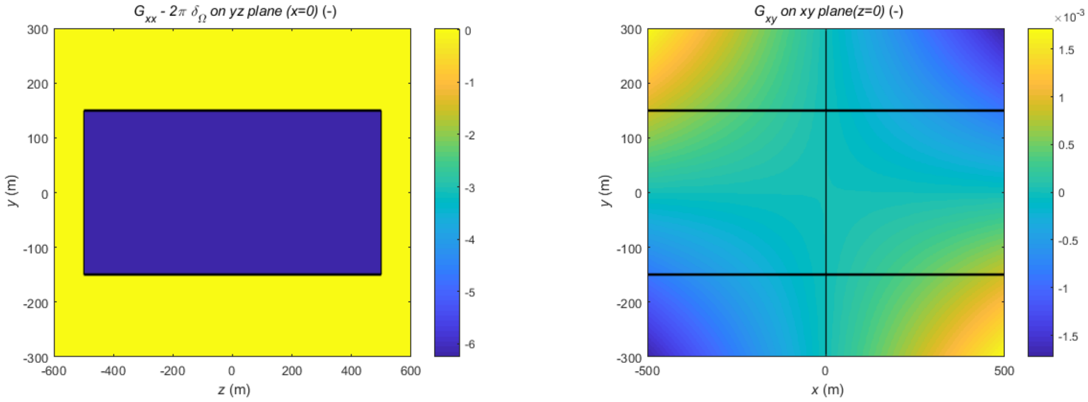

(a) Dimensionless normal stress $\frac{\sigma_{xx}}{C}$ on the xy plane (whole reservoir)

(b) Dimensionless shear stress $\frac{\sigma_{xy}}{C}$ on the xy plane (whole reservoir)

Figure 4.8: Dimensionless normal stress $\frac{\sigma_{xx}}{C}$ *and dimensionless shear stress* $\frac{\sigma_{xy}}{C}$ *at the* $z = 0$ (xy) *plane, with the scaling parameter* $C = 2.36 \times 10^6 N/m^2$ *for a symmetrical cuboidal reservoir with throw,* $t = 0$, $a = b = 150$ m *and all other dimensions as listed in table (2.3)*

the lateral thinning on the behaviour of induced stresses, normal or shear. The locations of concentration of stresses in this case are analogous to the stress concentrations in the cuboidal reservoir. Shear stress $\frac{\sigma_{xy}}{C}$ depict a normal faulting tendency at the top of the hanging wall and the bottom of the foot wall, with a reverse faulting tendency on the bottom of the hanging wall and the top of the foot wall.

4.2. Slip

Slip is the relative movement of rocks on either side of a fault or fracture plane. When strain energy accumulated over long durations in the rocks across the fault is released suddenly in the form of slip, seismic waves are generated that can be felt on the surface as earthquakes. Upon injection/production of fluids in the reservoir, pore pressure changes result in an altered the state of stress across a pre-existing fault and the resultant stresses can result in slip. To study the locations for initiation of slip, as well as to determine the incremental pore pressures p required to make the fault unstable or initiate slip, we use the Coulomb criterion for failure along a fault. The Coulomb criterion can be defined by the following equations

$$\begin{aligned} \sigma^0_{shear} + \sigma_{shear} &> -\mu(\sigma'^0_{normal} + \sigma'_{normal}) \quad \text{if} \quad \sigma^0_{shear} + \sigma_{shear} > 0, \\ \sigma^0_{shear} + \sigma_{shear} &< \ \ \mu(\sigma'^0_{normal} + \sigma'_{normal}) \quad \text{if} \quad \sigma^0_{shear} + \sigma_{shear} < 0. \end{aligned} \tag{4.5}$$

where σ^0_{shear} is initial shear stress, σ'^0_{normal} is initial effective normal stress, σ_{shear} is incremental shear stress, σ'_{normal} is incremental effective normal stress and μ is the friction coefficient. Effective stresses are related to the corresponding total stresses by the Terzaghi principle as described in equation (3.1). Note that since we assume that the fault allows pressure transmission laterally across the fault within the reservoir, we use a slightly modified form of equation (3.1):

$$\sigma^*_{ij} = \sigma^{*'}_{ij} - \alpha p \delta_{\Omega'} \delta_{ij}, \tag{4.6}$$

where Ω' refers to the reservoir and the section of the fault in contact with the reservoir, and $\delta_{\Omega'}$ is the modified Kroecker delta defined as

$$\delta_{\Omega} = \begin{cases} 1 & \text{if} \quad (x,y) \in \Omega' \\ 0 & \text{if} \quad (x,y) \notin \Omega' \end{cases}. \tag{4.7}$$

This is a slight refinement to the defintion of effective stress as in equation (24) from Jansen et al. [10], but in line with the usage in equation (28) from Jansen et al. [10] In section (4.1.1), we calculated total normal and shear stresses at the fault plane. In this section, we use the Coulomb criterion from equation (4.5) to predict the initiation of slip. In our analysis for slip on the fault plane, with the fault and reservoir along axis directions as depicted in figure (2.2), the normal stresses σ_{normal} correspond to the horizontal normal stresses in the $x-$direction, σ_{xx}, while the shear stresses σ_{shear} correspond to the resultant of orthogonal shear stresses σ_{xy} and σ_{zx}.

It is to be noted that we take the maximum potential for triggering slip to be at the fault plane ($x = 0$), in line with our findings in the plane-strain case covered in Jansen et al. [10] that the maximum incremental shear stress σ_{xy} corresponds to $x = 0$. We also assume the plane of slip initiation to be the fault plane, as an existing fault surface is more likely to be the weakest surface prone to slip upon alteration in stress conditions. In reality it is however still possible there could be creation of new fractures/faults upon pore pressure changes, that then act as the slipping surface. Further analysis can thus be done by considering the possibility of slip initiation in any other plane in the reservoir. In this report, however, we limit ourselves to the assumption stated. The total resultant shear stress $\sigma^{R,T}_{shear}$ is thus defined as follows

$$\sigma^{R,T}_{shear} = \sqrt{(\sigma^0_{xy} + \sigma_{xy})^2 + (\sigma^0_{zx} + \sigma_{zx})^2}, \tag{4.8}$$

with $\sigma^0_{xy} = 15 \times 10^6$ MPa and $\sigma^0_{zx} = 0$ MPa . The incremental resultant shear stress $\sigma^{R,inc}_{shear}$ is thus defined as

$$\sigma^{R,inc}_{shear} = \sigma^{R,T}_{shear} - \sigma^0_{shear}, \tag{4.9}$$

with

$$\sigma^0_{shear} = \sqrt{(\sigma^0_{xy})^2 + (\sigma^0_{zx})^2} = \sqrt{(\sigma^0_{xy})^2 + (0)^2} = \sigma^0_{xy}$$

In order to ascertain the reservoir end effect on the shear stresses and to find the location of highest shear stresses along the z-direction, the total resultant shear stresses are plotted at an incremental pressure $p = -20$ MPa, for different distances from $z = 0$, along with the slip boundary given by equation (4.5), as in figure (4.9). In the figure, the maximum shear stresses are at the closest distance from the $z = 0$ plane. Therefore for further analysis for slip at a constant z, we consider stresses at $z \approx 0$. As seen in figure (4.9), the stresses along the z direction are fairly independent of the $z-$ location except very close to the endpoints of the reservoir. Therefore, the end effects are limited to very close to the $z-$ boundary of the reservoir and

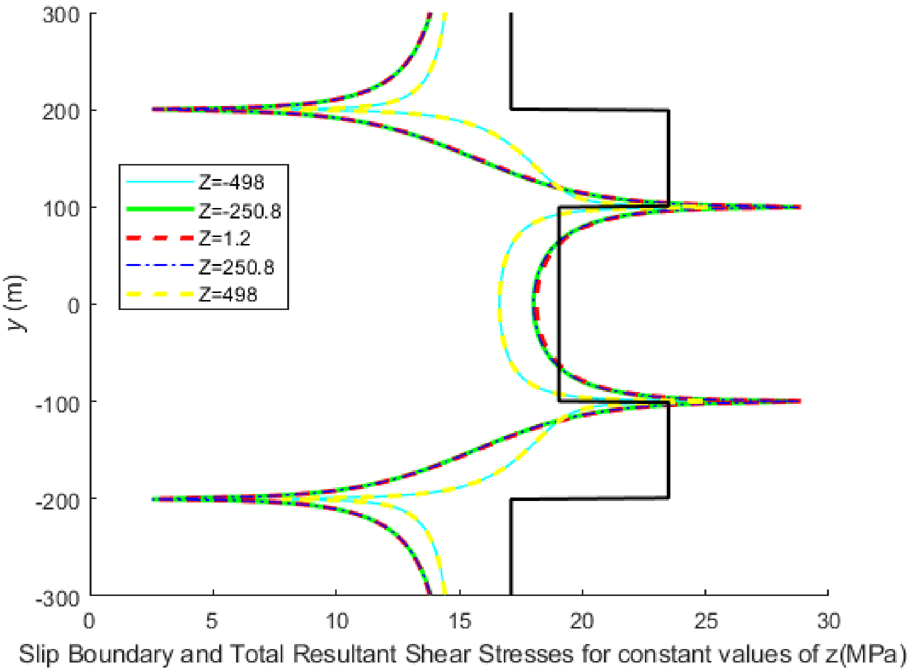

Figure 4.9: Total resultant shear stress at different z, for an incremental reservoir pressure, $p = -20$ MPa . The solid black line represents the slipping boundary

all the points within the domain and the reservoir at a particular vertical elevation would exhibit the same slipping behaviour, except near the boundaries. Accordingly, we plot the relevant stresses at the fault plane ($x = 0$), for a single constant value of $z (z \approx 0)$ so as to ascertain the variation of stresses along the vertical height of the reservoir.

Figure (4.10) depicts all the relevant stresses for the slip conditions, for an incremental pore pressure $p = -20$ MPa (Production). Subplot (a) depicts the initial effective normal stress σ'^0_{normal}, incremental normal stress σ_{normal}, incremental effective normal stress σ'_{normal} and total effective normal stress $\sigma'^0_{normal} + \sigma'_{normal}$. Subplot (b) depicts the initital shear stress σ^0_{shear}, incremental resultant shear stress $\sigma^{R,inc}_{shear}$ and total resultant shear stress $\sigma^{R,T}_{shear}$ as defined in equations (4.8) and (4.9). Subplot (c) depicts the total resultant shear stress $\sigma^{R,T}_{shear}$ with the slip thresholds or slip boundaries $\pm\mu(\sigma'^0_{normal} + \sigma'_{normal})$. Slip conditions are met when total resultant shear stress exceeds the slip threshold as defined by Coulomb criterion. Total resultant shear stress to the right of positive slip boundary results in normal slip, while total resultant shear stress to the left of negative slip boundary results in reverse slip. We note that in case of a vertical fault as considered in our example, we consider the reservoir unit to the left of fault plane ($x < 0$) to be the hanging wall and reservoir unit to the right of the fault plane ($x > 0$) to be the foot wall. As a result, normal slip implies that the reservoir unit to the right of the fault moves up relative to the unit on the left. Figure (4.11) depicts the same stresses as in figure (4.10), but for an incremental pore pressure $p = 20$ MPa (Injection).

From sublots (b) in figures (4.10) and (4.11), we observe the incremental shear stresses $\sigma^{R,inc}_{shear}$ for both the production and injection show distinctive patterns. For production, we observe a concentration of positive incremental shear stress(normal faulting tendency) in the region where reservoir juxtaposes reservoir across the fault and a slightly negative incremental shear stress in the region outside the reservoir or where overburden juxtaposes overburden and underburden juxtaposes underburden. In the section between these two regions, where reservoir juxtaposes overburden and underburden, the incremental shear stress transitions between the negative and positive peaks at the reservoir boundaries. There is a positive peak observed for incremental and total resultant shear stresses at the inner boundary of the region where reservoir juxtaposes overburden/underburden (in our case at $y = \pm 100$ m) and a negative peak at the outer boundary of the reservoir ($y = \pm 200$ m). At the chosen incremental pore pressure of $p = -20$ MPa, the slip conditions are met at point very close to the $y = \pm 100$ m boundary, while most points outside the region bounded by $y = \pm 100$

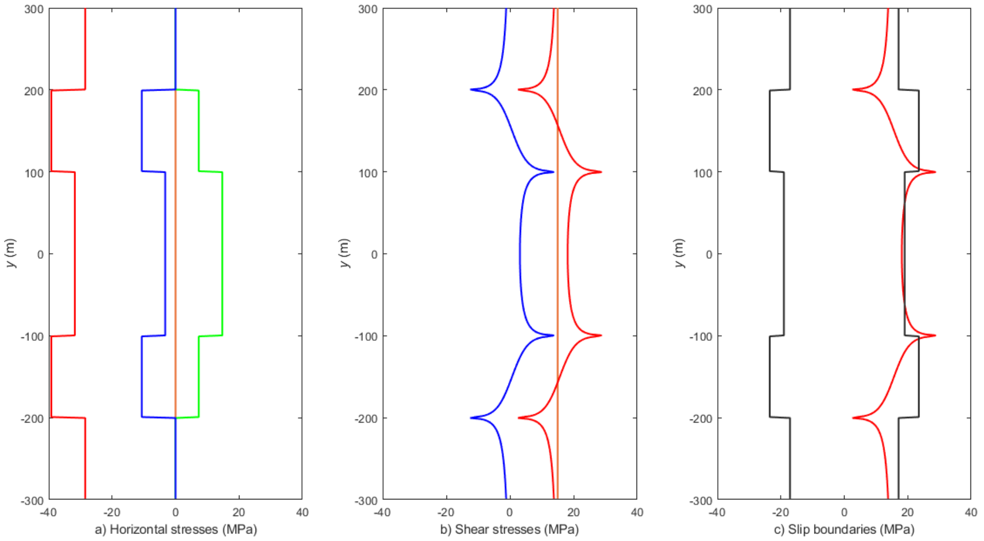

Figure 4.10: Stresses at $z \approx 0$ *for an reservoir pressure,* $p = -20$ *MPa .*
a) Horizontal stresses; orange: σ'^{0}_{normal}*, green:* σ_{normal}*, blue:* σ'_{normal}*, red:* $\sigma'^{0}_{normal} + \sigma'_{normal}$*.*
b) Shear stresses; orange: σ^{0}_{shear}*, blue:* $\sigma^{R,inc}_{shear}$*, red:*$\sigma^{R,T}_{shear}$*.*
c) Regions of slip; red: $\sigma^{R,T}_{shear}$*, gray: slip boundaries* $\pm\mu\ (\sigma'^{0}_{normal} + \sigma'_{normal})$ *;*

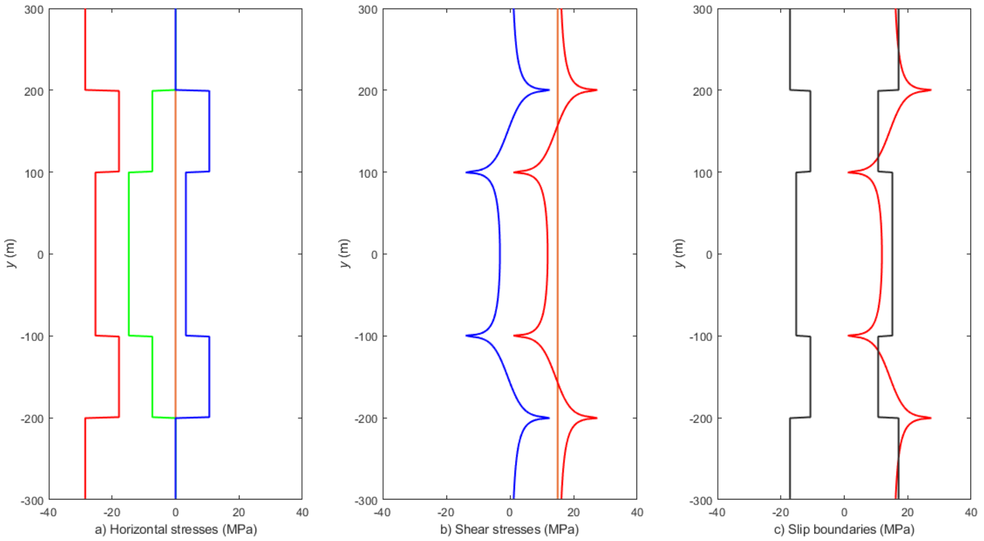

Figure 4.11: Stresses at $z \approx 0$ *for an reservoir pressure,* $p = 20$ *MPa .*
a) Horizontal stresses; orange: σ'^{0}_{normal}*, green:* σ_{normal}*, blue:* σ'_{normal}*, red:* $\sigma'^{0}_{normal} + \sigma'_{normal}$*.*
b) Shear stresses; orange: σ^{0}_{shear}*, blue:* $\sigma^{R,inc}_{shear}$*, red:*$\sigma^{R,T}_{shear}$*.*
c) Regions of slip; red: $\sigma^{R,T}_{shear}$*, gray: slip boundaries* $\pm\mu\ (\sigma'^{0}_{normal} + \sigma'_{normal})$ *;*

m have shear stresses well below the slip boundary on the right. The shear stresses within these boundaries however, are very close to the slip boundary and predictably result in slip as pressure is depleted slightly more. It is important to note, the total resultant shear stress $\sigma^{R,T}_{shear}$ in our analysis, is positive for the whole length of the fault due to high initial shear stress assumption in our model. In the case where initial shear stress is negligible, the negative peaks observed in the incremental shear stress would imply a negative peak in total resultant shear stress and thus a reverse faulting tendency in corresponding section of the reservoir at the same time another section exhibits a positive faulting tendency.

In the case of injection, expectedly, the peaks are reversed with positive peaks at $y = \pm 200$ m and negative peaks at $y = \pm 100$ m. The stress concentrations are also accordingly of opposite signs, with the region where reservoir juxtaposes reservoir experiencing a negative incremental shear stress $\sigma^{R,inc}_{shear}$ (reverse faulting tendency) and the region beyond the reservoir with slightly positive incremental shear stress. However it is interesting to note, points in the region bounded by $y = \pm 100$ m have total resultant shear stresses well below the slip boundary, but points outside the $y = \pm 100$ m boundary and within the reservoir limits i.e within the $y = \pm 200$ m bounds, have shear stresses higher than the slip boundaries while the regions beyond the $y = \pm 200$ m marks are very close to the slip boundary, still within the non-slip zone. As a result, for injection, the section of the fault where reservoir juxtaposes overburden or the underburden is more liekly to slip at lower incremental pore pressures. The results obtained, are qualitatively and quantitatively in line with what we observed for the analysis for plane-strain case in Jansen et al. [10]. As mentioned in section (4) the peaks in shear stress G_{xy} at reservoir boundaries at exactly $y = \pm 100$ m and $y = \pm 200$ m are infinitely high for both production and injection, but the peaks have been limited while plotting. The infinite peaks in G_{xy} (and thus the incremental and total resultant shear stresses) at reservoir boundaries imply the total resultant shear stress at these boundaries cross the slip threshold for the slightest of pressure change and thus any change in pore pressure p would lead to some amount of slip at these boundaries, in line with our findings for the plane-strain analysis.

To visualize the slip behaviour at different pore pressures, we plot the corresponding slip boundaries and shear stresses at different incremental pore pressures for both production and injection cases, as depicted in figure (4.12). The initial conditions at zero incremental pore pressure depict shear stresses below the slip thresholds. We observe peaks at low levels of depletion/injection at the same locations as discussed above, and with increasing depletion/injection the slip boundaries shift further, but the area with shear stresses beyond the slip boundary still increases. As evident from figure (4.12 (a)) for the production case, at relatively lower levels of depletion ($p = -5$ MPa), the shear stresses exceed the slip threshold only near $y = \pm 100$ m boundary. As the pore pressure decreases (further depletion, ($p = -20$ MPa)) a wider area within the $y = \pm 100$ m boundaries now has shear stresses above the slip threshold, with peaks at the same locations as before. This is analogous to a slip patch growth as the depletion continued. It is interesting to note that in this case, in the region bounded by $y = \pm 100$ m with shear stress still below the slip threshold (region between $y = \pm 75$ m), the shear stress is now much closer to the slip threshold than at lower levels of depletion, and thus more likely to slip. We quantify this relative likeliness of a section of the fault to deform/slip using the concept of shear capacity utilization, as explained below. As the depletion levels increase further, we observe that the slip patch grows further within the $y = \pm 100$ m boundary, with most of the region now beyond the slip threshold. However, in the region beyond the $y = \pm 100$ m boundary, shear stresses stay below the slip threshold even at higher levels of depletion. In fact, beyond the $y = \pm 200$ m mark, the shear stress is seen to decrease as pore pressure increases, thus leading to stabilisation. A similar aspect is observed in the case for injection, in figure (4.12 (b)) . As the pore pressure increases, section of the fault with shear stress more than slip threshold increases beyond the $y = \pm 200$ m slip boundary. While in the region between the $y = \pm 100$ m, the resultant shear stress is lower at higher levels of injection. This could imply that after a section of the fault undergoes slip and possibly triggers growth of the slip patch without any further change in pore pressure due to reduction in friction (discussed below), the possible propagation of the slip patch could be thwarted by sections of the fault with shear stresses significantly lower than the slip threshold. This could possible mean that concentration of induces stresses at reservoir boundaries, despite causing slip at lower levels of incremental pore pressures, could possibly contain the slip patch growth. It is important to note that since our analysis models only the induced stresses and initiation of slip, the predictions about slip patch growth would need a dynamic modelling of slip to be confirmed.

We also note while determining slip boundaries the coefficient of friction used is the coefficient of static friction, μ_{static}. The coefficient of static friction corresponds to a peak value for friction along the fault and the shear stress is required to exceed this limiting value to initiate slip. Once the slip is initiated, however, the frictional strength of the fault typically reduces to a residual value, corresponding to the typically lower coefficient of dynamic friction, $\mu_{dynamic}$ [11]. The dynamic friction depends on the sliding history of the fault as well as the slip velocity among other factors. Since we limit our analysis to the initiation of slip, and do not model the dynamic evolution of slip in this report, we use the coefficient of static friction. It implies that in our analysis, once the peaks identified in shear stress cross the slip threshold, further slip patch growth would only be predicted with further induced stressing, or further depletion/injection. However, in actual scenarios,

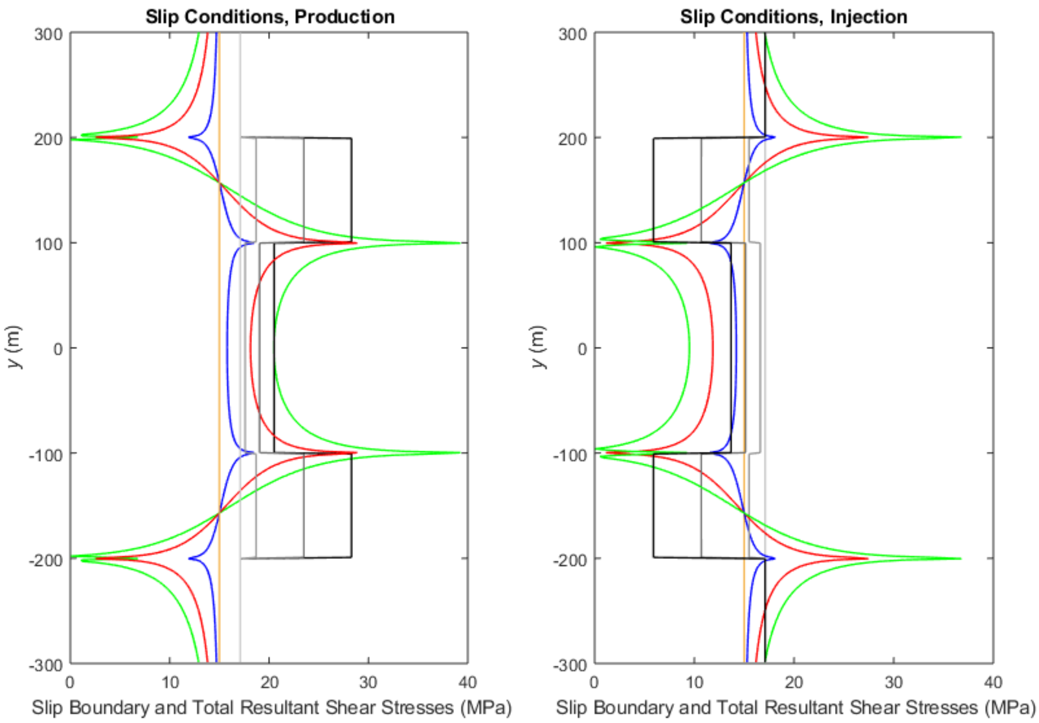

Figure 4.12: Shear stresses in a symmetrical cuboidal reservoir, resulting from different incremental reservoir pressures p*.*
a) production; orange: $p = 0$ MPa*, blue:* $p = -5$ MPa*, red:* $p = -20$ MPa*, green:* $p = -35$ MPa.
b) injection; orange: $p = 0$ MPa*, blue:* $p = 5$ MPa*, red:* $p = 20$ MPa*, green:* $p = 35$ MPa.
Gray lines in both figures: boundaries; light gray: $p = 0$ MPa*, medium gray:* $p = \pm 5$ MPa*, dark gray:* $p = \pm 20$ MPa *and black:* $p = \pm 35$ MPa.

the dynamic behaviour of friction and lower coefficients of dynamic friction would imply once the slip is initiated at the reservoir boundaries with infinite peaks, the estimated slip boundaries in figures (4.10) and (4.11) would shift to lower values. As a result,the slip patch might grow beyond the peaks observed without any further induced stresses, both in the case of production and injection. In case of production, the region lying between $y = \pm 100$ m would predictably undergo slip, while for injection the region beyond the $y = \pm 200$ m boundary would undergo slip. As a result, initiation of slip would most likely be followed by friction reduction and propagation of slip. Since we witness that for a critically stressed fault, even small perturbations in pore pressure result in peak shear stresses at structural discontinuities, it implies that even a small perturbation in pore pressure can not just initiate slip (as predicted by our analysis), but can possibly lead to propagation of slip or slip patch growth without any further depletion. We note that the onset of slip is dependent on the calculated values for slip thresholds, which in turn are based on the initial in-situ stress conditions. Since sections of the fault are very close to the slip boundaries after a certain level of production/depletion, different values for initial stress values will shift the slip thresholds and change the critical pressures required for onset of slip. Thus the onset of slip across a fault due to production or injection is largely dependent on the initial state of stress in the subsurface.

In order to determine the progression of shear stresses and slip patch growth on the fault plane, we use a parameter shear capacity utilization (SCU), defined as:

$$SCU = \begin{cases} \frac{\sigma^{R,T}_{shear}}{-\mu(\sigma'^{0}_{normal} + \sigma'_{normal})} & \text{if} \quad \sigma^{R,T}_{shear} > 0,, \\ \\ \frac{\mu(\sigma'^{0}_{normal} + \sigma'_{normal})}{\sigma^{R,T}_{shear}} & \text{if} \quad \sigma^{R,T}_{shear} < 0. \end{cases} \tag{4.10}$$

As is evident from equation (4.10) and the Coulomb criterion in equation (4.5), stress conditions at a point result in slip when $SCU \geq 1$. The shear capacity utilization parameter fora symmetrical cuboidal reservoir with increasing and decreasing incremental pore pressures (for injection and production) respectively has been plotted in figures (4.13) and (4.14). Subplots (a) in both figures depict the initial conditions with incremental pore pressure $p = 0$ MPa. The region in red represents the area with $SCU \geq 1$. In case of production, increasingly negative (depleting) pore pressures result in a slip patch growth inwards from the $y = \pm 100m$ boundary initially. In figure (4.14(g)), the slip patches have not yet merged at incremental pore pressure of $p = -25$ MPa, but in figure (4.14(h)), the slip patches have already merged at $p = 35$ MPa. In order to examine the growth of slip patches inwards until they merge, we plot the SCU at smaller gaps in incremental pore pressure between $p = -25$ MPa and $p = -35$ MPa in figure (4.15). The slip patches merge in the middle of the reservoir at $p \approx -31$ MPa for the given example, and then the merged slip patch grows rapidly laterally outwards. This is different as observed in the injection scenario, with increasing pore pressures resulting in a slip patch growth inwards towards the $y = \pm 100m$ boundary initially, and then outwards towards the overburden and the underburden. The slip patches do not merge in this case. Recall that at the reservoir boundaries the total resultant shear stresses are infinitely high, and thus the $SCU > 1$ as soon as incremental pore pressure undergoes the slightest of change, but our figures erroneously depict no slip patch at these boundaries as we calculate and plot the results for a point slightly above or below these boundaries in order to avoid infinitely high values in the plots.

Another key difference between injection and production scenarios is the initiation of slip patch growth beyond the singularities at reservoir boundaries, at a lower differential pressure in the case of injection, as opposed to production. In our example, figure (4.13 (c)), shear stresses within a significant portion of the reservoir ($(-200 \text{ m} < y < -160 \text{ m})$ and $(160 \text{ m} < y < 200 \text{ m})$) have crossed the slip threshold and a slip patch grows beyond the boundary at an increased pressure of $p = 5$ MPa. In the case of production, however, in figure ((4.14 (c)) the shear stresses at each point except at the reservoir boundaries are still below the slip threshold and there is no observed slip patch, at a depletion level or $p = -5$ MPa. The thickness of the sections with $SCU \geq 1$ reaches the ≈ 40 m line (same as the thickness of slip patch for injection at $p = 5$ MPa) at an incremental pore pressure of $p = -15$ MPa. This accounts for difference of ≈ 10 MPa between the pressures required to allow similar sized sections of the fault to undergo slip for production and injection scenarios. Another notable insight from the SCU plots in the case of production, is that once the slip patches merge, the region of slip grows laterally outwards from the reservoir, as opposed to vertically outwards into the overburden and the underburden. Figures (4.16) (4.17) depict the shear capacity utilization parameter for increasing or decreasing incremental pore pressures respectively in an asymmetrical laterally thinning reservoir. The results obtained are similar to the results for a symmetrical cuboidal reservoir, with the growth of slip patch at similar incremental pore pressures and similar directions as described above for a cuboidal reservoir. However, one notable difference observes is that in case of production, the slip patches do not merge even at the depletion level of incremental pore pressure $p = -35$ MPa, while the slip patches merged at $p \approx -31$ MPa for the symmetrical cuboidal reservoir. It is important to note that the growth of the slip patch in our analysis is based on indicative calculations. Predicting the actual growth of slip patch would require dynamic modelling of slip propagation.

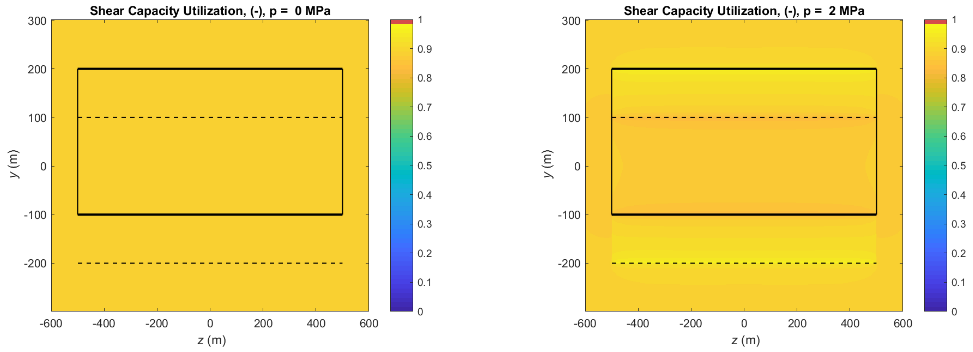

(a) SCU, $p = 0$ MPa (Symmetrical)

(b) SCU, $p = 2$ MPa (Symmetrical)

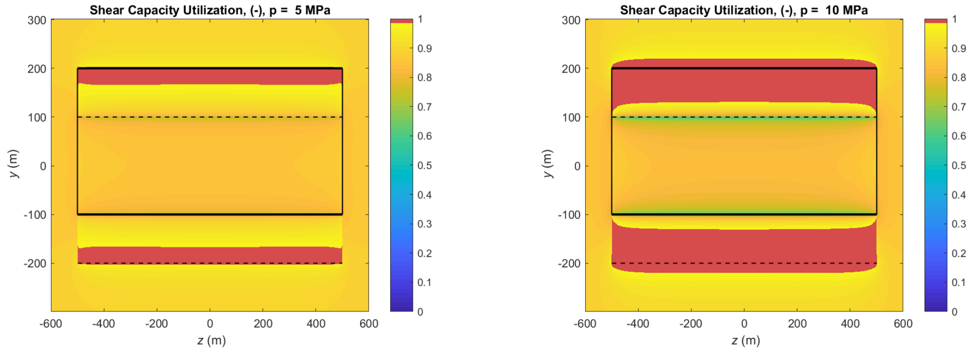

(c) SCU, $p = 5$ MPa (Symmetrical)

(d) SCU, $p = 10$ MPa (Symmetrical)

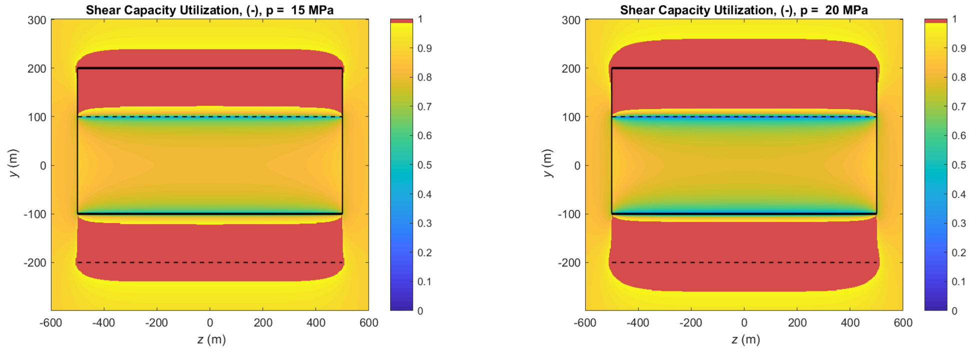

(e) SCU, $p = 15$ MPa (Symmetrical)

(f) SCU, $p = 20$ MPa (Symmetrical)

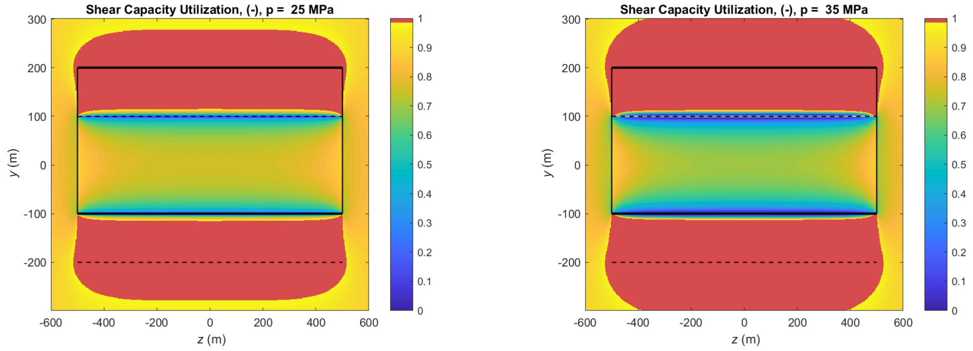

(g) SCU, $p = 25$ MPa (Symmetrical)

(h) SCU, $p = 35$ MPa (Symmetrical)

Figure 4.13: Shear Capacity Utilization (SCU) for different incremental pore pressures (Injection), for a symmetrical cuboidal reservoir with dimensions as listed in table (2.3). The red portions represents regions where resultant total shear stresses are beyond the slip conditions, and thus represent the slip patch.

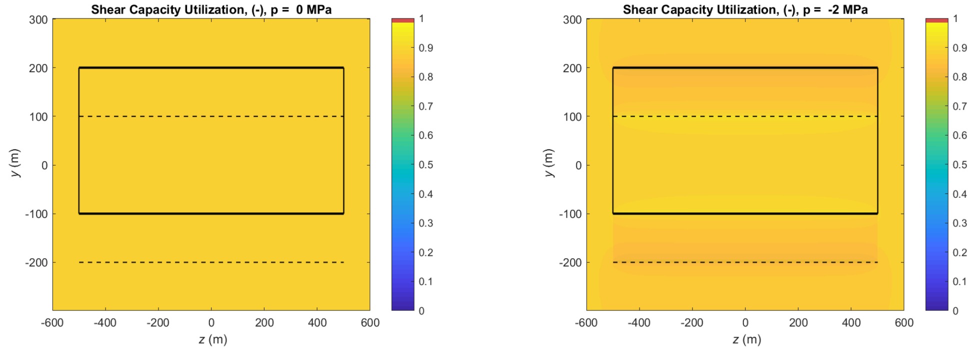

(a) SCU, $p = 0$ MPa (Symmetrical)

(b) SCU, $p = -2$ MPa (Symmetrical)

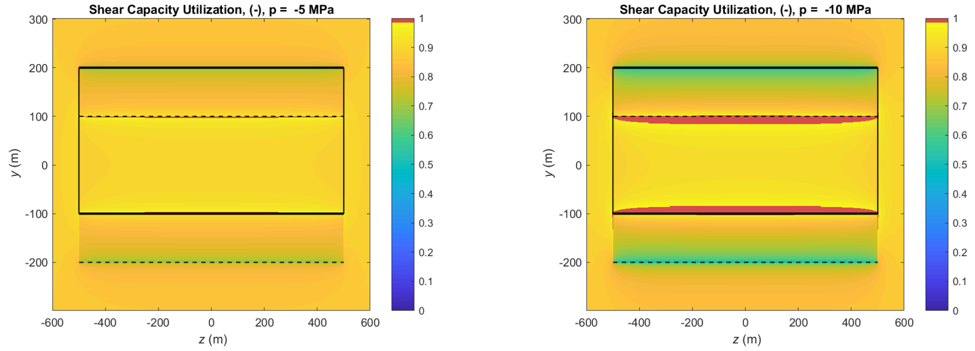

(c) SCU, $p = -5$ MPa (Symmetrical)

(d) SCU, $p = -10$ MPa (Symmetrical)

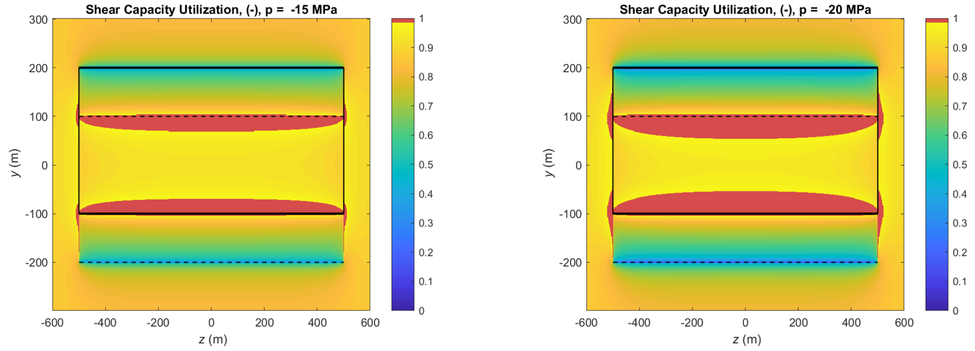

(e) SCU, $p = -15$ MPa (Symmetrical)

(f) SCU, $p = -20$ MPa (Symmetrical)

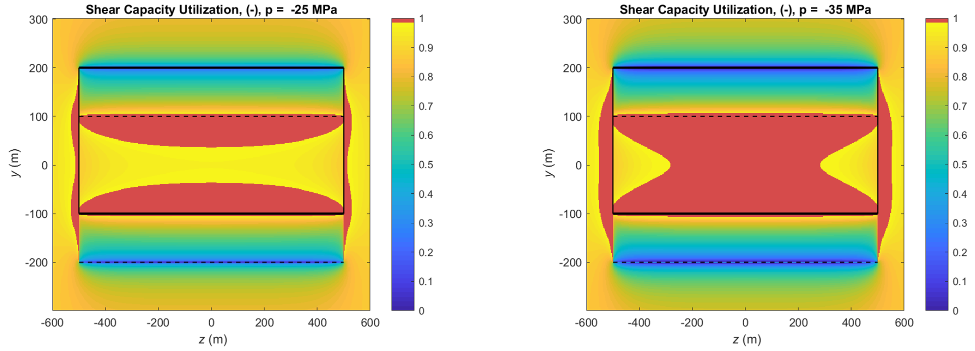

(g) SCU, $p = -25$ MPa (Symmetrical)

(h) SCU, $p = -35$ MPa (Symmetrical)

Figure 4.14: Shear Capacity Utilization (SCU) for different incremental pore pressures (Production), for a symmetrical cuboidal reservoir with dimensions as listed in table (2.3). The red portions represents regions where resultant total shear stresses are beyond the slip conditions, and thus represent the slip patch.

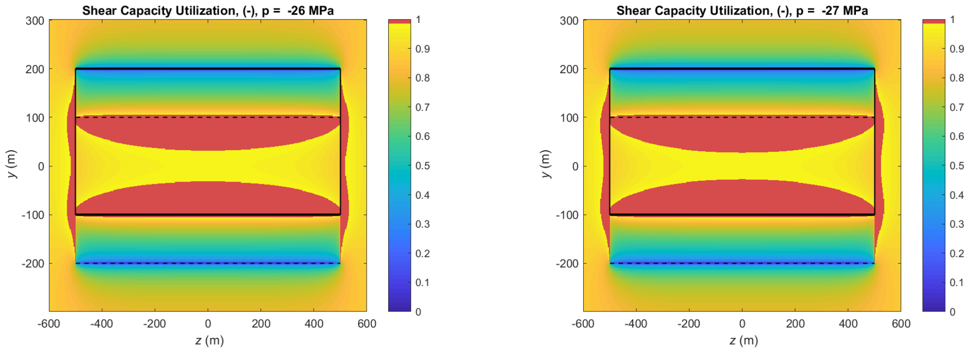

(a) SCU, $p = -26$ MPa (Symmetrical) (b) SCU, $p = -27$ MPa (Symmetrical)

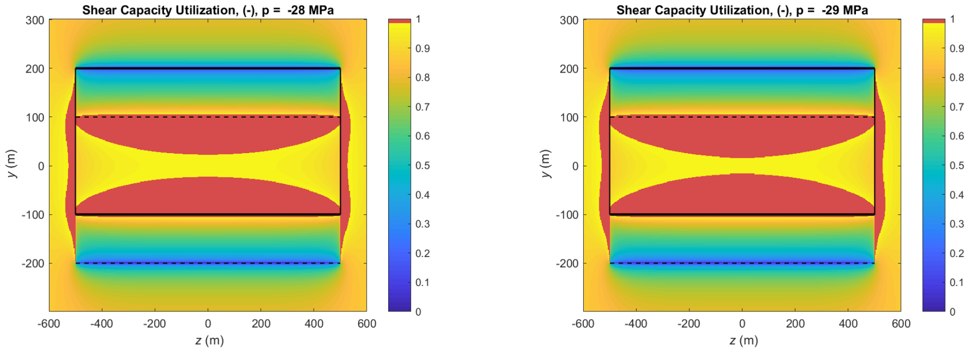

(c) SCU, $p = -28$ MPa (Symmetrical) (d) SCU, $p = -29$ MPa (Symmetrical)

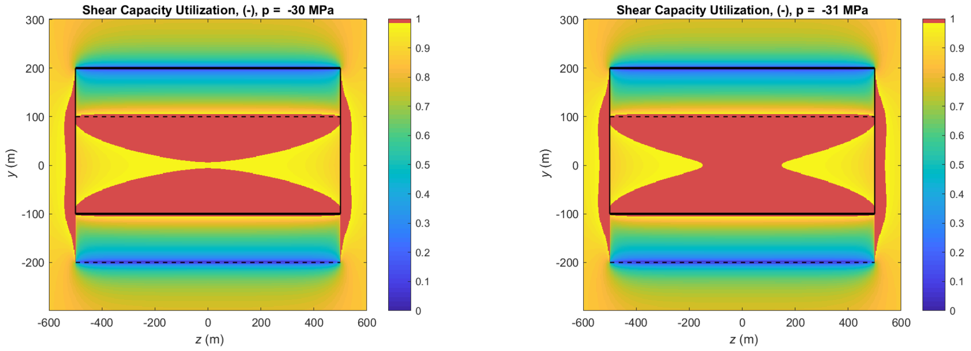

(e) SCU, $p = -30$ MPa (Symmetrical) (f) SCU, $p = -31$ MPa (Symmetrical)

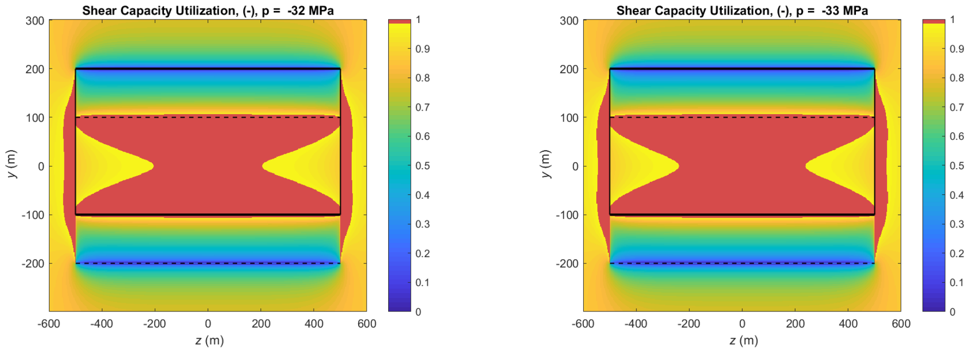

(g) SCU, $p = -32$ MPa (Symmetrical) (h) SCU, $p = -33$ MPa (Symmetrical)

Figure 4.15: Shear Capacity Utilization (SCU) for different incremental pore pressures (Production) depicting the merging of slip patches, for a symmetrical cuboidal reservoir with dimensions as listed in table (2.3). The red portions represents regions where resultant total shear stresses are beyond the slip conditions, and thus represent the slip patch.

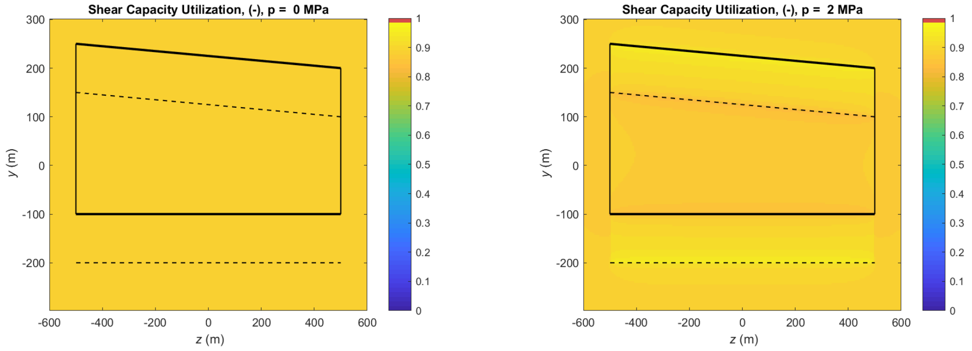

(a) SCU, $p = 0$ MPa (Asymmetrical)

(b) SCU, $p = 2$ MPa (Asymmetrical)

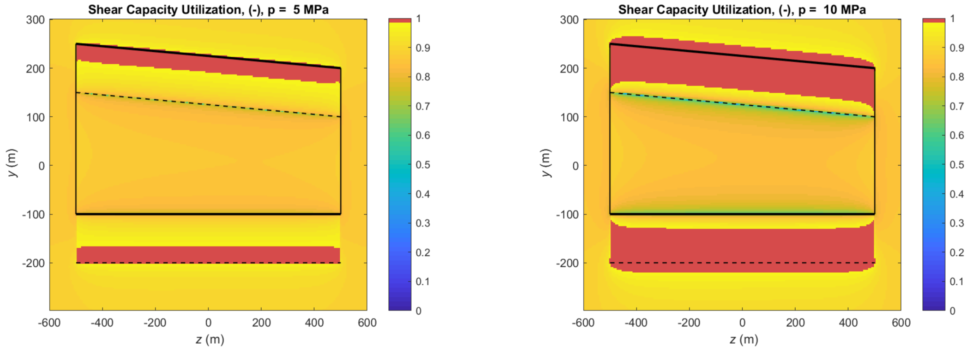

(c) SCU, $p = 5$ MPa (Asymmetrical)

(d) SCU, $p = 10$ MPa (Asymmetrical)

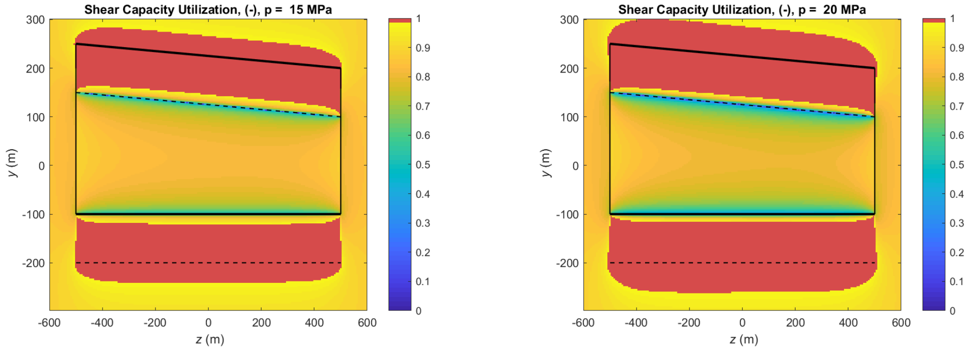

(e) SCU, $p = 15$ MPa (Asymmetrical)

(f) SCU, $p = 20$ MPa (Asymmetrical)

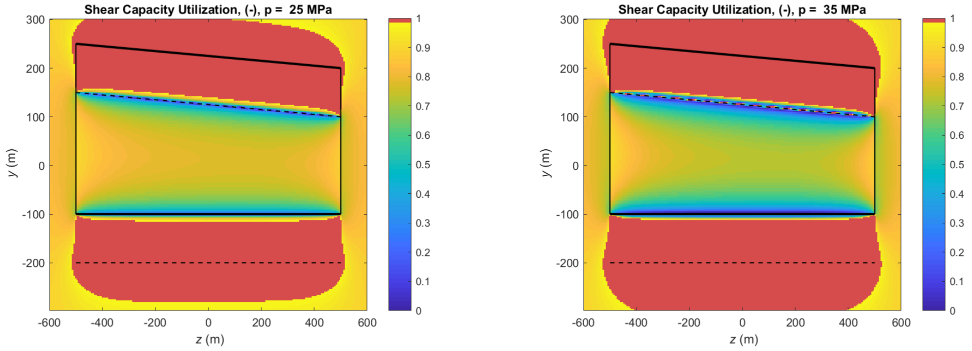

(g) SCU, $p = 25$ MPa (Asymmetrical)

(h) SCU, $p = 35$ MPa (Asymmetrical)

Figure 4.16: Shear Capacity Utilization (SCU) for different incremental pore pressures (Injection), for an asymmetrical thinning reservoir with dimensions as listed in table (2.3). The red portions represents regions where resultant total shear stresses are beyond the slip conditions, and thus represent the slip patch.

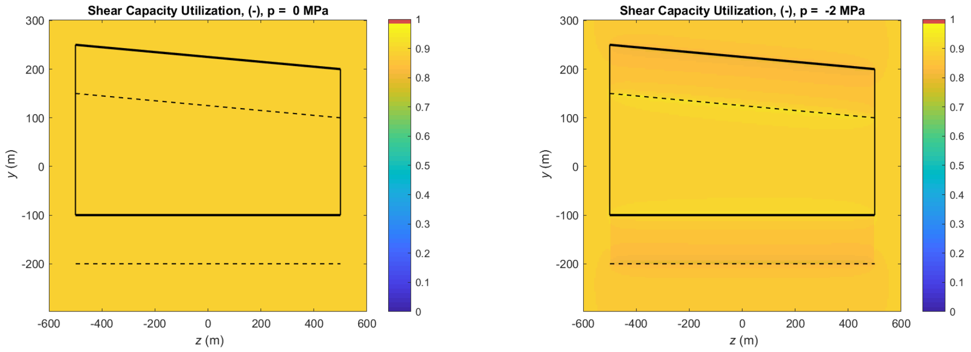

(a) SCU, $p = 0$ MPa (Asymmetrical) (b) SCU, $p = -2$ MPa (Asymmetrical)

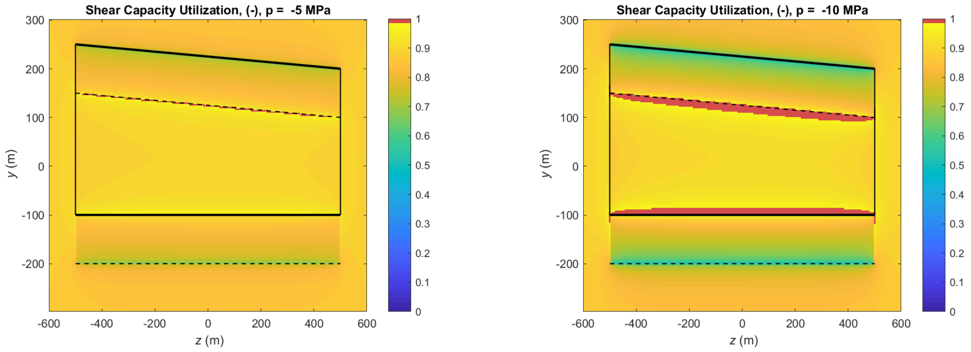

(c) SCU, $p = -5$ MPa (Asymmetrical) (d) SCU, $p = -10$ MPa (Asymmetrical)

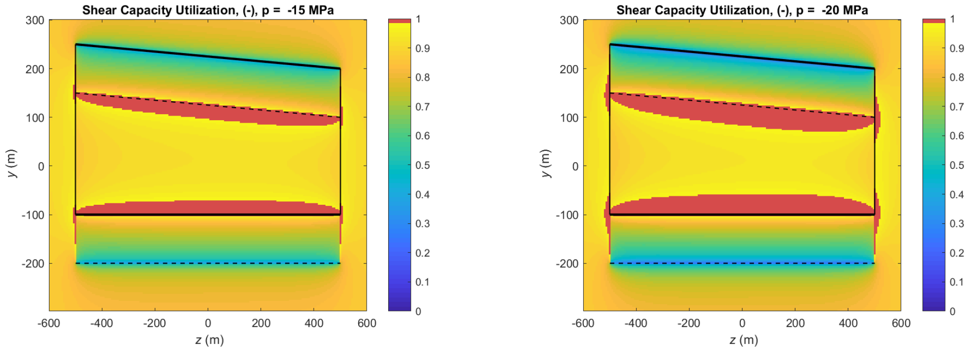

(e) SCU, $p = -15$ MPa (Asymmetrical) (f) SCU, $p = -20$ MPa (Asymmetrical)

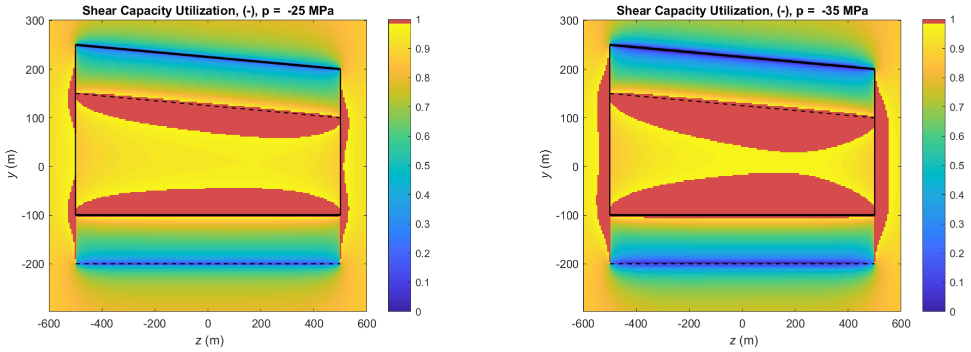

(g) SCU, $p = -25$ MPa (Asymmetrical) (h) SCU, $p = -35$ MPa (Asymmetrical)

Figure 4.17: Shear Capacity Utilization (SCU) for different incremental pore pressures (Production), for an asymmetrical thinning reservoir with dimensions as listed in table (2.3). The red portions represents regions where resultant total shear stresses are beyond the slip conditions, and thus represent the slip patch.

4.3. Shear stress directions

In the above sections, we have studied the slip conditions and shear stresses resultant due to a change in pore pressure p inside the reservoir. We consider the fault plane ($x = 0$) to be the plane where slip initiation takes place and the magnitudes of total resultant shear stresses, $\sigma^{R,T}_{shear}$ as defined in equation (4.8) are used to determine the slip initiation locations and pressures. However, it is important to note the direction of the total resultant shear stresses, $\sigma^{R,T}_{shear}$, would be varying within the plane, according to the changes in the directions of initial shear stress σ^{0}_{xy} as well as incremental shear stresses σ_{xy} and σ_{zx}. We plot vector plots depicting the resultant vector for $\sigma^{R,T}_{shear}$ with arrows, with the direction of the arrows representing the direction of the vector, while the size of the arrows represents the magnitude. The vector plots are depicted in figure (4.18). The magnitude of the resultant shear stresses, is, as we observed in the figures (4.10), along the y- axis, with peaks observed at $y = \pm 100m$ and $y = \pm 200m$ boundaries, however we see a change in directions somewhere between the boundaries. The change in orientation is quite evident in the region surrounding the reservoir, in the overburden and the overburden. Overall, qualitatively, the result for both the symmetrical and asymmetrical reservoirs are similar and the added complexity of lateral variation in reservoir thickness does not seem to impart much difference in the behaviour of resultant stresses and thus the resultant slip behaviour.

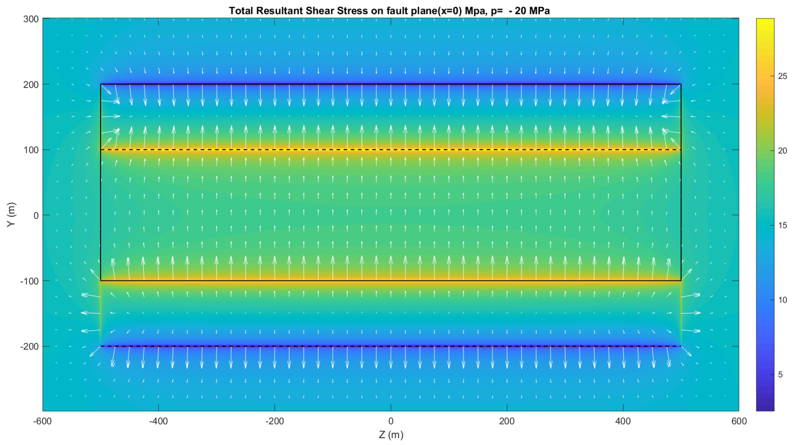

(a) Vector plot for total resultant shear stress (Symmetrical)

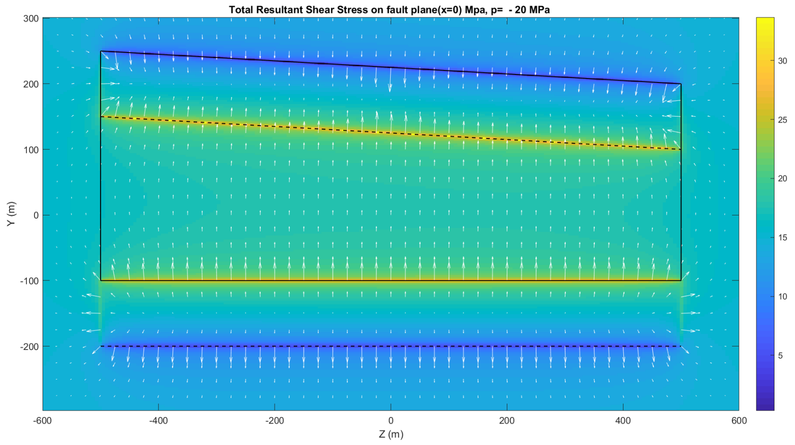

(b) Vector plot for total resultant shear stress (Asymmetrical)

Figure 4.18: Vector plot for total resultant shear stresses $\sigma^{R,T}_{shear}$, for a symmetrical cuboidal reservoir and for an asymmetrical laterally thinning reservoir, at a incremental pore pressure $p = -20$ MPa (Production). The arrows depict the vector direction, while the size of the arrows depicts the magnitude of the vector.

4.4. Sensitivity

We check the sensitivity of the resultant stresses and the initiation of slip to the fault throw chosen arbitrarily in our analysis, to check the validity of our example solution as well as to understand the impact of fault throw on the actual stress development.

We first check for induced stresses with varying reservoir thickness H. We use the scaled throw (t/H) to curtail the effects of throw on the stresses. The results are depicted in figure (4.19). We observe that the likelihood for the fault to initiate slip does not vary with reservoir height for a fixed ratio of fault throw to reservoir height. Figure (4.20) depicts the total resultant shear stresses, $\sigma^{R,T}_{shear}$ (solid lines), and the corresponding slip boundaries (dashed lines) for different fault throws, t, for a given reservoir height, $H = 300$ m. Subplot (a) is for pore pressure $p = -5$ MPa, while subplot (b) is for pore pressure $p = -20$ MPa. The reservoir dimensions a, b as depicted in schematic (2.2) are given by equations

$$a = \frac{H-t}{2}, \tag{4.11}$$

$$b = \frac{H+t}{2}, \tag{4.12}$$

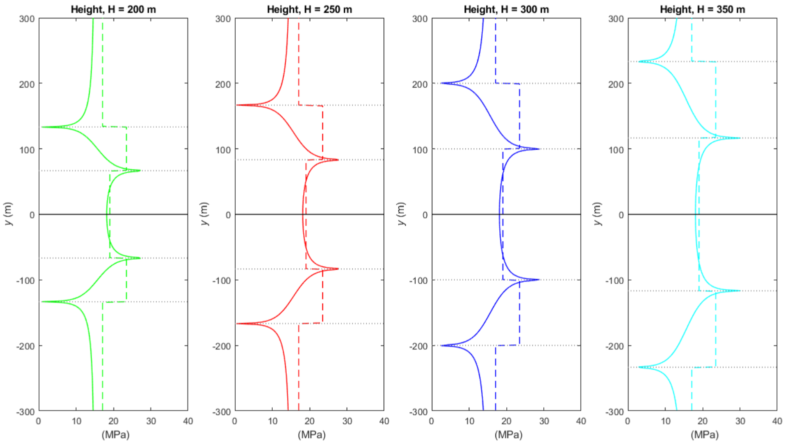

Figure 4.19: Total resultant shear stresses, $\sigma^{R,T}_{shear}$ (Solid lines), and the corresponding slip boundaries (dashed lines) at incremental pore pressures $p = -20$ MPa (Production) for different reservoir heights. The ratio of throw to height is fixed for all cases at $t/H = 1/3$

It can be seen that for the same thickness and same lateral extent of the reservoir a higher fault throw leads to higher shear stress in the section of the reservoir between the bottom of hanging wall and the top of the foot wall. As a result, the onset of slip requires a much lower incremental pore pressure in the case of a fault with higher throw. As we observed in section (4.2), for production, the concentration of shear stresses in the section of the fault where reservoir juxtaposes reservoir makes it more likely to slip at lower incremental pore pressures. As a result, with higher fault throw, this section of the reservoir reduces in thickness, approaching zero when the fault throw t equals height of the reservoir H. As the thickness of this section reduces, we observe a higher value of the resultant shear stress in that section, making it more likely to slip as compared to a fault with lower throw. It is thus conclusive that the fault with throw $t \geq H$ would witness induced shear stresses that exceed the slip threshold at the least incremental pore pressure. The strong dependency of critical pressures on fault throw implies the need for precise determination of fault throw while modelling initiation of slip. It would thus necessitate precise information of throws for all major faults in the reservoir, as opposed to a generalized fault throw used as a representation of all faults for studies aimed at prediction of induced seismicity from extraction/injection of fluids in a reservoir.

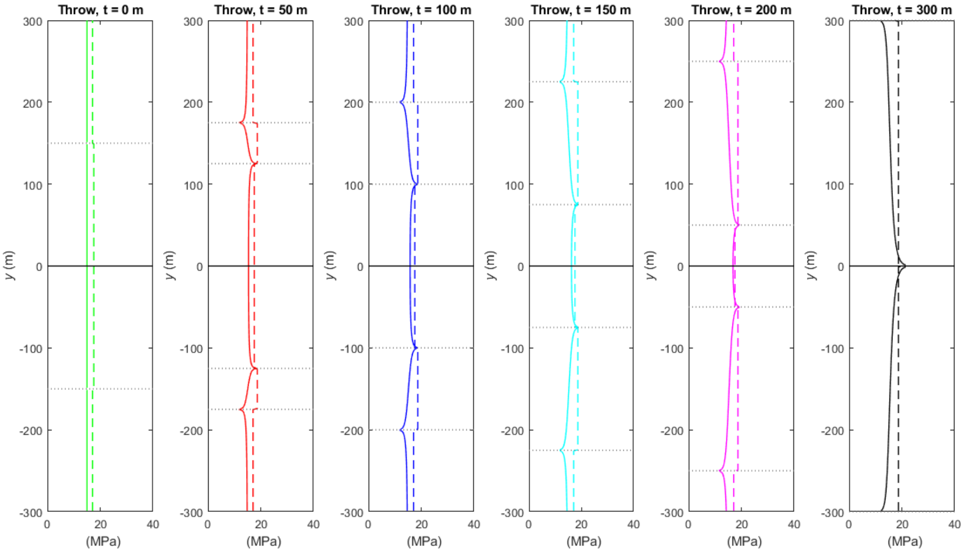

(a) Sensitivity of slip initiation to fault throw, *t*, at pore pressure *p* = -5Mpa

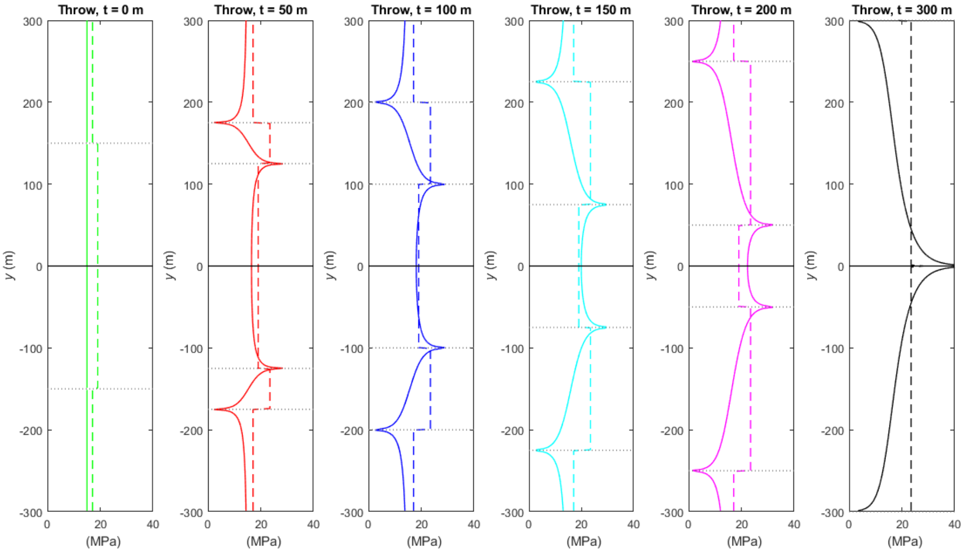

(b) Sensitivity of slip initiation to fault throw, *t*, at pore pressure *p* = -20Mpa

Figure 4.20: Total resultant shear stresses, $\sigma^{R,T}_{shear}$ *(Solid lines), and the corresponding slip boundaries (dashed lines) at incremental pore pressures* $p = -5$ *MPa and* $p = -20$ *MPa (Production) for different fault throws. Height of the reservoir is fixed for all cases at* $H = 300$ *m*

5

Conclusions

The findings in this study following the analytical approach for calculating induced stresses in a simplified three dimensional reservoir geometry with displaced faults are largely in line with results from the numerical modelling studies (Mulders [14], Orlic and Wassing [16], Buijze et al. [1] and Haug et al. [8]). The existing analytical models to the best of our knowledge, were limited to simpler geometries as also noted by Haug et al. [8]. The combined analysis in this report and in Jansen et al. [10] presents results for induced stresses in a two-dimensional reservoir with inclined displaced faults, a three-dimensional cuboidal reservoir with a vertical displaced fault and a laterally thinning three-dimensional reservoir with a vertical displaced fault. The insights from two-dimensional plane-strain analysis in Jansen et al. [10] are reaffirmed in this study. The effects of third dimension incorporation in the model and the effect of thickness variations in the reservoir are observed to be limited. Differences in the pattern of induced stresses as well as predicted directions for growth of slip patches for production and injection are also found in the three-dimensional reservoir. We find infinite peaks in induced stresses at reservoir boundaries (also observed by Buijze et al. [1]), which implies onset of slip at the slightest of pressure changes even in non-critically stressed faults at these locations. However in reality, aseismic slip or non-sharp reservoir edges and fault surfaces are likely to prevent propagation of the slip. The onset of slip besides the reservoir boundaries as predicted by our analysis is likely to be delayed until the pore pressure reaches a critical value, as pointed out by Van Wees et al.[29]. We also observe heterogeneous distribution of the induced stresses due to fault throw to cause earlier onset of slip, but the heterogeneous shear capacity utilization in this case is expected to limit the propagation of slip,in line with the findings by Van den Bogert [26] and Buijze et al. [1]. We also find the most likely section of the fault to be reactivated during production to be the part where reservoir juxtaposes reservoir, in agreement with predictions by Orlic and Wassing [16], Buijze et al. [1]. We also reaffirm the conclusions by Van den Bogert [26] about the strong dependency of onset of slip on the in-situ stresses, fault throw and fault frictional strength. We now compile the conclusions from this study and present our recommendations.

1. We successfully model the growth of elastic stresses induced by depletion or injection of fluid in a three-dimensional reservoir compartmentalized by a displaced fault.
2. We present closed form analytical expressions for induced stresses in a symmetrical cuboidal reservoir with a displaced vertical fault derived. Simplified expressions for a laterally thinning reservoir could not be obtained due to mathematical complexity of the three-dimensional integration.
3. We reaffirm the finding by Orlic and Wassing [16], Van den Bogert [26] and Buijze et al. [1] that the reservoir structural setting, particularly the fault throw significantly influences the induced stresses from depletion and thus the initiation of slip. We extend the conclusion to the case of injection into the reservoir as well.
4. A three-dimensional reservoir with a displaced fault exhibits a heterogeneous distribution of induced stresses, as compared to a uniform induced stress pattern for faults with zero throw. This is in line with the findings of previous numerical studies by Mulders [14], Orlic and Wassing [16] and Buijze et al. [1].
5. We note that the pattern of induced stresses observed is markedly different for the case of production and for injection. At the fault plane, in case of production, we observe concentration of positive

incremental shear stresses at the sections of fault where reservoir juxtaposes reservoir. For injection, this section experiences negative incremental shear stresses. But for the section beyond the reservoir boundaries, production causes negative shear stresses and injection results in negative incremental shear stress. There is a region of transition between the corresponding negative and positive incremental shear stresses where the reservoir juxtaposes overburden and underburden.

6. We observe peaks in the incremental shear stresses at the fault plane for both production and injection at the boundaries of reservoir units on either side of the fault. At the top of the hanging wall and the bottom of the foot wall, production induces a positive peak while injection induces a negative peak in incremental shear stresses. At the bottom of the hanging wall and the top of the foot wall, production induces a negative peak and injection induces a positive peak, as observed in figures (4.11(b)) and (4.10 (b)).

7. We use the same initial state of stress for both production and injection scenarios in our model, thus the total incremental shear stresses and slip thresholds are dependent on the incremental shear stresses and incremental pore pressures. At the reservoir boundaries that witness peaks in incremental shear stress, for production, the peaks at the top of the hanging wall and the bottom of the foot wall cross the slip threshold, while for injection, the peaks at the bottom of the hanging wall and the top of the foot wall cross the slip thresholds even at low pore pressure changes, as seen in figure (4.12).

8. For production at incremental pore pressure $p = -20$ MPa, some portion of the section of the fault where reservoir juxtaposes reservoir (corresponding to positive shear stress) experiences total resultant shear stresses close to slip threshold or $SCU \approx 1$ and is likely to witness propagation of slip even without any further depletion or injection. As pore pressure continues to decrease, a larger portion within this section witnesses total resultant shear stresses above the slip threshold. For injection at incremental pore pressure $p = 20$ MPa, total resultant shear stresses are higher in some portion of the section of the fault where reservoir juxtaposes overburden and underburden, while with increasing incremental pore pressure, a larger portion within this section undergoes slip. For injection, the section beyond the reservoir (overburden juxtaposing overburden and underburden juxtaposing underburden) has shear stresses close to the slip threshold or $SCU \approx 1$.

9. Another stark difference between production and injection scenarios is the critical incremental pore pressure required to initiate slip. For injection the critical incremental pore pressure is lower in absolute terms as compared to production, as seen in figures (4.12), 4.13) and (4.14). This implies for injection, a lower (absolute) change in pore pressure is likely to trigger slip and thus seismicity as compared to the (absolute) pore pressure change required for a similar reservoir under production.

10. The possible growth of slip patches is depicted by calculated values for Shear Capacity Utilisation (SCU) in figures (4.13) and (4.14). For injection, the two separate slip patches are observed to grow inwards from the top of the foot wall and the bottom of the hanging wall, until the slip patches reach the top of the hanging wall and the bottom of the foot wall. Thereafter the slip patches are predicted to grow outwards into the overburden and the underburden without merging. In the case of production, slip patches grow internally from the top of the hanging wall and bottom of the foot wall, until these slip patches merge into a single slip patch, which then grows laterally outwards into the adjacent rocks next to the reservoir, as seen in figure (4.14) and (4.17). Note that the predictions are based on an indicative calculation and that we do not model the slip dynamically. The predictions would require detailed dynamic modelling of slip patch growth to be conclusive.

11. The results obtained for the three-dimensional reservoir are qualitatively the same as we obtained for a two-dimensional reservoir under plane-strain conditions in [10]. This implies that the suspected propagation of stresses in the horizontal direction modifying the induced stress pattern and slip behaviour, as discussed in section (1.3), is observed in the three-dimensional analytical model. It can thus be concluded that plane-strain conditions are a good approximation of the three-dimensional stress state for modelling induced stresses and initiation of slip in a reservoir with a displaced fault.

12. The analysis conducted on an asymmetrical laterally thinning reservoir reveals the negligible effect of change in reservoir thickness over the pattern of induced stresses in the reservoir. The total resultant shear stresses follow the same qualitative pattern with respect to the slip thresholds, as in a symmetrical cuboidal reservoir, the peaks observed also correspond with the analogous reservoir boundaries and

thus the fault reactivation is expected to follow the same behaviour for both production and induction. This implies a symmetrical cuboidal reservoir could be an acceptable approximation to an otherwise laterally varied-thickness reservoir.

13. We find that the induced stresses in the reservoir at fault plane show an increasingly heterogeneous distribution with shear stress concentrations at reservoir boundaries, with increasing fault throw. With the increase in fault throw, the fault is expected to be reactivated at a lower level of depletion/injection as compared to a fault with zero throw. A reservoir with fault throw equal to thickness of the reservoir would experience the earliest onset of slip, as predicted by the results of sensitivity study in figure (4.20). The stress patterns do not vary with variation in reservoir thickness at constant ratio of fault throw to height.

Note that in our analysis, we only consider seismic slip across the fault. In reality, the slip might be seismic or aseismic that would change the pattern of induced stresses. Aseismic slip is the slow movement of rocks across the fault that does not trigger large scale seismic events, and can result in slow release of the stress build-up in the fault as a result of pore pressure changes. It is thus possible inclusion of aseismic slip in the analysis would lead to a delayed growth of the slip patch.

Recommendations

Testing the results for production/injection induced stresses by comparing predictions with actual field observations. With the results for three-dimensional stresses in a reservoir with a displaced fault, it is possible to use existing fault models in a hydrocarbon field, for example Groningen, along with known information about the pressure depletion and in-situ stresses to model the expected locations for faults likely to be reactivated at the corresponding reservoir pressures. Comparing predictions of such models with recorded seismic events would help confirm that proposed mechanisms are indeed the causal mechanisms for induced seismicity in such fields. Such comparisons would not be conclusive quantitatively, owing to the simplifying assumptions and limitations of our model. However the predictions are expected to correlate with actual field observations qualitatively in terms of the findings of this study.

We study the onset of slip by calculating induced stresses in a reservoir with linear elastic behaviour, however the predictions about subsequent propagation of slip and slip patch growth require further investigation by dynamic modelling of slip propagation. We also assume the fault frictional strength to be constant as a simplifying assumption. It is thus recommended to combine the analytical solutions for induced stresses with dynamic rupture analysis incorporating the non-linear rock behaviour as well as evolution of the fault's shear strength in the form of dynamic friction. Incorporation of cohesion into estimating fault shear strength can also help improving the quality of results. Incorporation of aseismic slip is also recommended in order to capture the possible slow release of accumulated energy.

We have attempted to introduce increasingly complex geometrical descriptions of the reservoir model, but further work can be done by incorporating further geometrical complexities in the model. Analytical expressions of induced stresses in a laterally thinning reservoir unsuccessfully attempted in this study can be calculated. The resultant stress patterns are not expected to change, but analytical expressions are quicker alternatives for further studies incorporating a similar geometry. Another complexity that can be introduced following the same approach as in this study, is non-homogeneous rock properties for the reservoir and enclosing domain. While we consider a reservoir the reservoir and overburden/underburden to be of the same elastic properties A different rock composition and elastic coefficients for different formations in the subsurface is likely to increase the heterogeneous distribution of stresses and thus possibly trigger slip at lower pressures, but possibly limited slip propagation.

We consider a reservoir with a single fault, but in reality there could be regions of high fault density with several faults in close proximity. The induced stress patterns and slip behaviour are likely to be influenced significantly due to multiple faults leading to a much more heterogeneous distribution of induced stresses. It is thus recommended to find analytical solutions for induced stresses incorporating the the effect of multiple faults in close proximity on the resultant stress patterns.

Symbol	*Meaning*	*SI units*
a, b, c, d, e, f, g, h	geometrical parameters	m
C	constant	N/m^2
D	constant	–
e	elastic strain	–
$\mathbf{f}$	vector representing a distributed force	N/m^2
g_i	Green's function for displacements	$1/m^2$
g_{ij}	Green's function for stresses	$1/m^3$
$\tilde{g}_{ij}$	Green's function for displacements (point source)	m/N
$\tilde{\mathbf{g}}_i$	vector of Green's functions $\tilde{g}_{ij}$	m/N
G_i	integral of Green's function g_i	m
G_{ij}	integral of Green's function g_{ij}	–
G	shear modulus	N/m^2
H	reservoir height	m
K	bulk modulus	N/m^2
$m, n, p, q, r, s,$	geometrical parameters	m
$\mathbf{n}$	unit normal vector	–
p	incremental pore pressure	N/m^2
$\hat{R}$	radial distance from nucleus of strain in 3D	m
t	fault throw	m
T	reservoir thickness	m
u	displacement	m
W	reservoir width	m
x, y, z	coordinates	m
α	Biot's coefficient	–
γ	Reservoir thickness reduction angle	rad
Γ	domain boundary	–
δ	Kronecker delta	–
ϵ	total strain	–
ϵ^*	eigenstrain	–
ζ, ξ, ψ	x, y and z coordinate values inside inclusion	m
θ	dip angle	rad
μ	friction coefficient	–
ν	Poisson's ratio	–
$\bar{\sigma}$	average stress	N/m^2
$\hat{\sigma}$	combined stress = $\sigma^0 + \sigma$	N/m^2
σ	total stress = $\sigma' + p$	N/m^2
σ'	effective stress = $\sigma - p$	N/m^2
σ^*	eigenstress	N/m^2
Ω	domain	–
Subscripts		
sl	slip	
Superscripts		
0	initial	
$'$	effective	
$*$	eigen	
R	resultant	
T	total	
inc	incremental	

Bibliography

[1] L. Buijze, P. A. J. van den Bogert, B. B. T. Wassing, B. Orlic, and J. ten Veen. Fault reactivation mechanisms and dynamic rupture modelling of depletion-induced seismic events in a rotliegend gas reservoir. *Netherlands Journal of Geosciences*, 96:s131–s148, 12 2017. doi: 10.1017/njg.2017.27.

[2] L. Buijze, P. A. J. van den Bogert, B. B. T. Wassing, and B. Orlic. Nucleation and arrest of dynamic rupture induced by reservoir depletion. *Journal of Geophysical Research: Solid Earth*, 124(4):3620–3645, 2019. doi: 10.1029/2018JB016941. URL `https://agupubs.onlinelibrary.wiley.com/doi/abs/10.1029/2018JB016941`.

[3] National Research Council. *Induced Seismicity Potential in Energy Technologies*. The National Academies Press, Washington, DC, 2013. ISBN 978-0-309-25367-3. doi: 10.17226/13355. URL `https://www.nap.edu/catalog/13355/induced-seismicity-potential-in-energy-technologies`.

[4] J.D. Eshelby. The Determination of the Elastic Field of an Ellipsoidal Inclusion, and Related Problems. *Proceedings of the Royal Society of London Series A*, 241:376–396, August 1957. doi: 10.1098/rspa.1957.0133.

[5] J. Geertsma. Problems of rock mechanics in petroleum production engineering. *ISRM-1CONGRESS-1966-099*, page 10, January 1966. URL `https://doi.org/`.

[6] J. Geertsma. Land subsidence above compacting oil and gas reservoirs. *Journal of Petroleum Technology*, 25(06):734–744, June 1973. ISSN 0149-2136. URL `https://doi.org/10.2118/3730-PA`.

[7] S.K. Guha. *Induced Earthquakes*. Kluwer Academic Publisher, 2000.

[8] C. Haug, J.A. Nüchter, and A. Henk. Assessment of geological factors potentially affecting production-induced seismicity in north german gas fields. *Geomechanics for Energy and the Environment*, 16: 15 – 31, 2018. ISSN 2352-3808. doi: https://doi.org/10.1016/j.gete.2018.04.002. URL `http://www.sciencedirect.com/science/article/pii/S2352380818300030`.

[9] J. H. Healy, W. W. Rubey, D. T. Griggs, and C. B. Raleigh. The denver earthquakes. *Science*, 161(3848): 1301–1310, 1968. ISSN 0036-8075. doi: 10.1126/science.161.3848.1301. URL `https://science.sciencemag.org/content/161/3848/1301`.

[10] J.D. Jansen, P. Singhal, and F.C. Vossepoel. Insights from closed-form expressions for injection- and production-induced stresses in displaced faults. *Journal of Geophysical Research: Solid Earth*, 0(0), 2019. doi: 10.1029/2019JB017932. URL `https://agupubs.onlinelibrary.wiley.com/doi/abs/10.1029/2019JB017932`.

[11] H. Kanamori and E.E. Brodsky. The physics of earthquakes. *Reports on Progress in Physics*, 67(8):1429–1496, jul 2004. doi: 10.1088/0034-4885/67/8/r03. URL `https://doi.org/10.1088%2F0034-4885%2F67%2F8%2Fr03`.

[12] A.E.H Love. *A Treatise on the Mathematical Theory of Elasticity*. Courier Corporation, 1927.

[13] W.G. Milne. The snipe lake, alberta earthquake of march 8, 1970. *Canadian Journal of Earth Sciences*, 7 (6):1564–1567, 1970. doi: 10.1139/e70-148. URL `https://doi.org/10.1139/e70-148`.

[14] F.M.M. Mulders. Modelling of stress development and fault slip in and around a producing gas reservoir. Master's thesis, Delft University of Technology, 2003.

[15] T. Mura. *Micromechanics of defects in solids*. Springer Science and Business Media, 1987.

[16] B. Orlic and B. Wassing. A study of stress change and fault slip in producing gas reservoirs overlain by elastic and viscoelastic caprocks. *Rock Mechanics and Rock Engineering*, 46, 05 2012. doi: 10.1007/s00603-012-0347-6.

[17] W.D. Pennington, S.D. Davis, S.M. Carlson, J. DuPree, and T.E. Ewing. The evolution of seismic barriers and asperities caused by the depressuring of fault planes in oil and gas fields of south texas. *Bulletin of the Seismological Society of America*, 76(4):939–948, April 1986. ISSN 0037-1106.

[18] W.E. Pratt and D.W. Johnson. Local subsidence of the goose creek oil field. *Journal of Geology*, 1926.

[19] C. B. Raleigh, J. H. Healy, and J. D. Bredehoeft. An experiment in earthquake control at rangely, colorado. *Science*, 191(4233):1230–1237, 1976. ISSN 0036-8075. doi: 10.1126/science.191.4233.1230. URL `https://science.sciencemag.org/content/191/4233/1230`.

[20] G. H. Rothe and C. Y. Lui. Possibility of induced seismicity in the vicinity of the sleepy hollow oil field, southwestern nebraska. *Bulletin of the Seismological Society of America*, 1983.

[21] P. Segall. Earthquakes triggered by fluid extraction. *Geology*, 17(10):942–946, 10 1989. ISSN 0091-7613. doi: 10.1130/0091-7613(1989)017<0942:ETBFE>2.3.CO;2. URL `https://doi.org/10.1130/0091-7613(1989)017<0942:ETBFE>2.3.CO;2`.

[22] P. Segall. Induced stresses due to fluid extraction from axisymmetric reservoirs. *Pure and Applied Geophysics*, 139(3-4):535–560, 1992. URL `http://pubs.er.usgs.gov/publication/70017120`.

[23] H. Soltanzadeh and C.D. Hawkes. Semi-analytical models for stress change and fault reactivation induced by reservoir production and injection. *Journal of Petroleum Science and Engineering*, 60(2): 71 – 85, 2008. ISSN 0920-4105. doi: https://doi.org/10.1016/j.petrol.2007.05.006. URL `http://www.sciencedirect.com/science/article/pii/S0920410507001076`.

[24] J. Suckale. Induced seismicity in hydrocarbon fields. *Advances in Geophysics - ADVAN GEOPHYS*, 51: 55–106, 12 2009. doi: 10.1016/S0065-2687(09)05107-3.

[25] K. Terzaghi. *Erdbaumechanik auf bodenphysikalischer grundlage*. Leipzig ; Wien : F. Deuticke, 1925.

[26] P.A.J. Van den Bogert. Impact of various modelling options on the onset of fault slip and fault slip response using 2-dimensional finite-element modelling. restricted report no. sr.15.11455. Technical report, Shell Global Solutions International B.V, Rijswijk, 2015.

[27] J. Van Wees, P. Fokker, K. Thienen-Visser, B. Wassing, S. Osinga, B. Orlic, A.S. Ghouri, L. Buijze, and M. Pluymaekers. Geomechanical models for induced seismicity in the netherlands: Inferences from simplified analytical, finite element and rupture model approaches. *Netherlands Journal of Geosciences*, 96:s183–s202, 12 2017. doi: 10.1017/njg.2017.38.

[28] T.K. Visser and J. Breunese. Induced seismicity of the groningen gas field:history and recent developments. *The Leading Edge*, 34:664–671, 06 2015. doi: 10.1190/tle34060664.1.

[29] J.D. Van Wees, L. Buijze, K. Van Thienen-Visser, M. Nepveu, B.B.T. Wassing, B. Orlic, and P.A. Fokker. Geomechanics response and induced seismicity during gas field depletion in the netherlands. *Geothermics*, 52:206 – 219, 2014. ISSN 0375-6505. doi: https://doi.org/10.1016/j.geothermics.2014.05.004. URL `http://www.sciencedirect.com/science/article/pii/S0375650514000583`. Analysis of Induced Seismicity in Geothermal Operations.

Appendices

A. Induced stresses in three-dimensional symmetrical cuboidal reservoir with a displaced fault

The resultant expressions for 3D integrals of the Green's functions $G_{ij}(x,y,z)$ for induced stresses in a symmetrical cuboidal reservoir with a displaced fault are listed below. The integrals are calulated according to the limits as defined in the following equaiton :

$$G_{ij}(x,y,z) = \int_m^n \int_r^s \int_p^q g_{ij}(x,y,z,\zeta,\xi,\psi)\, d\zeta\, d\xi\, d\psi \tag{A-1}$$

$$\begin{aligned}
G_{xx}(x,y,z) =& \frac{1}{2} \times [\\
-\ & \arctan\left(\frac{(z-m)(y-r)}{(p-x)\sqrt{(z-m)^2+(x-p)^2+(y-r)^2}}\right) + \arctan\left(\frac{(z-m)(y-s)}{(p-x)\sqrt{(z-m)^2+(x-p)^2+(y-s)^2}}\right)\\
+\ & \arctan\left(\frac{(z-m)(y-r)}{(q-x)\sqrt{(z-m)^2+(x-q)^2+(y-r)^2}}\right) - \arctan\left(\frac{(z-m)(y-s)}{(q-x)\sqrt{(z-m)^2+(x-q)^2+(y-s)^2}}\right)\\
+\ & \arctan\left(\frac{(z-n)(y-r)}{(p-x)\sqrt{(z-n)^2+(x-p)^2+(y-r)^2}}\right) - \arctan\left(\frac{(z-n)(y-s)}{(p-x)\sqrt{(z-n)^2+(x-p)^2+(y-s)^2}}\right)\\
-\ & \arctan\left(\frac{(z-n)(y-r)}{(q-x)\sqrt{(z-n)^2+(x-q)^2+(y-r)^2}}\right) + \arctan\left(\frac{(z-n)(y-s)}{(q-x)\sqrt{(z-n)^2+(x-q)^2+(y-s)^2}}\right)]
\end{aligned}$$

$$\begin{aligned}
G_{yy}(x,y,z) =& \frac{1}{2} \times [\\
-\ & \arctan\left(\frac{(z-m)(x-p)}{(r-y)\sqrt{(z-m)^2+(x-p)^2+(y-r)^2}}\right) + \arctan\left(\frac{(z-m)(x-p)}{(s-y)\sqrt{(z-m)^2+(x-p)^2+(y-s)^2}}\right)\\
+\ & \arctan\left(\frac{(z-m)(x-q)}{(r-y)\sqrt{(z-m)^2+(x-q)^2+(y-r)^2}}\right) - \arctan\left(\frac{(z-m)(x-q)}{(s-y)\sqrt{(z-m)^2+(x-q)^2+(y-s)^2}}\right)\\
+\ & \arctan\left(\frac{(z-n)(x-p)}{(r-y)\sqrt{(z-n)^2+(x-p)^2+(y-r)^2}}\right) - \arctan\left(\frac{(z-n)(x-p)}{(s-y)\sqrt{(z-n)^2+(x-p)^2+(y-s)^2}}\right)\\
-\ & \arctan\left(\frac{(z-n)(x-q)}{(r-y)\sqrt{(z-n)^2+(x-q)^2+(y-r)^2}}\right) + \arctan\left(\frac{(z-n)(x-q)}{(s-y)\sqrt{(z-n)^2+(x-q)^2+(y-s)^2}}\right)]
\end{aligned}$$

$$\begin{aligned}
G_{zz}(x,y,z) =& \frac{1}{2} \times [\\
& \arctan\left(\frac{(x-p)(r-y)}{(m-z)\sqrt{(z-m)^2+(x-p)^2+(y-r)^2}}\right) - \arctan\left(\frac{(x-p)(s-y)}{(m-z)\sqrt{(z-m)^2+(x-p)^2+(y-s)^2}}\right)\\
-\ & \arctan\left(\frac{(x-q)(r-y)}{(m-z)\sqrt{(z-m)^2+(x-q)^2+(y-r)^2}}\right) + \arctan\left(\frac{(x-q)(s-y)}{(m-z)\sqrt{(z-m)^2+(x-q)^2+(y-s)^2}}\right)\\
-\ & \arctan\left(\frac{(x-p)(r-y)}{(n-z)\sqrt{(z-n)^2+(x-p)^2+(y-r)^2}}\right) + \arctan\left(\frac{(x-p)(s-y)}{(n-z)\sqrt{(z-n)^2+(x-p)^2+(y-s)^2}}\right)\\
+\ & \arctan\left(\frac{(x-q)(r-y)}{(n-z)\sqrt{(z-n)^2+(x-q)^2+(y-r)^2}}\right) - \arctan\left(\frac{(x-q)(s-y)}{(n-z)\sqrt{(z-n)^2+(x-q)^2+(y-s)^2}}\right)]
\end{aligned}$$

$$\begin{aligned}
G_{xy}(x,y,z) = & \frac{1}{2} \times [\\
& \operatorname{arctanh}\left(\frac{m-z}{\sqrt{(z-m)^2+(x-p)^2+(y-r)^2}}\right) + \operatorname{arctanh}\left(\frac{z-m}{\sqrt{(z-m)^2+(x-p)^2+(y-s)^2}}\right) \\
+ & \operatorname{arctanh}\left(\frac{z-m}{\sqrt{(z-m)^2+(x-q)^2+(y-r)^2}}\right) + \operatorname{arctanh}\left(\frac{m-z}{\sqrt{(z-m)^2+(x-q)^2+(y-s)^2}}\right) \\
+ & \operatorname{arctanh}\left(\frac{z-n}{\sqrt{(z-n)^2+(x-p)^2+(y-r)^2}}\right) + \operatorname{arctanh}\left(\frac{n-z}{\sqrt{(z-n)^2+(x-p)^2+(y-s)^2}}\right) \\
+ & \operatorname{arctanh}\left(\frac{n-z}{\sqrt{(z-n)^2+(x-q)^2+(y-r)^2}}\right) + \operatorname{arctanh}\left(\frac{z-n}{\sqrt{(z-n)^2+(x-q)^2+(y-s)^2}}\right)]
\end{aligned}$$

$$\begin{aligned}
G_{yz}(x,y,z) = & \frac{1}{2} \times [\\
& \operatorname{arctanh}\left(\frac{p-x}{\sqrt{(z-m)^2+(x-p)^2+(y-r)^2}}\right) + \operatorname{arctanh}\left(\frac{x-p}{\sqrt{(z-m)^2+(x-p)^2+(y-s)^2}}\right) \\
+ & \operatorname{arctanh}\left(\frac{x-q}{\sqrt{(z-m)^2+(x-q)^2+(y-r)^2}}\right) + \operatorname{arctanh}\left(\frac{q-x}{\sqrt{(z-m)^2+(x-q)^2+(y-s)^2}}\right) \\
+ & \operatorname{arctanh}\left(\frac{x-p}{\sqrt{(z-n)^2+(x-p)^2+(y-r)^2}}\right) + \operatorname{arctanh}\left(\frac{p-x}{\sqrt{(z-n)^2+(x-p)^2+(y-s)^2}}\right) \\
+ & \operatorname{arctanh}\left(\frac{q-x}{\sqrt{(z-n)^2+(x-q)^2+(y-r)^2}}\right) + \operatorname{arctanh}\left(\frac{x-q}{\sqrt{(z-n)^2+(x-q)^2+(y-s)^2}}\right)]
\end{aligned}$$

$$\begin{aligned}
G_{zx}(x,y,z) = & \frac{1}{2} \times [\\
& \operatorname{arctanh}\left(\frac{r-y}{\sqrt{(z-m)^2+(x-p)^2+(y-r)^2}}\right) + \operatorname{arctanh}\left(\frac{y-s}{\sqrt{(z-m)^2+(x-p)^2+(y-s)^2}}\right) \\
+ & \operatorname{arctanh}\left(\frac{y-r}{\sqrt{(z-m)^2+(x-q)^2+(y-r)^2}}\right) + \operatorname{arctanh}\left(\frac{s-y}{\sqrt{(z-m)^2+(x-q)^2+(y-s)^2}}\right) \\
+ & \operatorname{arctanh}\left(\frac{y-r}{\sqrt{(z-n)^2+(x-p)^2+(y-r)^2}}\right) + \operatorname{arctanh}\left(\frac{s-y}{\sqrt{(z-n)^2+(x-p)^2+(y-s)^2}}\right) \\
+ & \operatorname{arctanh}\left(\frac{r-y}{\sqrt{(z-n)^2+(x-q)^2+(y-r)^2}}\right) + \operatorname{arctanh}\left(\frac{y-s}{\sqrt{(z-n)^2+(x-q)^2+(y-s)^2}}\right)]
\end{aligned}$$

We now check the integrals $G_{xx}(x,y,z)$, $G_{yy}(x,y,z)$ and $G_{xy}(x,y,z)$ obtained for a reservoir with infinite extension in the $z-$ direction with $g = h = \infty$. For each of the cuboidal units, the dimensions in $z-$ direction are identical with $-g < z < h$. Therefore, we find the expression for the general cuboidal unit defined by dimensions p,q,r,s,m,n with $m = -\infty$ and $n = \infty$ to compare with the results obtained for plane-strain case in Jansen et al. [10], or

$$G_{ij}(x,y,z) = \int_{-\infty}^{\infty}\int_{r}^{s}\int_{p}^{q} g_{ij}(x,y,z,\zeta,\xi,\psi)\, d\zeta\, d\xi\, d\psi \tag{A-2}$$

The resultant expressions thus obtained are as listed below, :

$$\begin{aligned}
G_{xx}(x,y,z) = & \frac{1}{2} \times [\\
- & \arctan\left(\frac{(y-r)}{(p-x)}\right) - \arctan\left(\frac{(y-r)}{(p-x)}\right) + \arctan\left(\frac{(y-s)}{(p-x)}\right) + \arctan\left(\frac{(y-s)}{(p-x)}\right) \\
+ & \arctan\left(\frac{(y-r)}{(q-x)}\right) + \arctan\left(\frac{(y-r)}{(q-x)}\right) - \arctan\left(\frac{(y-s)}{(q-x)}\right) - \arctan\left(\frac{(y-s)}{(q-x)}\right)] \\
= & \arctan\left(\frac{y-s}{x-q}\right) - \arctan\left(\frac{y-r}{x-q}\right) - \arctan\left(\frac{y-s}{x-p}\right) + \arctan\left(\frac{y-r}{x-p}\right).
\end{aligned}$$

Similarly, we simplify the expressions for $G_{yy}(x,y,z)$ and $G_{xy}(x,y,z)$

$$G_{yy}(x,y,z) = \arctan\left(\frac{x-q}{y-s}\right) - \arctan\left(\frac{x-q}{y-r}\right) - \arctan\left(\frac{x-p}{y-s}\right) + \arctan\left(\frac{x-p}{y-r}\right),$$

and

$$G_{xy}(x,y,z) = \frac{1}{2}\ln\frac{\left((x-q)^2+(y-s)^2\right)\left((x-p)^2+(y-r)^2\right)}{\left((x-q)^2+(y-r)^2\right)\left((x-p)^2+(y-s)^2\right)} \tag{A-3}$$

Additionally, we also find the expression for $G_{zx}(x,y,z)$, so as to enable us the calculation for total resultant shear stresses induced due to production or injection of fluids. The resultant after simplification is, $\lim_{m\to-\infty,n\to\infty} G_{zx}(x,y,z) = 0$. The expressions obtained for $G_{xx}(x,y,z)$, $G_{yy}(x,y,z)$, $G_{xy}(x,y,z)$ are analogous to the expressions obtained for two-dimensional plane-strain expressions obtained in Jansen et al. [10].

Thus for a reservoir with infinite extent in $z-$ direction and in $x-$ direction, that is, for $g = h = c = d = \infty$, the integrals $G_{xx}(x,y,z)$, $G_{yy}(x,y,z)$, $G_{xy}(x,y,z)$ will be the same as obtained for the two-dimensional reservoir by Janesen et all.

B. Induced stresses in three-dimensional asymmetrical laterally thinning reservoir with a displaced fault

For an asymmetrical laterally thinning reservoir, the analytical expressions for three-dimensional integrals of Green's functions for induced stresses $G_{ij}(x,y,z)$ are not obtained, as mentioned in section (4.1.2) due to mathematical complexity. Instead, the integrals for Green's function for induced stress,$g_{ij}(x,y,z)$ due to a point for have been performed in only two dimensions analytically and the results for induced stresses are thus calculated using numerical integration in the third dimension. The resultant expressions after two-dimensional integrals of the Green's functions for induced stress,$g_{ij}(x,y,z)$, in an asymmetrical laterally thinning reservoir, denoted by $G'_{ij}(x,y,z)$, are as below

$$
\begin{aligned}
G'_{xx}(x,y,z) = & \int_s^{s+(n-\psi)\tan\gamma}\int_p^q g_{ij}(x,y,z,\zeta,\xi,\psi)\,d\zeta d\xi \\
= \frac{1}{2}\times\Big[& \\
& \frac{(x-p)\big((n-\psi)\tan\gamma-(y-s)\big)}{\big((x-p)^2+(z-\psi)^2\big)\sqrt{\big((n-\psi)\tan\gamma-(y-s)\big)^2+(x-p)^2+(z-\psi)^2}} \\
- & \frac{(x-q)\big((n-\psi)\tan\gamma-(y-s)\big)}{\big((x-q)^2+(z-\psi)^2\big)\sqrt{\big((n-\psi)\tan\gamma-(y-s)\big)^2+(x-q)^2+(z-\psi)^2}} \\
+ & \frac{(x-p)(y-s)}{\big((x-p)^2+(z-\psi)^2\big)\sqrt{(x-p)^2+(y-s)^2+(z-\psi)^2}} \\
- & \frac{(x-q)(y-s)}{\big((x-q)^2+(z-\psi)^2\big)\sqrt{(x-q)^2+(y-s)^2+(z-\psi)^2}}\ \Big]
\end{aligned}
$$

$$
\begin{aligned}
G'_{yy}(x,y,z) = & \int_p^q\int_s^{s+(n-\psi)\tan\gamma} g_{ij}(x,y,z,\zeta,\xi,\psi)\,d\xi d\zeta \\
= \frac{1}{2}\times\Big[& \\
& \frac{(x-p)\big((n-\psi)\tan\gamma-(y-s)\big)}{\Big(\big((n-\psi)\tan\gamma-(y-s)\big)^2+(z-\psi)^2\Big)\sqrt{\big((n-\psi)\tan\gamma-(y-s)\big)^2+(x-p)^2+(z-\psi)^2}} \\
- & \frac{(x-q)\big((n-\psi)\tan\gamma-(y-s)\big)}{\Big(\big((n-\psi)\tan\gamma-(y-s)\big)^2+(z-\psi)^2\Big)\sqrt{((n-\psi)\tan\gamma-(y-s))^2+(x-q)^2+(z-\psi)^2}} \\
+ & \frac{(x-p)(y-s)}{\big((y-s)^2+(z-\psi)^2\big)\sqrt{(x-p)^2+(y-s)^2+(z-\psi)^2}} \\
- & \frac{(x-q)(y-s)}{\big((y-s)^2+(z-\psi)^2\big)\sqrt{(x-q)^2+(y-s)^2+(z-\psi)^2}}\ \Big]
\end{aligned}
$$

$$
\begin{aligned}
G'_{zz}(x,y,z) = & \int_p^q\int_m^{n-(\xi-s)\cot\gamma)} g_{ij}(x,y,z,\zeta,\xi,\psi)\,d\psi d\zeta \\
= \frac{1}{2}\times\Big[& \\
& \frac{(x-p)\big((s-\xi)\cot\gamma-(z-n)\big)}{\big((n+(s-\xi)\cot\gamma-z)^2+(y-\xi)^2\big)\sqrt{\big((s-\xi)\cot\gamma-(z-n)\big)^2+(x-p)^2+(y-\xi)^2}} \\
- & \frac{(x-q)\big((s-\xi)\cot\gamma-(z-n)\big)}{\big((n+(s-\xi)\cot\gamma-z)^2+(y-\xi)^2\big)\sqrt{\big((s-\xi)\cot\gamma-(z-n)\big)^2+(x-q)^2+(y-\xi)^2}} \\
+ & \frac{(z-m)(x-p)}{\big((z-m)^2+(y-\xi)^2\big)\sqrt{(x-p)^2+(y-\xi)^2+(z-m)^2}} \\
- & \frac{(z-m)(x-q)}{\big((z-m)^2+(y-\xi)^2\big)\sqrt{(x-q)^2+(y-\xi)^2+(z-m)^2}}\ \Big]
\end{aligned}
$$

$$
\begin{aligned}
G'_{xy}(x,y,z) = & \int_{s}^{s+(n-\psi)\tan\gamma} \int_{p}^{q} g_{ij}(x,y,z,\zeta,\xi,\psi)\, d\zeta d\xi \\
= \frac{1}{2} \times \Big[& \\
& \frac{1}{\sqrt{\big((n-\psi)\tan\gamma-(y-s)\big)^2+(x-p)^2+(z-\psi)^2}} - \frac{1}{\sqrt{(x-p)^2+(y-s)^2+(z-\psi)^2}} \\
- & \frac{1}{\sqrt{\big((n-\psi)\tan\gamma-(y-s)\big)^2+(x-q)^2+(z-\psi)^2}} + \frac{1}{\sqrt{(x-q)^2+(y-s)^2+(z-\psi)^2}} \Big]
\end{aligned}
$$

$$
\begin{aligned}
G'_{yz}(x,y,z) = & \int_{p}^{q} \int_{s}^{s+(n-\psi)\tan\gamma} g_{ij}(x,y,z,\zeta,\xi,\psi)\, d\xi d\zeta \\
= \frac{1}{2} \times \Big[& \\
- & \frac{(x-p)(z-\psi)}{\Big(\big((n-\psi)\tan\gamma-(y-s)\big)^2+(z-\psi)^2\Big)\sqrt{\big((n-\psi)\tan\gamma-(y-s)\big)^2+(x-p)^2+(z-\psi)^2}} \\
+ & \frac{(z-\psi)(x-q)}{\Big(\big((n-\psi)\tan\gamma-(y-s)\big)^2+(z-\psi)^2\Big)\sqrt{\big((n-\psi)\tan\gamma-(y-s)\big)^2+(x-q)^2+(z-\psi)^2}} \\
+ & \frac{(x-p)(z-\psi)}{\big((y-s)^2+(z-\psi)^2\big)\sqrt{(x-p)^2+(y-s)^2+(z-\psi)^2}} \\
- & \frac{(z-\psi)(x-q)}{\big((y-s)^2+(z-\psi)^2\big)\sqrt{(x-q)^2+(y-s)^2+(z-\psi)^2}} \Big]
\end{aligned}
$$

$$
\begin{aligned}
G'_{zx}(x,y,z) = & \int_{s}^{s+(n-\psi)\tan\gamma} \int_{p}^{q} g_{ij}(x,y,z,\zeta,\xi,\psi)\, d\zeta d\xi \\
= \frac{1}{2}(\psi-z) \times \Big[& \\
- & \frac{(n-\psi)\tan\gamma-(y-s)}{\big((x-p)^2+(z-\psi)^2\big)\sqrt{\big((n-\psi)\tan\gamma-(y-s)\big)^2+(x-p)^2+(z-\psi)^2}} \\
+ & \frac{(n-\psi)\tan\gamma-(y-s)}{\big((x-q)^2+(z-\psi)^2\big)\sqrt{\big((n-\psi)\tan\gamma-(y-s)\big)^2+(x-q)^2+(z-\psi)^2}} \\
- & \frac{y-s}{\big((x-p)^2+(z-\psi)^2\big)\sqrt{(x-p)^2+(y-s)^2+(z-\psi)^2}} \\
+ & \frac{y-s}{\big((x-q)^2+(z-\psi)^2\big)\sqrt{(x-q)^2+(y-s)^2+(z-\psi)^2}} \Big]
\end{aligned}
$$